6. Telescope optics

6.1 Requirements and guidelines

The design shall be optimized along the objectives outlined in Table 6-1. These objectives are derived from science and level 1 requirements and from indirect, engineering requirements (see table). They apply to a 100-m aperture design. Implied characteristics are derived in Figure 6-1. With a conventional two-mirror design, the need for field stabilization and embedded active and adaptive optics, together with the maximum size of the adaptive corrector, would imply a four-metre class secondary mirror performing all active and adaptive functions, on top of of field stabilization. A compact telescope structure (length ~ diameter) leads to a ~f/1 primary mirror, and an acceptable linear field dimension (~2-m) implies a relatively fast telescope focal ratio (~f/6-f/7). A Ritchey-Chretien design with such characteristics has a ~20-25 arc seconds diffraction-limited field of view (λ=0.5 μm). It follows that a conventional two-mirror solution cannot meet requirements, in addition to implying unrealistic constraints on the secondary mirror technology[45]. An all-aspherical, three mirror solution would not, either. In order to provide a real image of the pupil (ground layer), the secondary mirror would have to be concave; with a M1-M2 separation of ~100-m and a maximum secondary mirror diameter of 8.3-m, this implies a f/0.93 aspherical primary mirror. In order to produce a ~4m diameter exit pupil (adaptive mirror), the secondary mirror would have to be concave, f/0.45. In addition, the adaptive mirror (M3) would obstruct all rays travelling from the primary towards the secondary mirror. Allowing for a linear obscuration ratio of ~50% by M3 would require a f/0.25 secondary mirror. We conclude that the minimum number of surfaces is 4. As a result, a spherical primary mirror solution may become an attractive option, in line with the crucial objective of maximizing aperture while minimizing costs.

Aspherical primary mirror solutions imply severe limitations on the fabrication and maintenance processes. Those may be acceptable with a few dozen segments, but may become prohibitive with a few thousands. Aspherical segments could be polished in a way mimicking spherical polishing, whereby segments are mounted onto a warping harness tuned to provide the desired shape upon relaxation. This implies tight requirements on residual stresses in the substrate, and is most probably incompatible with lightweight, structured blanks. It also favours smaller segments, with a correspondingly smaller deviation from best fitting sphere –although in the case of OWL, the individual segments focal ratio would be large hence their allowable diameter large enough for such disadvantage to be inconsequential. In addition, the machine time required to finish the segments after edge-cutting is anything but predictable –at least until a representative sample has been produced. Even though ion-beam polishing, magnetic rheology polishing and small computer-controlled tools techniques have proven and excellent converging characteristics, none of these techniques can reasonably compete with full-size rigid tool

[45] We refer to the amplitude of the adaptive shell deformations but not necessarily tip-tilt correction. Field stabilization and adaptive compensation may be combined in a two-stage unit, with large amplitude, low temporal frequencies taken care of by a tip-tilt mount allowing rigid body motion of the corrector and adaptive support.

polishing. The latter not only allows for a much favorable wear law –in proportion to tool area- but also for intrinsically smoother surfaces.

More importantly perhaps, in the aspherical case optical testing requires that the setup be tailored to families of segments, with evident matching risks and time overheads. Spherical solutions, on the contrary, offer the opportunity to measure all segments against a unique reference, according to a straightforward procedure.

Objective / guideline	Reasons	
Field aberrations over the science field (3 arc minutes diameter) shall be axisymmetrical or negligible.	Compensation of asymmetrical field aberrations in the science instrument is generally impossible.	M
Optical quality shall be maximized over a field of view at least twice larger than that directly implied by top level requirements.	Avoid field aberration offsets in wide-field Adaptive Optics control (ground layer AO, MCAO).	M
The total number of surfaces shall be minimized.	Minimal emissivity and maximal throughput.	C
Obscurations shall be minimized	Throughput, image contrast at intermediate angular frequencies	C
Total length shall be optimized for minimal structure and enclosure dimensions.	Cost (including enclosure), structural performance.	C
Sensitivity to misalignments shall be minimized.	Relaxed tolerances, low sensitivity to wind-induced misalignments.	C
The total linear field of view (diameter) shall be in the range of ~2-m	Allow for (presumably) sufficient design space while limiting flexures e.g. in sensors arms.	D
The field of view (diameter) available for adaptive optics wavefront sensing shall be 6 arc minutes.	Large field AO sensing (MCAO, GLAO)	M
The field of view (diameter) available for non-adaptive wavefront sensing shall be maximized.	Sky coverage not limited by non-adaptive wavefront control.	C
The design shall provide suitable surfaces for active optics, including deformable mirror(s), active centring, focusing, and field stabilization	Compensation of inevitable, large amplitude and low frequency errors.	M
Field stabilization shall be done in a pupil image	Avoid pupil motion	M
The design shall provide a suitably located surface for single-conjugate IR SCAO and GLAO. Additional surface(s) for MCAO would be an advantage.	IR single-conjugate AO and GLAO provided by the telescope.	M D
The adaptive mirror(s) shall preferably have dimensions not smaller than 2-m and not larger than 4-m. Adaptive mirrors shall preferably be monolithic.	Moderate extrapolation from current adaptive secondary mirror technology (~1-m diameter with ~27 mm interactuator spacing).	C
An intermediate focus suitable for AO calibration (interaction matrices) would be an advantage.	Avoid the need for on-sky calibration (overheads on science, possibly less accurate than in-situ calibration with an artificial reference).	D
Monolithic mirrors shall be less than 8.3m in diameter (useful area).	Larger monolithic mirrors would require lengthy technology development.	M
Segments shape and material shall preferably - be compatible with serial production and maintenance; - be compatible with processes minimizing high spatial frequency misfigure; - allow moderate to high lightweighting ratio.	 Construction and operation costs; Optical quality; Structural performance and control bandwidth	 C C D

Table 6-1. Optical design: guidelines and objectives. M=Mandatory; C=Critical; D=Desirable.

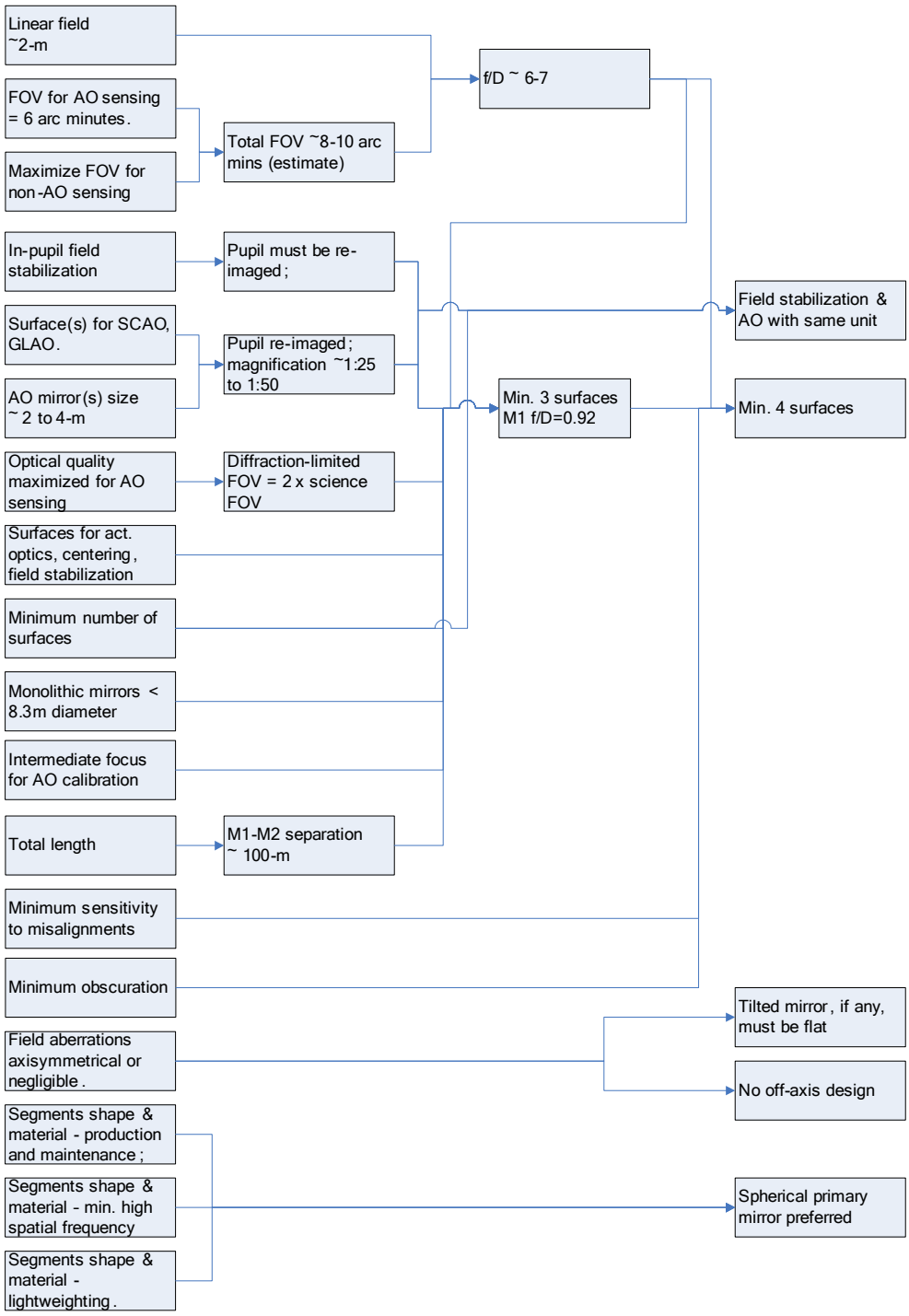

Figure 6-1. Implied characteristics.

Spherical primary mirror solutions have crucial advantages in terms of cost, risk, and performance:

- Ideally suited for serial production and maintenance of all-identical segments; low industrial risks;
- Optical testing against a unique reference matrix possible; very low risk of inter-segments matching errors;
- Smaller number of spares than with aspherical solutions;

- Fast polishing process, full-sized rigid tools possible; no need for warping harness, higher process yield;
- Polishing with large rigid tools may allow segments to be polished hexagonal without wasters or post-polish cutting to shape (hence relaxed specifications for blanks residual stresses);
- Polishing with large rigid tools is intrinsically more favorable in relation to high spatial frequency errors;
- Compatibility with lightweight segments technology46.

With an expected number of segments in the range of 3,000 units, compatibility with serial production is an advantage that can hardly be over-emphasized. Reliable optical testing against a unique matrix is also of primordial importance. In the aspherical case optical testing requires that the setup be tailored to families of segments, with evident matching risks and time overheads.

In brief, feasibility per se is not enough; even without consideration for cost, a production rate of about 1 segment per day necessarily requires predictable and largely automated processes. A spherical primary mirror is not a mandatory requirement but plausibly a critical one.

On the negative side, primary mirror solutions require a complex corrector for spherical and field aberrations. In practice, a strongly aspherical mirror will have to be conjugated to the primary mirror. Size and feasibility of this aspheric mirror will play against a short primary mirror focal ratio and imply either a structure longer than desirable or a very large (segmented) secondary mirror.

The requirements and guidelines outlined above imply that the optical design must be set up in a more complex, methodical approach than that applicable to traditional designs. In particular, optical solutions are subject to a lengthy iteration process to provide –if possible- suitable conjugates for adaptive, single-conjugate or multi-conjugate adaptive optics.

6.2 Optical design

6.2.1 Design trade-off

Several optical design solutions have been explored [9], starting with a four-mirror solution [10]. Two- and three-mirror solutions are ruled out as shown in section 6.1. Because of its modular design, the telescope structure could rapidly be re-configured for a quick evaluation of structural characteristics (see Figure 6-2 for examples based on a former family of structural design solutions).

As the minimum number of surfaces implied by the requirements and guidelines is four, there are strong cost, performance and risk incentives to explore spherical primary mirror solutions (see section 6.1). Other solutions have nevertheless been explored –more than can be accounted for in this report. These solutions have been rated against merit functions – essentially a list of relevant criteria. Each criterion is attributed a weight indicative of the criticality of the corresponding characteristic. Weights and ratings are evidently subjective. Results can **only** be used to identify clear trends but not to resolve “close matches”.

Appendix 8 lists the criteria included in the function of merit, together with their relative weights. This function of merit is plausibly incomplete and will require update, most notably to take into account the results of ongoing instruments design studies, of AO simulations, and of developments in the area of wavefront sensing with Laser Guide Stars. The design must comply with the mandatory requirements also listed in Appendix 8.

[46] Although warping harness could theoretically be used with lightweight segments, their design and operation would likely be incompatible with serial production, and predictability of the final shape is likely to be poor.

Ratings associated to feasibility (e.g. to adaptive mirror dimensions) make implicit assumptions as to the current state of technology, probable design solutions or plausible evolution thereof. Ratings will be re-assessed in the preliminary design phase; substantial changes in the optical design could be accommodated within the first year of the design phase, and significant ones within the first two years. Both criteria and the way ratings are attributed have, for obvious reasons, evolved throughout the conceptual design phase.

It appeared quite early in the design phase that the telescope size and the maximum allowable monolithic mirror diameter (8.3-m) impose strong geometrical constraints on the design. Otherwise attractive options were ruled out for this specific reason, as 10- to 12-m class monolithic mirror, if feasible at all, would require technology developments incompatible with a competitive schedule. By way of consequence, this also means that a relaxation of telescope diameter to ~60-70m would allow for a larger number of options, some of which substantially more attractive than the current baseline (see also RD6 and section 6.2.4).

The maximum dimension of monolithic surfaces is inspired from past experience, including but not limited to the VLT. In particular, the technology development underlying even a modest extrapolation from existing blanks dimensions always required more time and effort than anticipated. According to current schedule estimates, 8-m class mirrors for OWL are already on the critical path and their schedule can probably not be compressed by much. Larger dimensions (~10-m) would plausibly imply an additional 3 to 4 years to first light, on top of significant investments in suitable production infrastructures.

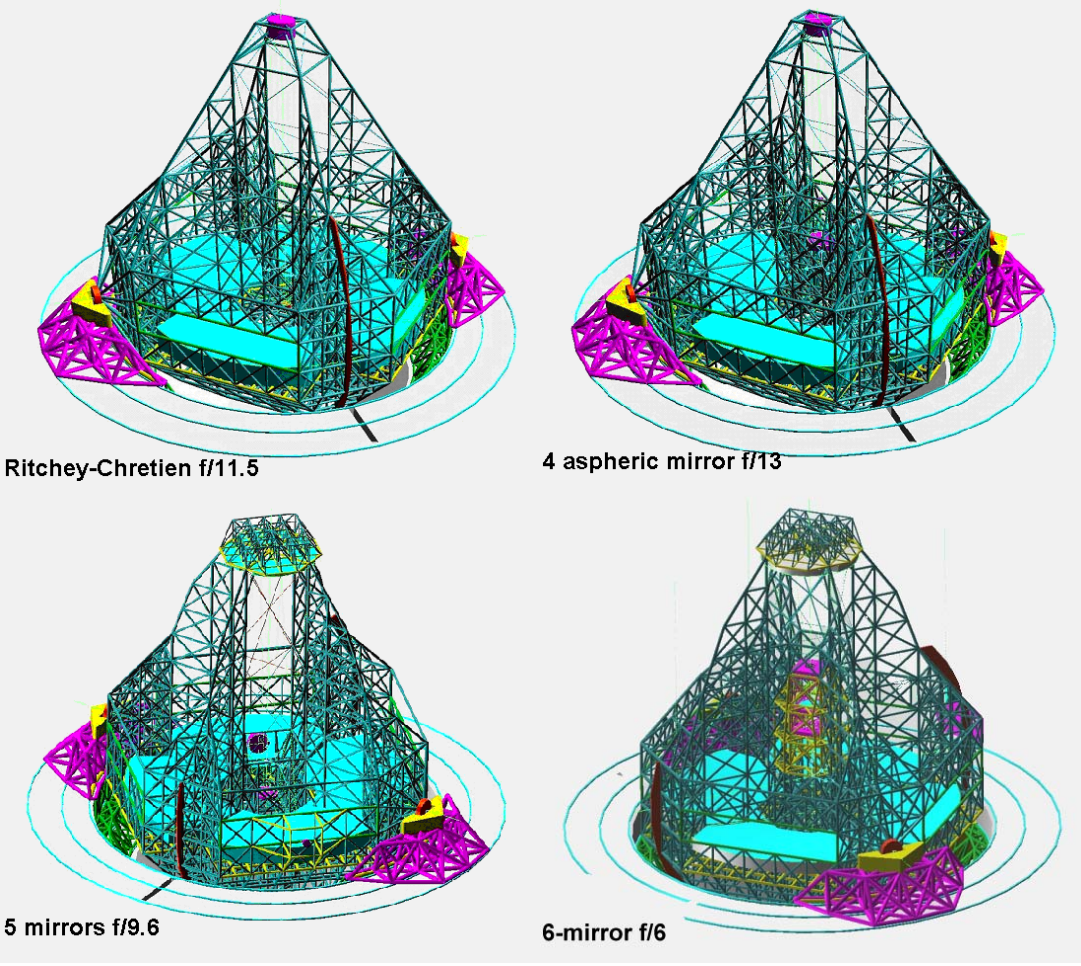

Figure 6-2. Mechanical implementation of different optical designs.

Figure 6-3 to Figure 6-6 show a few of the designs which have been evaluated. Although it does not comply with mandatory requirements, a Ritchey-Chrétien is included for reference. Design No 3 corresponds to the optional corrector (see section 6.2.3). The ratings for these four

designs are given in Table 6-2. Even when allowing for partly subjective weight and ratings allocations, the current baseline stands as best compromise.

These designs are only a sample of all those which have been briefly explored. Figure 6-7 shows an interesting solution, with an extremely fast (f/0.89) primary mirror and a failry well corrected 10 arc minutes field of view, with a wavefront error in the range of 1.5 μm RMS at the edge of the field. The exit focal ratio can be set in the f/8 to f/15 range. This design was rejected because of the enormous obscuration (47% linear), and the prohibitive size of the monolithic mirrors M2 and M3 (9.4 and 10.5-m). A folded version, with flat secondary mirror and relaxed focal ratio of the primary, might alleviate these problems but the instrumentation would be inconveniently located between the flat secondary and the corrector.

Figure 6-8 shows a five-mirror solution, with f/1.42 spherical primary and a convex, spherical secondary mirror. Field aberrations within 10 arc minutes field diameter are stronger (by a factor ~5) than with the baseline and with the design of Figure 6-7. This can probably be improved by further optimization. The Nasmyth-type focus is a major advantage for instrumentation. All monolithic mirrors are less than 8.3-m diameter. This design was rejected because none of the surfaces have adequate dimension and/or location for adaptive optics and field stabilization.

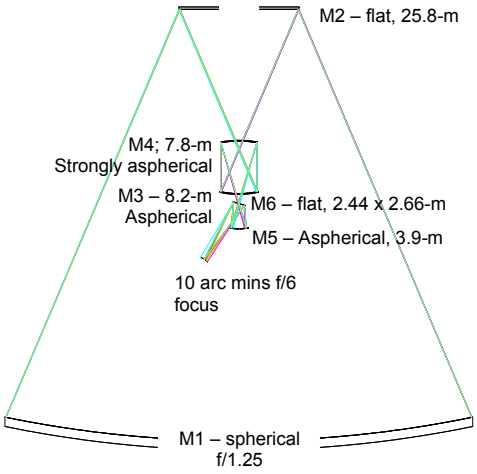

Figure 6-3. Baseline optical design (design No 1).

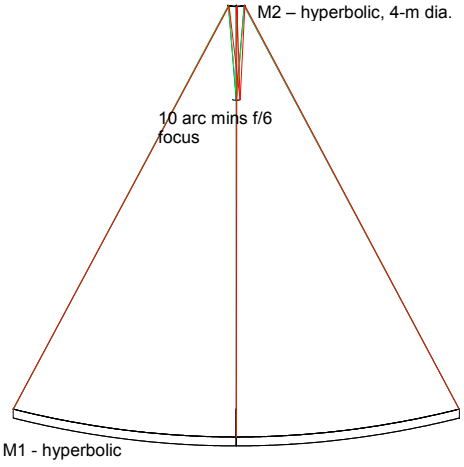

Figure 6-4. Ritchey-Chretien design (design No 2).

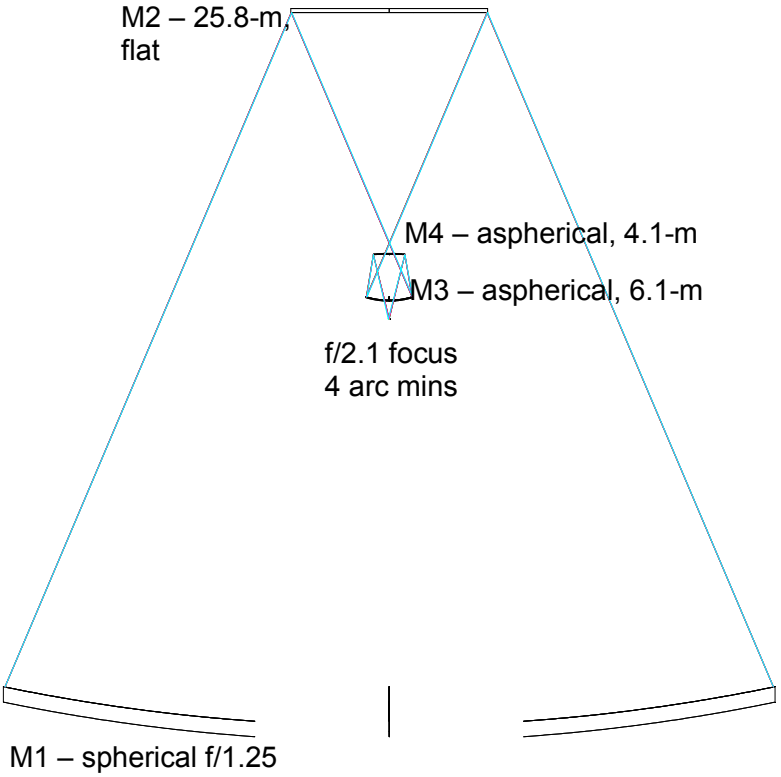

Figure 6-5. Four mirror, spherical primary & flat secondary mirrors solution (design No 3).

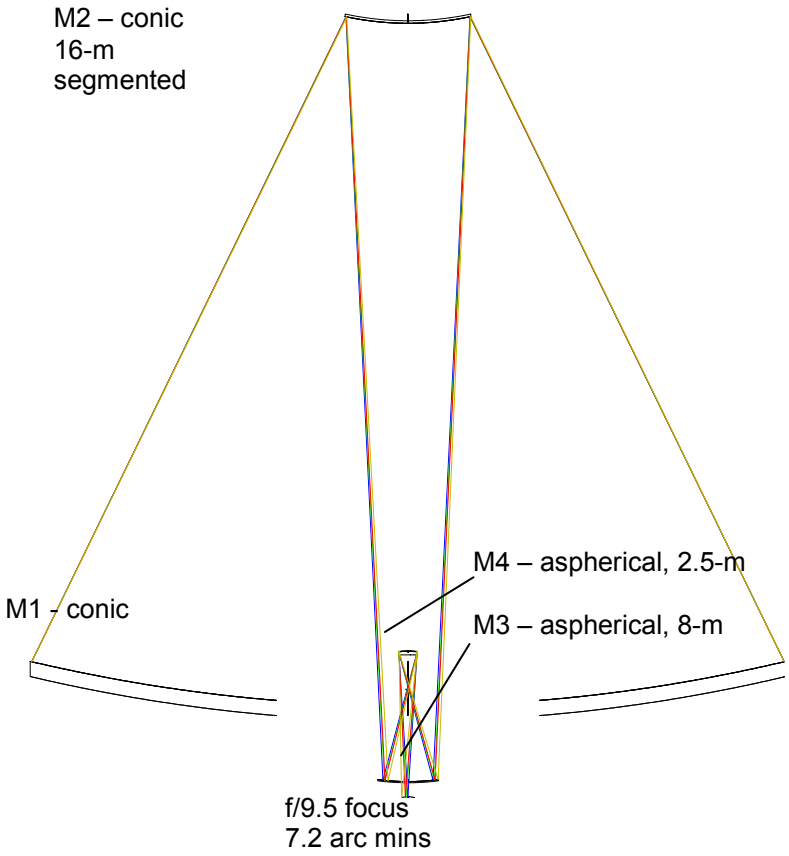

Figure 6-6. Four-mirror, conic M1 & M2 design (design No 4).

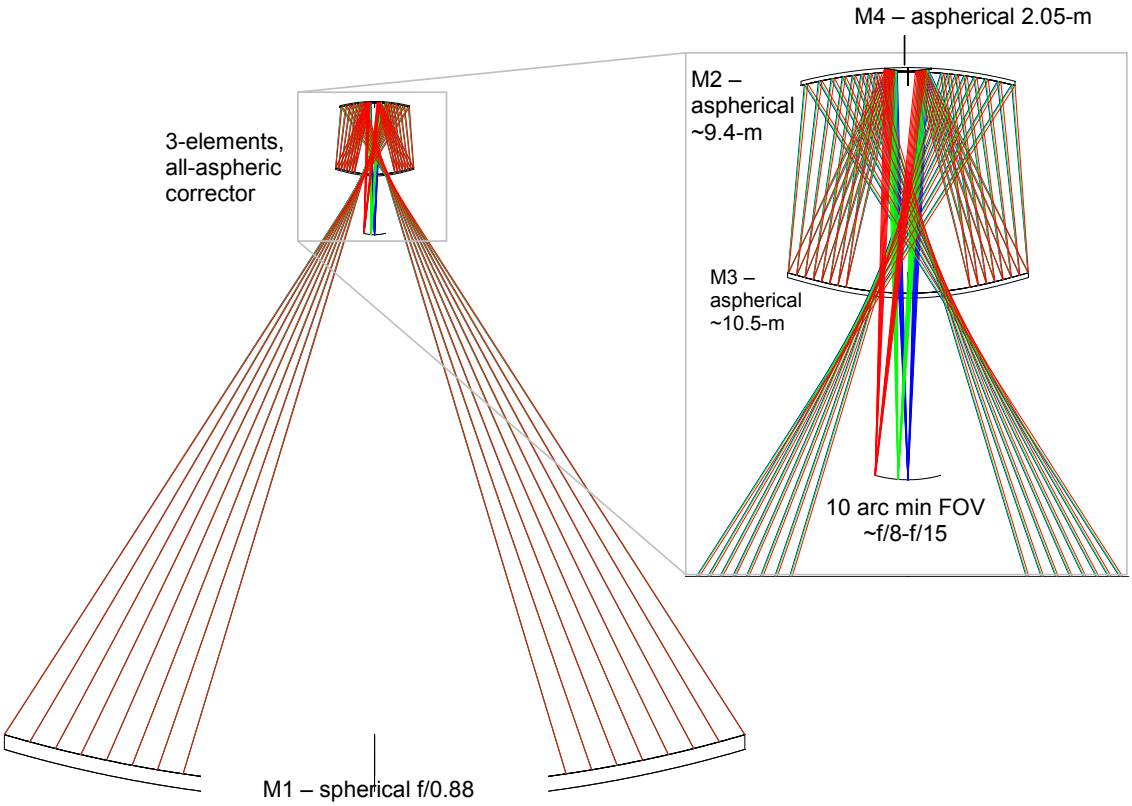

Figure 6-7. Four-mirror solution; f/0.89 spherical primary mirror .

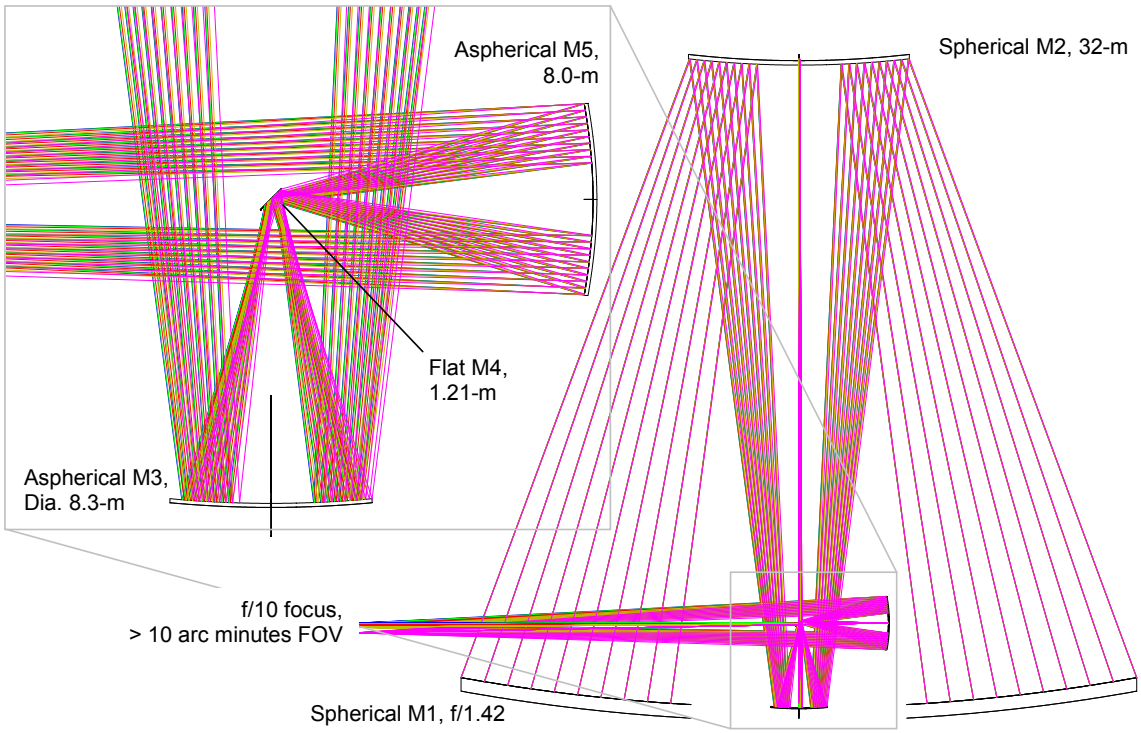

Figure 6-8. 5-mirror solution, f/1.42 spherical primary mirror.

	Design No	1	2	3	4
Mandatory requirements (*)		P / F	P / F	P / F	P / F
1	Field aberrations over the science field (3 arc minutes diameter) shall be axisymmetrical or negligible.	P	P	P	P
2	Diffraction-limited (Strehl Ratio ≥ 0.80, λ=0.5μm) over at least 1 arc minute FOV.	P	**F**	**F**	P
3	The field of view (diameter) available for adaptive optics wavefront sensing shall be 6 arc minutes.	P	P	**F**	P
4	The design shall provide suitable surfaces for active optics, including deformable mirror(s), active centring, focusing, and field stabilization	P	P	P	P
5	Monolithic mirrors shall be less than 8.3m in diameter	P	P	P	P
6	Field stabilization shall be done in a pupil image	P	P	**F**	P
7	The design shall provide a suitably located surface for single-conjugate IR SCAO and GLAO.	P	P	P	P
Requirement / characteristic	**Weight**	**Rating**	**Rating**	**Rating**	**Rating**
1	Diffraction-limited FOV	5	3	0	0	5
2	Total field of view (0.1 arc seconds RMS image quality or unacceptable vignetting)	5	4	0	0	2
3	Optical quality at edge of field of view	3	4	0	0	5
4	Field curvature	3	0	3	2	2
5	Focal ratio	3	5	5	0	0
6	Maximum monolithic mirror diameter	5	1	5	3	4
7	Emissivity (number of surfaces)	5	3	7	5	5
8	Sensitivity to M1-M2 decenters	5	4	1	4	3
9	Sensitivity to M1-M2 axial despace	5	3	3	3	3
10	Sensitivity to decenters of M3, M4, …	3	3	5	3	3
11	Sensitivity to axial despace of M3, M4,	3	2	5	2	2
12	Central obscuration	3	2	5	2	2
13	Vignetting in the science field	5	5	5	5	5
14	Vignetting outside the science field	2	5	5	5	5
15	M1-M2 separation	5	4	4	4	4
16	Structure aspect ratio	4	3	4	3	3
17	Built-in IR adaptive optics (SCAO & GLAO)	5	3	5	5	5
18	Built-in IR MCAO	5	3	0	0	0
19	Separation of active and adaptive functions	5	3	0	0	0
20	SCAO / GLAO mirror dimensions	5	5	1	0	1
21	MCAO mirrors dimensions	5	2	0	0	0
22	Intermediate focus for AO calibration	2	3	0	0	3
23	Number of segmented mirrors	4	3	5	3	3
24	Feasibility of secondary mirror	5	5	1	5	5
25	Difficulty of fabricating most aspheric mirror(s)	4	1	1	1	3
26	Compatibility with serial production & maintenance of segments	5	5	1	5	1
27	Segments optical testing	4	5	1	5	1
28	Compatibility with lightweight segments	3	5	1	5	0
29	Baffling options	2	4	0	1	1
30	Allowable design volume for active/adaptive units	2	2	5	5	5
31	Allowable design volume for instruments	3	5	3	5	3
32	Access to gravity-stable platform(s)	3	0	0	0	0
33	Rapid switch between permanently mounted instruments possible (without additional relay optics).	2	5	0	0	0
SCORE (Σ Weight x Rating); maximum = 640			**429**	**310**	**322**	**334**

Table 6-2. Ratings for designs No 1 to 4. (*) P=Pass; F=Fail.

6.2.2 Baseline design

The baseline optical design is described in RD2; its overall geometry is shown in Figure 6-9 and the mechanical implementation in Figure 6-10. This baseline is a recent update of the former one (RD1), with a focal ratio of the primary mirror reduced from the former f/1.42 to the current f/1.25. At the time of writing of this document, the update has not yet been propagated to all areas of the system. Most notably, instruments concepts are still based on the former design. Differences are however minor and unlikely to have any significant impact on instrument concepts.

The present section concerns optical design only; considerations related to pupil and segments geometries are addressed in section 6.5.1.1.

The essential features of the baseline optical design are

- A spherical, f/1.25 primary mirror;
- A flat, 25.8-m secondary mirror;
- A four-elements corrector, with two active mirrors (M3 and M4), 8-m class, and two adaptive ones (M5 and M6), with diameters of ~2.5 and 4.0-m, respectively.

Prescription data are given in Table 6-3. The image surface is given as a conic, for minimum rms image size on the wavefront sensors[47]. The M1-M2 separation is such that the diameter of the secondary mirror is twice the size of a structural module.

The diameters are indicative only and will have to be re-calculated, taking into account tolerances on vignetting for wavefront sensing with natural and laser guide stars. These tolerances have not been calculated at the time of writing of this document; it is plausible that the diameters of surfaces M3 and M5 will eventually be reduced.

Fictive surfaces in the design listing (No 1, 4, 7, and 8) correspond to M2 obscuration, M4 hole, M3 hole, and M6 hole, respectively.

The image quality at the edge of the 10 arc minutes, f/6 focus is 0.052 arc seconds rms (see section 6.3.1 for detailed image quality data). The linear field diameter is 1780.7 mm and the image scale on-axis is 2.924 mm / arc second.

Central obscuration is 35% linear. Central obscuration and field of view are related through the dimension of M3 central hole; a larger obscuration would permit a larger field of view, which is limited by vignetting (M3 central hole) rather than by optical quality.

The entrance pupil is the primary mirror and the exit pupil is co-located with M6. The backfocal distance (M6 i.e. exit pupil to focus) is 13994.53 mm.

The strengths of this design are essentially

- Excellent image quality in the field of view;
- Low sensitivity to the (flat) secondary mirror decenters;
- Availability of two surfaces, M6 and M5, for adaptive compensation;
- Availability of two surfaces, M3 and M4, for active optics (low time frequency, high amplitude deformation of flexible mirrors);
- Availability of all wavefront control functions, including field stabilization, with no more than 6 surfaces.
- Compatibility with serially produced segments (spherical primary, flat secondary);
- Baffling opportunities.

Stringent centering tolerances inevitably appear, albeit within the corrector, which is favourably located. A complete sensitivity analysis is provided in section 6.3.5.

[47] Moving the sensors on a spherical rather than conic surface does however not yield to significant errors.

The main weaknesses of the design are:

- Tilted AO mirror, limiting performance with GLAO;
- Fairly short focal ratio;
- Fairly strong field curvature, concave in the direction of propagation of light.
- Large, segmented secondary mirror;
- Limited design space for M6 AO unit;
- No gravity-stable instrument location;
- Extreme aspherization of mirror M4 (12.7 mm deviation from best fitting sphere).

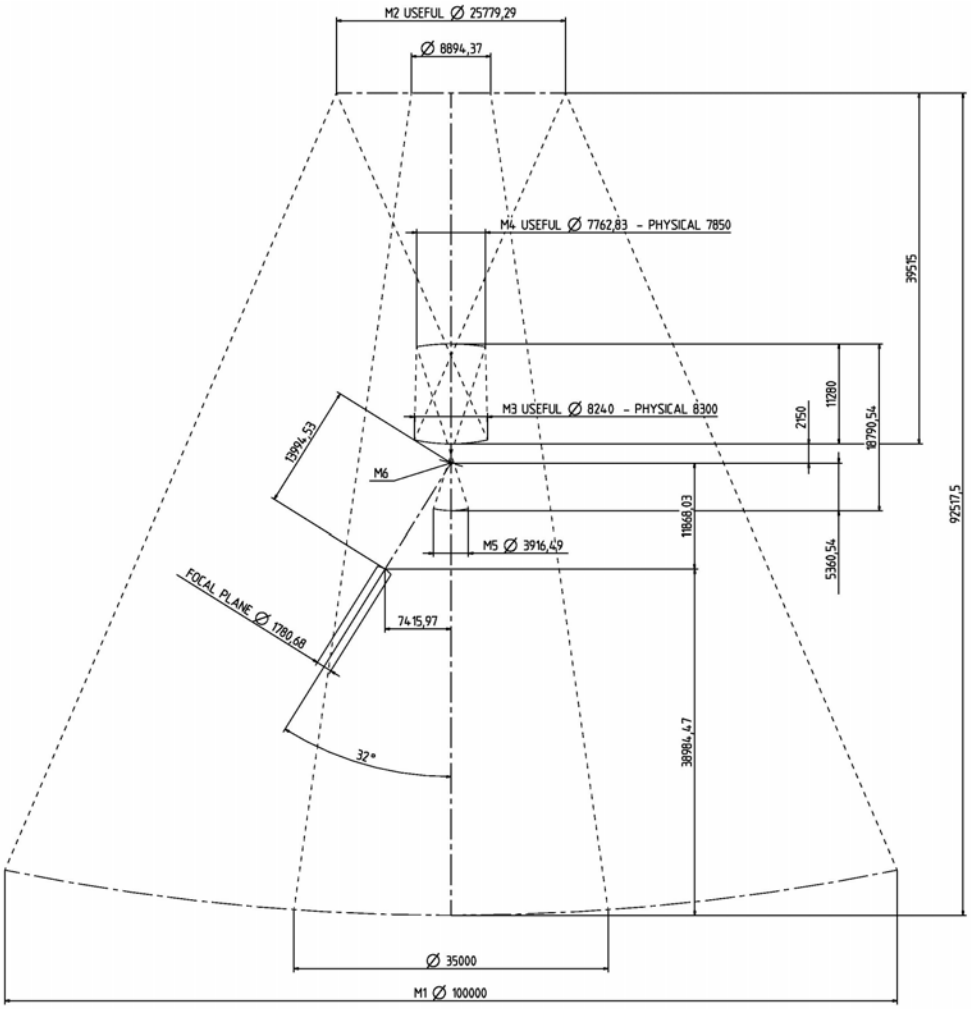

Figure 6-9. Baseline optical design, major dimensions.

Field aberrations include high order terms and are not accurately described with 36 Zernike Polynomials.

Further optimization of the design seems possible to some extent; a slightly longer focal ratio (~f/6.5) would probably be possible if required. The secondary mirror dimension (25.8-m) being smaller than the linear obscuration (35%), it is possible to relax the focal ratio of the primary mirror to f/1.32 without increasing the mirrors spearation, and with subsequent advantages in terms of feasibility of M4, and possibly a reduced tilt and increased design space of M6. The increased secondary mirror diameter (30-m) would, however, no longer be an integer multiple of

the standard size of the structural modules, thus implying a more complex interface to the telescope structure.

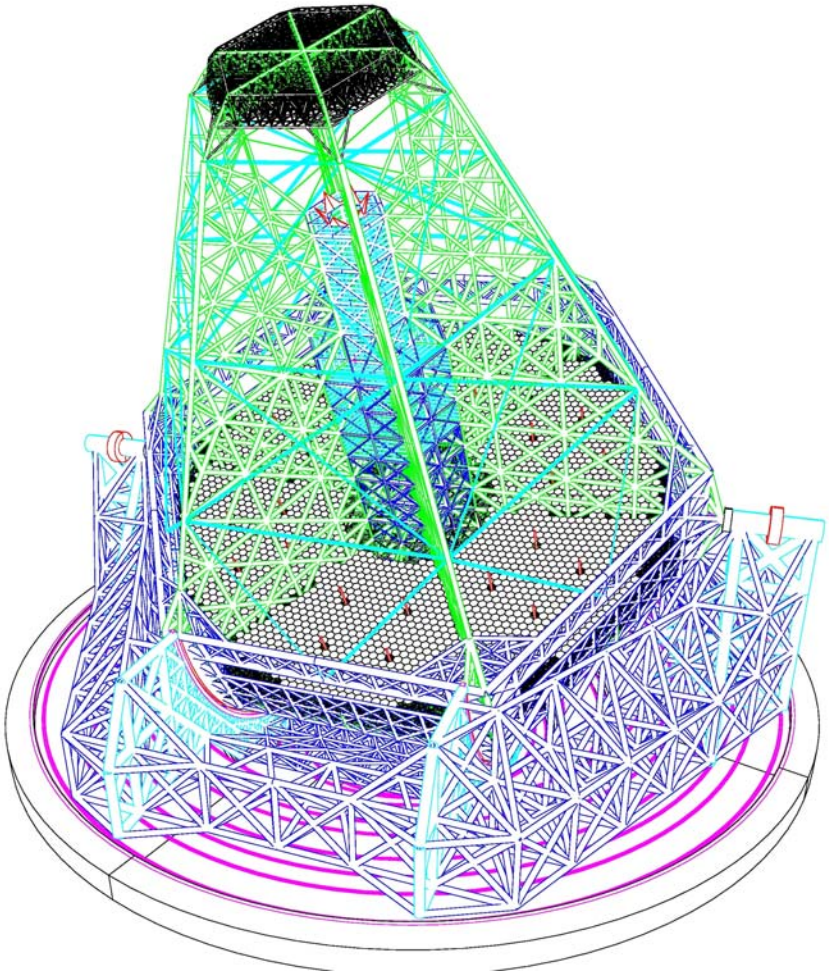

Figure 6-10. Baseline design, optomechanical implementation.

System/Prescription Data

```
File OWL-1250-92518-100m-11.ZMX
Surfaces                :              11
Stop                    :               2
System Aperture         : Entrance Pupil Diameter = 100000
Effective Focal Length  :        602364.9 (in image space)
Entrance Pupil Diameter :          100000
Entrance Pupil Position :         92517.5
Exit Pupil Diameter     :        2316.556
Exit Pupil Position     :       -13968.31
Field Type              : Angle in degrees
Maximum Radial Field    :      0.08333333
Primary Wavelength      :             0.5 µm
Lens Units              :   Millimeters
```

SURFACE DATA SUMMARY:

Surf	Type	Radius	Thickness	Glass	Diameter	Conic
OBJ	STANDARD	Infinity	Infinity		0	0
1	STANDARD	Infinity	92517.5		100254.4	0
STO	STANDARD	-250000	-92517.5	MIRROR	100000	0
3	STANDARD	Infinity	28235	MIRROR	25779.29	0
4	STANDARD	Infinity	11280		1820.15	0
5	EVENASPH	-18690	-11280	MIRROR	8241.896	0
6	EVENASPH	19970	11280	MIRROR	7762.828	0

```
7      STANDARD    Infinity          2150                 1665.273          0
8      STANDARD    Infinity          5360.54               721.3222         0
9      EVENASPH       -8504         -5360.54   MIRROR     3916.487          0
10     STANDARD    Infinity         13994.53   MIRROR     2608.574          0
IMA    STANDARD        2209.788                           1780.683     -1.295298
SURFACE DATA DETAIL:

Surface OBJ     : STANDARD
Surface   1     : STANDARD M2 OBSCURATION
 Aperture       : Circular Aperture
 Minimum Radius :         15000
 Maximum Radius :         51000
Surface STO     : STANDARD M1
 Aperture       : Circular Aperture
 Minimum Radius :         17500
 Maximum Radius :         50200
Surface   3     : STANDARD M2
 Aperture       : Circular Aperture
 Minimum Radius :          4400
 Maximum Radius :         12900
Surface   4     : STANDARD HOLE M4
Surface   5     : EVENASPH M3
 Coeff on r  2  :                0
 Coeff on r  4  :   9.9615208e-014
 Coeff on r  6  :  -7.4588943e-021
 Coeff on r  8  :   5.0822357e-028
 Coeff on r 10  :  -2.6489928e-035
 Coeff on r 12  :   9.3682602e-043
 Coeff on r 14  :  -1.9628184e-050
 Coeff on r 16  :   1.8115665e-058
 Aperture       : Circular Aperture
 Minimum Radius :             0
 Maximum Radius :          4090
Surface   6     : EVENASPH M4
 Coeff on r  2  :                0
 Coeff on r  4  :  -2.0050643e-013
 Coeff on r  6  :  -8.3000578e-022
 Coeff on r  8  :  -4.8126671e-029
 Coeff on r 10  :   1.8076695e-036
 Coeff on r 12  :  -2.7869116e-044
 Coeff on r 14  :                0
 Coeff on r 16  :                0
 Aperture       : Circular Aperture
 Minimum Radius :             0
 Maximum Radius :          3890
Surface   7     : STANDARD HOLE M3
Surface   8     : STANDARD HOLE M6
Surface   9     : EVENASPH M5
 Coeff on r  2  :                0
 Coeff on r  4  :   1.2236767e-013
 Coeff on r  6  :  -1.1194562e-020
 Coeff on r  8  :   8.8474514e-027
 Coeff on r 10  :  -1.2274556e-034
 Coeff on r 12  :  -1.1526053e-039
 Coeff on r 14  :   3.4012362e-046
 Coeff on r 16  :  -3.0833076e-053
 Aperture       : Circular Aperture
 Minimum Radius :           210
 Maximum Radius :          2000
Surface  10     : STANDARD M6
 Tilt/Decenter  : Tilt X = 16
 Aperture       : Elliptical Aperture
 X Half Width   :          1220
 Y Half Width   :          1330
Surface IMA     : STANDARD IMAGE
```

Table 6-3. Baseline design, optical prescription.

6.2.3 Optional corrector

For IR applications beyond 2.2 μm and with limited field requirements, the nominal corrector could be replaced by a simpler 2-mirror design (see Appendix 9). The two mirrors of the corrector would be 6.1 and 4.1-m diameter, respectively. They would receive IR-optimized reflective coatings. The 4.1-m mirror (M4) is conjugated to the pupil and could therefore provide either ground layer or single conjugate adaptive correction. In view of the long wavelength range, actuator interspacing needs not to be pushed beyond current technology. A 1.2-m spacing in the entrance pupil would correspond to ~49 mm interactuator spacing on M4 and a total of 5,054 actuators. According to simulations the expected AO performance would be

r_0~0.19-m	(seeing ~0.5 arc secs at 0.5 μm)	λ = 5 μm	Strehl Ratio ~87%
		λ = 10 μm	Strehl Ratio ~96%
r_0~0.10-m	(seeing ~1.0 arc secs at 0.5 μm)	λ = 5 μm	Strehl Ratio ~71%
		λ = 10 μm	Strehl Ratio ~91%

Under favorable seeing conditions (less than ~0.5 arc seconds in the visible i.e. r_o~1.2-m in K band), performance would still be reasonable in K band. A six-petal segmentation of M4 would be possible –being it an image of the entrance pupil- with maximum gap size of 40 mm.

6.2.4 Reduced aperture designs

Optical solutions have been explored at notional level, in the assumption of a relaxed specification on aperture size (see RD48 for a full report). At 80-m, the 4-mirror design shown in section 6.2.1, Figure 6-7, does no longer require monolithic mirrors larger than 8-m. Several possible configurations between f/15 and f/30 have been briefly evaluated. Although further optimization might be possible, the diffraction-limited field of view is rather limited and the location of the science instrumentation rather inconvenient.

At 60-m the palette of options becomes wider. In addition, a segmented secondary mirror may no longer be required. Figure 6-11 shows a 4-mirror f/15.5 design. It is essentially a beam compressor with spherical 60-m primary and aspherical 8-m convex secondary mirrors, combined with a Gregorian re-imager. Optical design data are given in Table 6-4. The field of view is 10 arc minutes diameter. The linear obscuration is 33% and set by the quaternary mirror. Mirror M4, with a diameter of 2.7-m and located in a pupil, would be suitable for single conjugate adaptive optics. The diffraction-limited field of view is close to 2 arc minutes diameter in the visible and close to 4 arc minutes in K band (see Table 6-5). A potential disadvantage of this design is its relatively strong sensitivity to decentres.

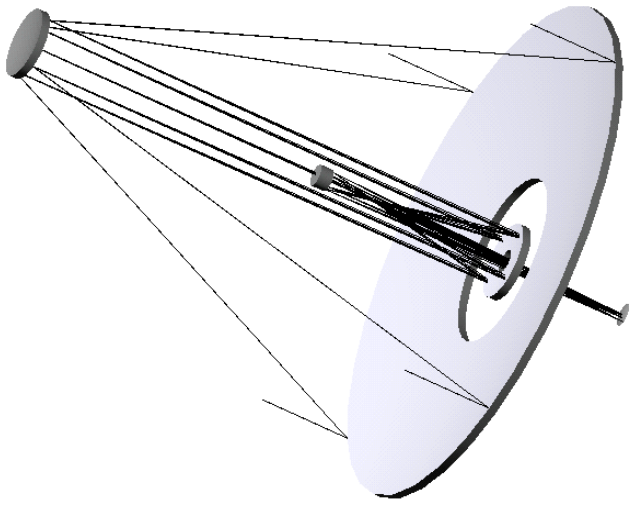

Figure 6-11. 4-mirror f/15 design, 60-m aperture.

Mirror	Diameter (m)	Radius of curvature (m)	Profile	Distance to next surface (mm)
M1	60.0	-145000	Sphere	61500
M2	8.2	-2057	Asphere	61500
M3	8.5	-3571	Asphere	23265
M4	2.6	-697	Asphere / adaptive	38500
Image	2.7	5.360	Sphere	-

Table 6-4. 4-mirror f/15 design, 60-m aperture; optical prescription.

Fabrication of the convex, aspherical secondary mirror is difficult but a possible test set-up has been calculated. The mirror would be tested at centre of curvature in double pass (Figure 6-12). The nulling system is made of a 650-mm aspheric, diamond-turned mirror combined with a 11.4-m spherical mirror. The latter could be undersized if stitching of subapertures could be tolerated, or segmented (e.g. 6 petals).

Field of view (radius)	RMS wavefront error (nm)	Strehl Ratio at 500 nm	Strehl Ratio at 2000 nm
On-axis	9	0.987	0.999
0.5 arc min	11	0.982	0.999
1.0 arc min	44	0.732	0.981
2.0 arc min	190	0.003	0.699
3.0 arc min	446	0.000	0.140
4.0 arc min	810	0.000	0.002
5.0 arc min	1350	0.000	0.000

Table 6-5. 4-mirror f/15, 60-m aperture design. Nominal optical quality.

Mirrors M3 and M4 are concave and could probably be tested through Oeffner compensators.

A modified, folded f/20 version of this design allows the beams to be folded along the elevation axis, thereby providing 2 convenient Nasmyth foci, in addition to the Cassegrain one.

A solution with a parabolic, f/0.75 primary mirror has also been briefly evaluated (Figure 6-13). The design is extremely compact, and therefore very favorable in relation to structural stiffness and enclosure cost. The primary mirror being parabolic, M1-M2 decentres do not introduce coma but astigmatism only (linear with the field of view). However, depointing is still a potential issue. Nominal optical quality is excellent, with a diffraction-limited (Strehl Ratio ≥ 0.80) field of view in excess of 3 arc minutes in the visible and 6 arc minutes in K band.

Off-axis parabolic segments could be tested in double pass against a reference flat. Matching of the segments indidivual curvature is however an issue and no convenient solution have been found so far.

Reduced aperture designs are, at the time of writing of this document, very notional.

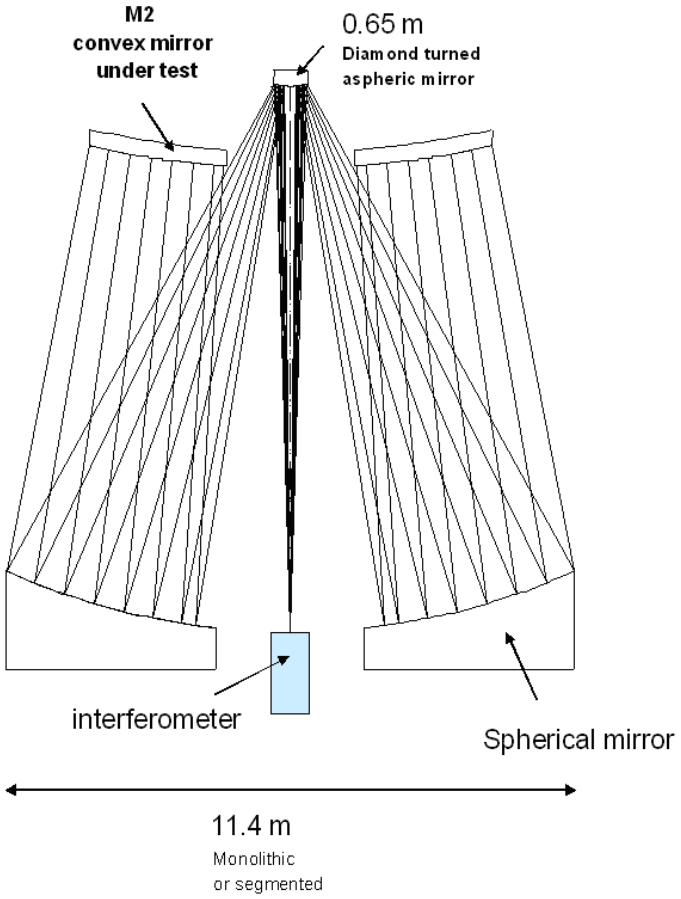

Figure 6-12. Optical test set-up for the testing of a convex, aspherical 8-m class mirror.

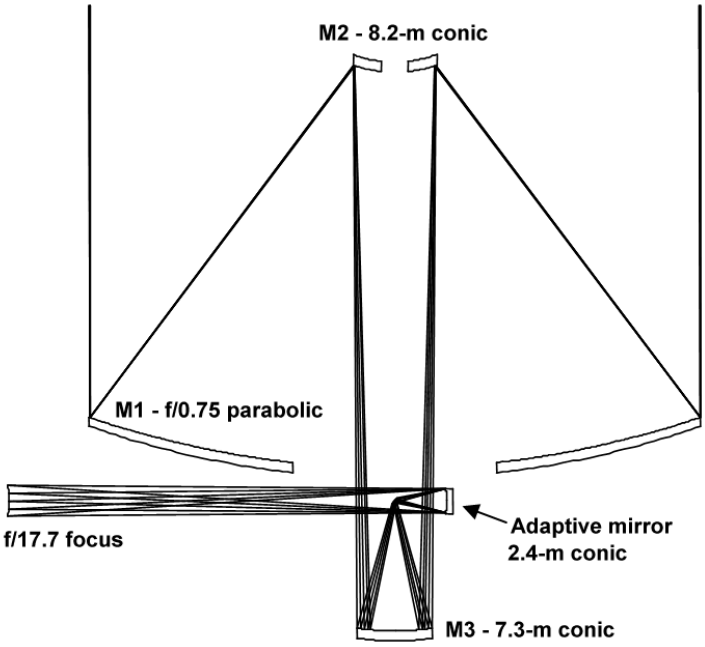

Figure 6-13. 60-m four mirror design with f/0.75 parabolic primary mirror.

6.2.5 Future design iterations

According to plans, the preliminary design phase will start with a re-assessment of the current optical design solution, taking into account, in particular, results from instrument studies and AO simulations.

At the time of writing of this document, exploratory work has already begun with a view to producing a fully co-axial design, thereby removing the undesirable tilt of M6 conjugate and allowing, if requested, to transport a small part of the field, by way of additional relay optics, down to the elevation axis and eventually to Nasmyth-type platforms.

Effort is currently concentrating on a solution whereby the mirror M6 is coaxial, spherical and convex. Optical quality in the field of view is excellent but transferring a 10 arc minutes field of view through a hole in M5 seems impossible unless M5 hole is enlarged to such proportion that the beam footprints on M5 will be vignetted outside a 5-6 arc minutes field of view. This vignetting does not affect science targets, but its implication on the active control loops needs to be assessed. In practice this makes the reconstruction of the desired M4 and M3 active deformation more complex, but the availability of several off-axis guide stars for active optics should allow sufficient overlap between beams footprints to permit accurate fitting of the active optics modes. Indeed the situation is more favorable than in the VLT, where significant vignetting by the tertiary mirror occurs beyond 10 arc minutes off-axis, and where only one wavefront sensor is available. On the negative side, this design requires a reduction of the focal ratio to ~f/4-f/5 in order to avoid increasing obscuration much beyond 35%.

Another design iteration which is under way at the time of writing of this document is a minor update of the baseline, with a f/1.32 instead of f/1.25 primary mirror, and a 30-m flat secondary mirror. It is expected that this update will allow more design space for M6 unit, a slightly longer focal ratio (~f/6.5 instead of f/6), and somewhat smaller field aberrations and aspherization of M4.

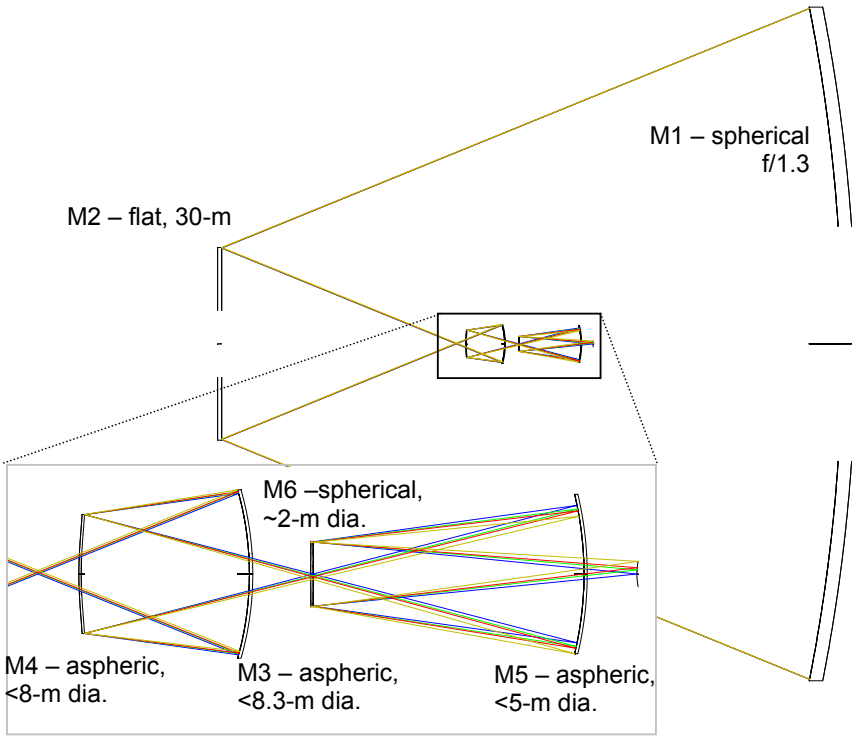

Figure 6-14. Coaxial design with f/5 focus. Field of view 6 arc minutes, f/1.3 primary mirror.

6.3 Optical characteristics

6.3.1 Nominal optical quality

The optical quality (Strehl Ratio) of the baseline 6-mirror design is given in Figure 6-15 (Strehl Ratio, up to 3 arc minutes off-axis), Figure 6-16 (RMS spot size up to 5 arc minutes off-axis), and Figure 6-17 (wavefront RMS, up to 5 arc minutes off-axis). Results are summarized in Table 6-6.

Monochromatic Point Spread Functions at 0.5 and 2.2 microns are shown in Figure 6-18 and Figure 6-20; ensquared energy in Figure 6-19 and Figure 6-21. None of these figures takes segmentation into account; the pupil shape is annular. It should be noted that non-axisymmetrical diffraction artefacts (Figure 6-18 and Figure 6-20) will be blurred by differential field-pupil rotation.

Diffraction-limited field of view (Strehl Ratio ≥ 0.80)		
λ=0.5 μm (on curved field with R=2209.8 mm)	142 arc seconds	(diameter)
λ=2.2 μm (on curved field with R=2215.4 mm)	245 arc seconds	(diameter)
λ=5.0 μm (on curved field with R=2243.1 mm)	360 arc seconds	(diameter)
Image quality at edge of field		
Wavefront RMS	1.476 μm	
RMS spot size	0.052 arc seconds	

Table 6-6. Baseline design, optical quality.

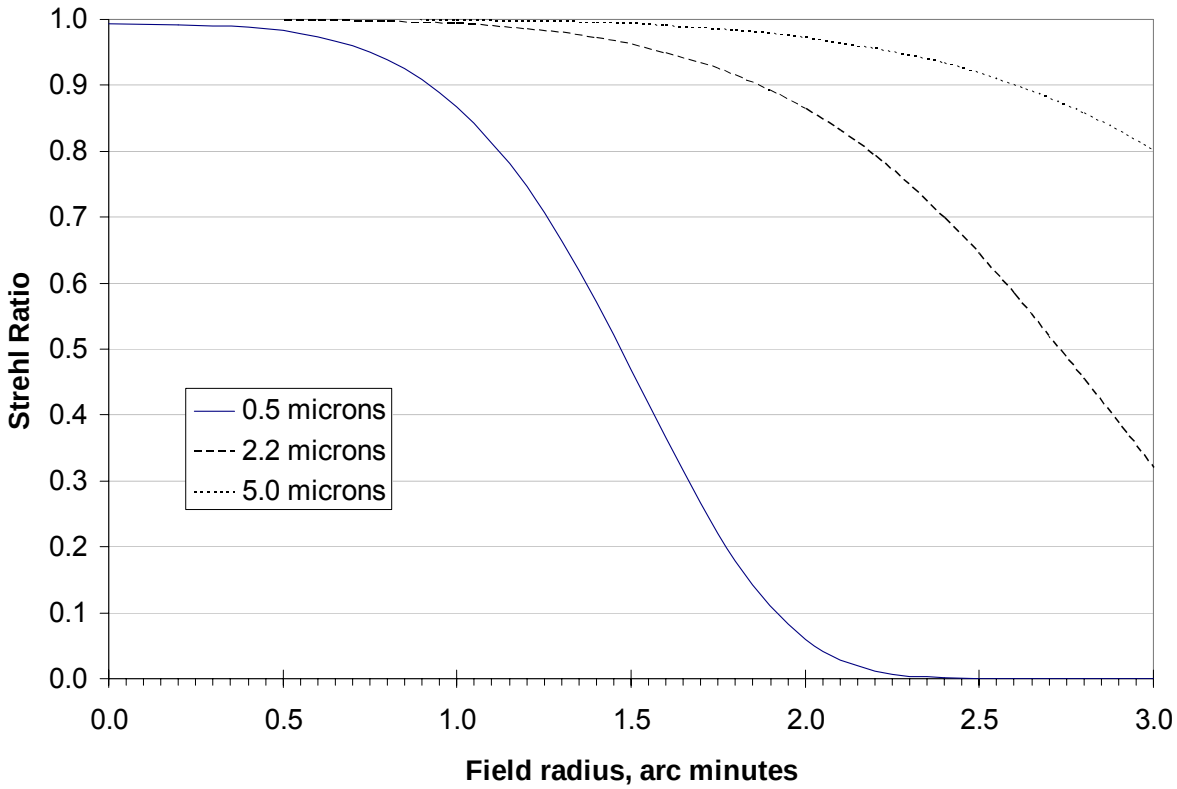

Figure 6-15. Baseline design; Strehl Ratio vs field of view.

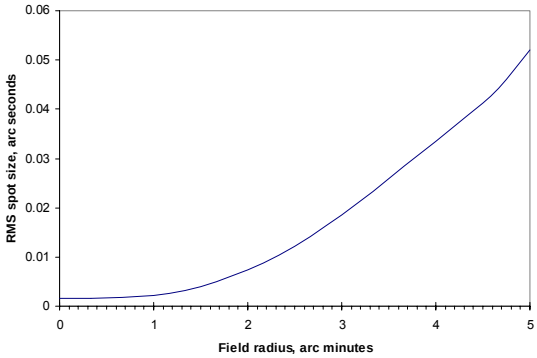

Figure 6-16. Baseline design; rms spot size (arc seconds) vs field radius.

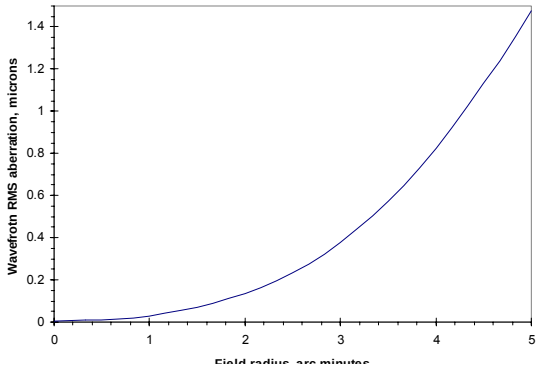

Figure 6-17. RMS wavefront error (microns) vs field radius.

Distortion is fairly small (1.31% at the edge of the field, see Figure 6-22). Distortion is defined here as $(\rho-\rho_p)/\rho_p$, where ρ is the radial coordinate of the impact of the real chief ray onto the image surface, and ρ_p the radial coordinate of the impact of the paraxial chief ray. A calculation based on image centroid may lead to slightly different figures.

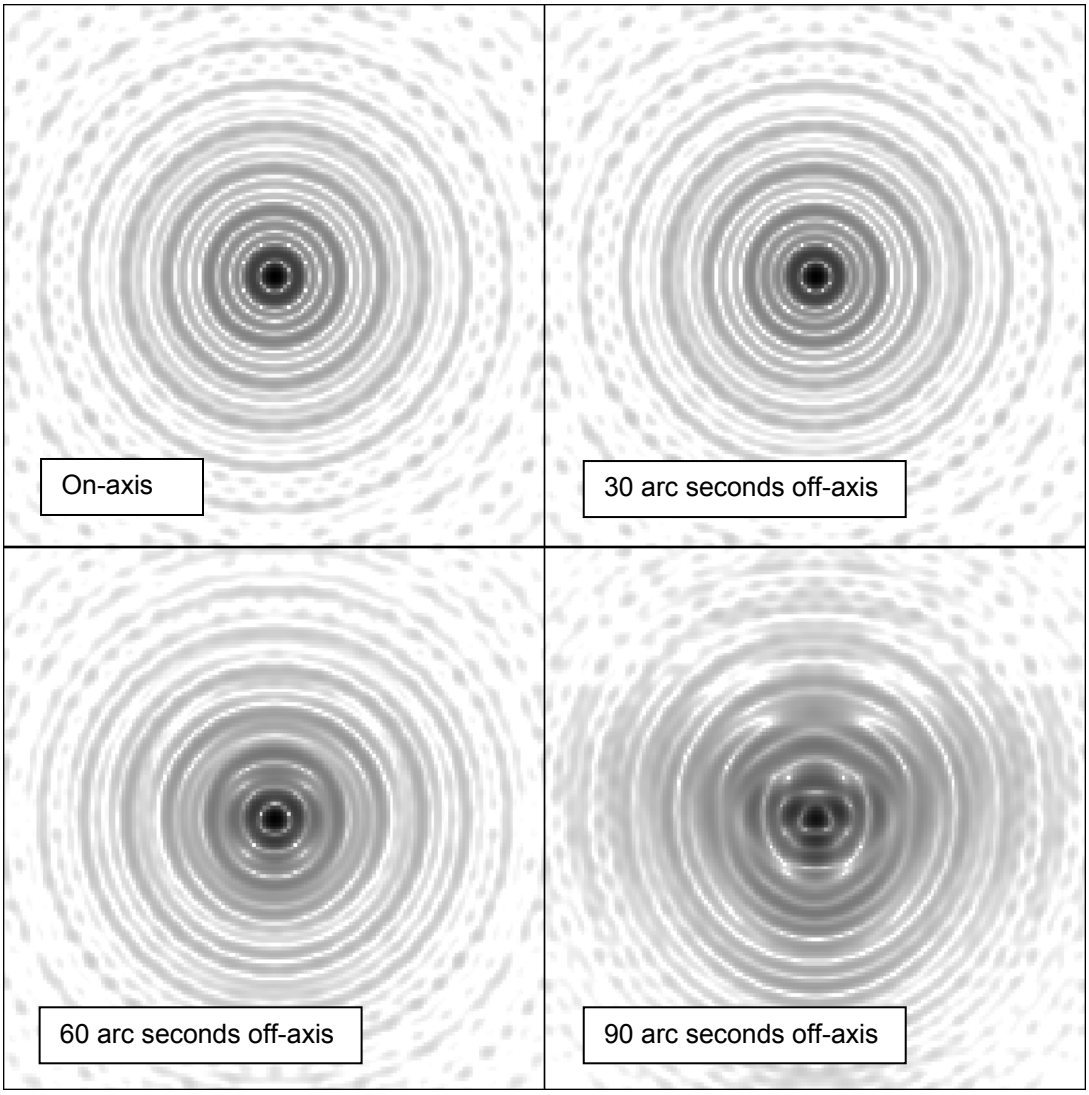

Figure 6-18. Point Spread functions at 0.5 microns. Box size 0.040 arc seconds.

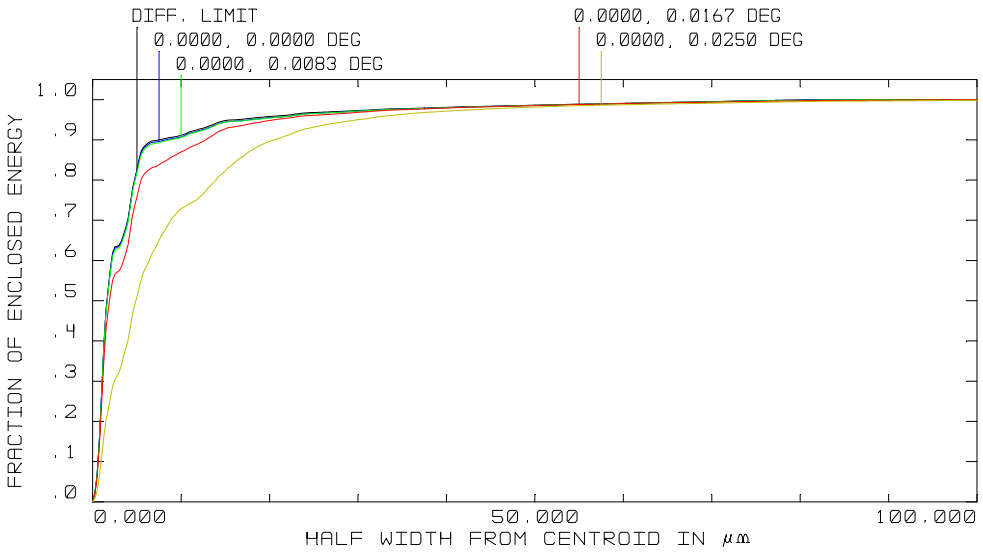

Figure 6-19. Ensquared energy at 0.5 microns. Scale: 100 microns = 0.0342 arc seconds.

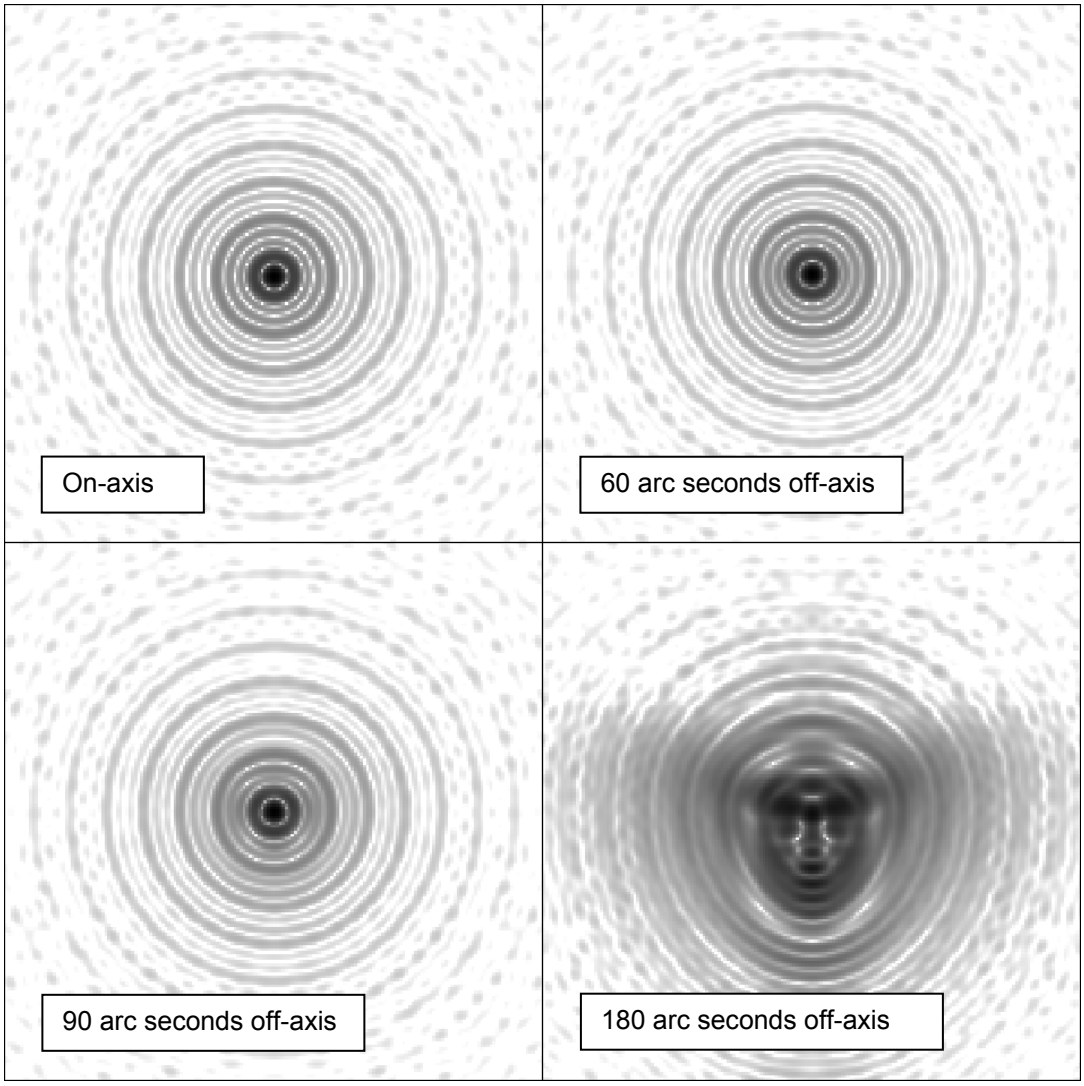

Figure 6-20. Point Spread functions at 2.2 microns. Box size 0.200 arc seconds.

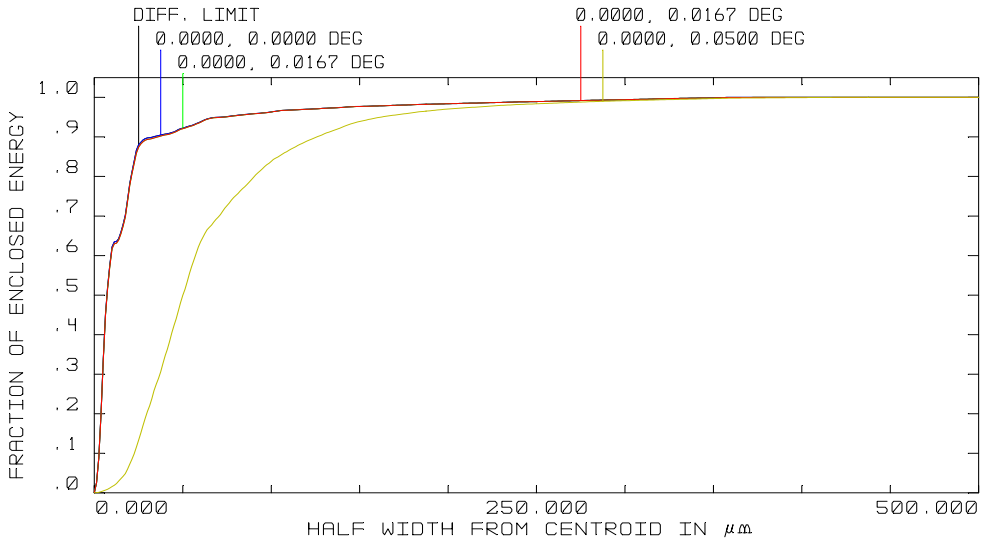

Figure 6-21. Ensquared energy at 2.2 microns. Scale: 500 microns=0.171 arc seconds.

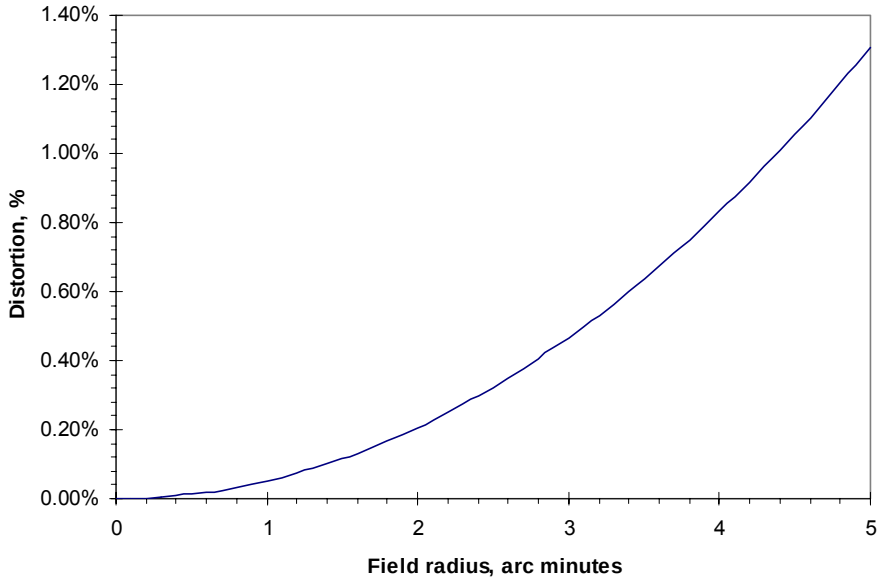

Figure 6-22. Distortion.

6.3.2 Vignetting

With the dimensions given in section 6.2.2, vignetting is completely negligible over the entire 10 arc minutes field of view. It may, however, be profitable to allow slight vignetting outside the 6 arc minutes diameter of the the Adaptive Optics control field of view, or even to allow vignetting to start at 3 arc minutes (outside the science field). The useful diameter of M5 as a function of the unvignetted field is

Unvignetted field	10 arc minutes	M5 diameter	3916.4 mm
Unvignetted field	6 arc minutes	M5 diameter	3629.0 mm
Unvignetted field	3 arc minutes	M5 diameter	3412.6 mm

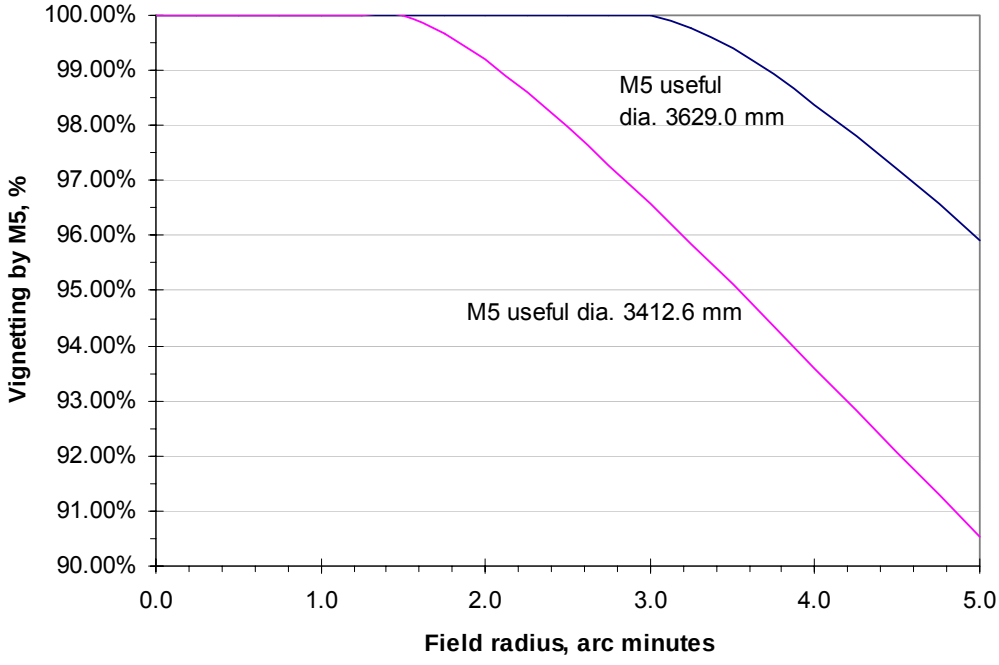

Figure 6-23. Vignetting by M5 as a function of M5 diameter.

Figure 6-23 shows the vignetting by M5, in the field of view for the two possible sizes of M5. The effect on active and possibly adaptive wavefront sensing ought to be small if not entirely negligible. It should be noted that the outer rim of M5, which would not be seen by the adaptive optics wavefront sensors, need to be controlled by the active optics ones. It would be simpler and probably better to allow vignetting of the corresponding light beams (outside the central 6 arc minutes i.e. M5 useful diameter 3629 mm instead of 3916.4 mm). A decision can however not be taken at this point, as the full implications on re-imaging of laser guide stars need to be assessed.

A similar reasoning applies with M3. The useful diameter is 8241.8 mm for an unvignetted field of view of 10 arc minutes; it can be reduced to 7963.8 mm if vignetting is allowed outside the central 3 arc minutes, with a maximum of 1.4% at the edge of the 10 arc minutes full field.

6.3.3 Stray light and baffling

The 4-mirror OWL corrector gives ample opportunity to provide good baffling, avoiding any risk of getting skylight not coming through the right mirror sequence, a must for a telescope operating in open air. The simple set of baffles shown in Figure 6-24 is fully adequate: although the first of the two intermediate images suffer from huge geometrical aberrations, the two field stops (defined by these baffles and the hole in M6) and the two pupil stops (defined by M4 and M6) are sufficient to prevent geometrical stray light coming from the sky (e.g. from the Moon) to be seen by the telescope focal plane. Good performance in terms of stray light is thus expected in the non-thermal spectral domain (Visible & near-IR up to the “blue” part of the H-band). Note however that a very bright source, and in particular the Moon, will also give some diffuse light depending on the cleanliness of the telescope mirrors, especially M1. This may restrict sky coverage during bright Moon periods for some type of observations (short wavelengths, coarse spatial resolution and/or small spectral resolution). A detailed analysis with adequate software tools is foreseen in Phase B.

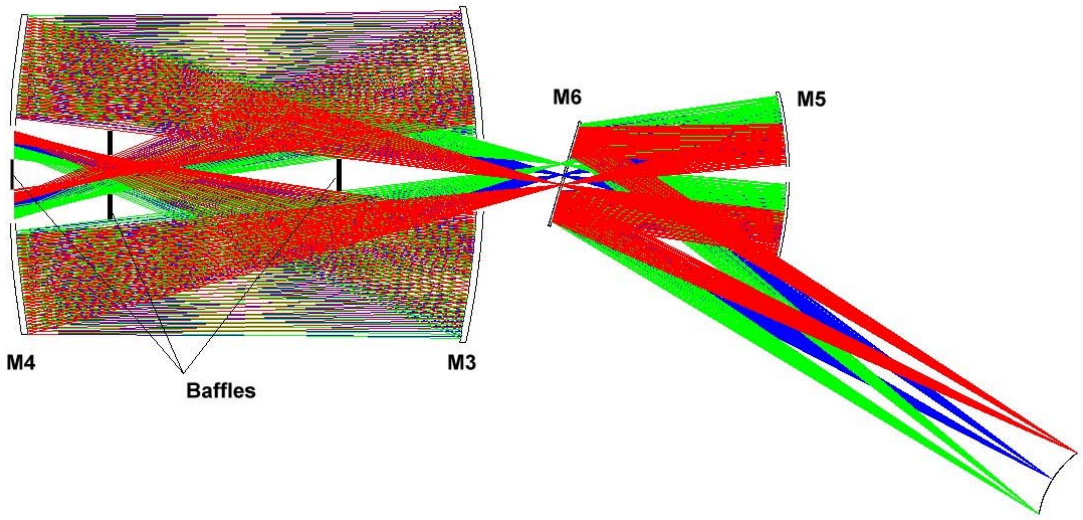

Figure 6-24. Possible set of baffles.

In the thermal IR on the other hand, it is essential that a cold stop be put on an optically good image of the pupil to mask for the strong thermal radiation coming from the corrector inner mechanics. This is a non trivial optical requirement put on each instrument project. It should be relatively easy to meet for multi-imagers and integral field spectrometers working at high spatial resolution since their linear field of view is small. This is more difficult for wide-field imaging, and case by case studies with the proper software tools are needed during Phase B.

6.3.4 Emissivity

The expected emissivity at 2.2 μm is given in Table 6-7. All obscured areas are assumed to have 100% emissivity. The figure without pupil mask (2nd column) is given for background information only. The pupil mask is shown in Figure 6-25. We assume 3% emissivity with classical Al coatings (3rd column), 1% with optional gold coatings, and a longitudinal ADC with 1% emissivity per interface glass-air. The overall emissivity figure is plausibly pessimistic as the facing-down secondary mirror and the fairly well protected corrector surfaces should normally be cleaner than the primary mirror. In addition, a cold plate located behind the primary and secondary mirrors may reduce the emissivity by the gaps.

Source	w/o pupil mask	with pupil mask	Pupil mask + Gold coated M2-M4	Pupil mask + Optional corrector	Pupil mask + Optional corrector + gold-coated M2
M1	3.0%	3.0%	3.0%	3.0%	3.0%
M2	3.0%	3.0%	1.0%	3.0%	1.0%
M3	3.0%	3.0%	1.0%	1.0%	1.0%
M4	3.0%	3.0%	1.0%	1.0%	1.0%
M5	3.0%	3.0%	3.0%		
M6	3.0%	3.0%	3.0%		
M1+ M2 gaps	1.2%	1.2%	1.2%	1.2%	1.2%
Ropes	1.1%	1.1%	1.1%	1.1%	1.1%
Spiders + missing segments	6.1%				
Central obscuration	11.9%				
Subtotal w/o ADC	**38.3%**	**20.3%**	**14.3%**	**10.3%**	**8.3%**
Total	**42.3%**	**24.3%**	**18.3%**	**14.3%**	**12.3%**

Table 6-7. Expected emissivity at 2.2 μm, classical Al or Au coatings.

Source	w/o pupil mask	with pupil mask	Pupil mask + Optional correcor
M1	1.5%	1.5%	1.5%
M2	1.5%	1.5%	1.5%
M3	1.5%	1.5%	1.5%
M4	1.5%	1.5%	1.5%
M5	1.5%	1.5%	
M6	1.5%	1.5%	
M1+M2 gaps	1.2%	1.2%	1.2%
Ropes	1.1%	1.1%	1.1%
Spiders + missing segments	6.1%		
Central obscuration	11.9%		
Subtotal w/o ADC	**29.3%**	**11.3%**	**8.3%**
ADC (1% per surface)	4.0%	4.0%	4.0%
Total	**33.3%**	**15.3%**	**12.3%**

Table 6-8. Expected emissivity at 2.2 μm, Gemini enhanced Ag coatings.

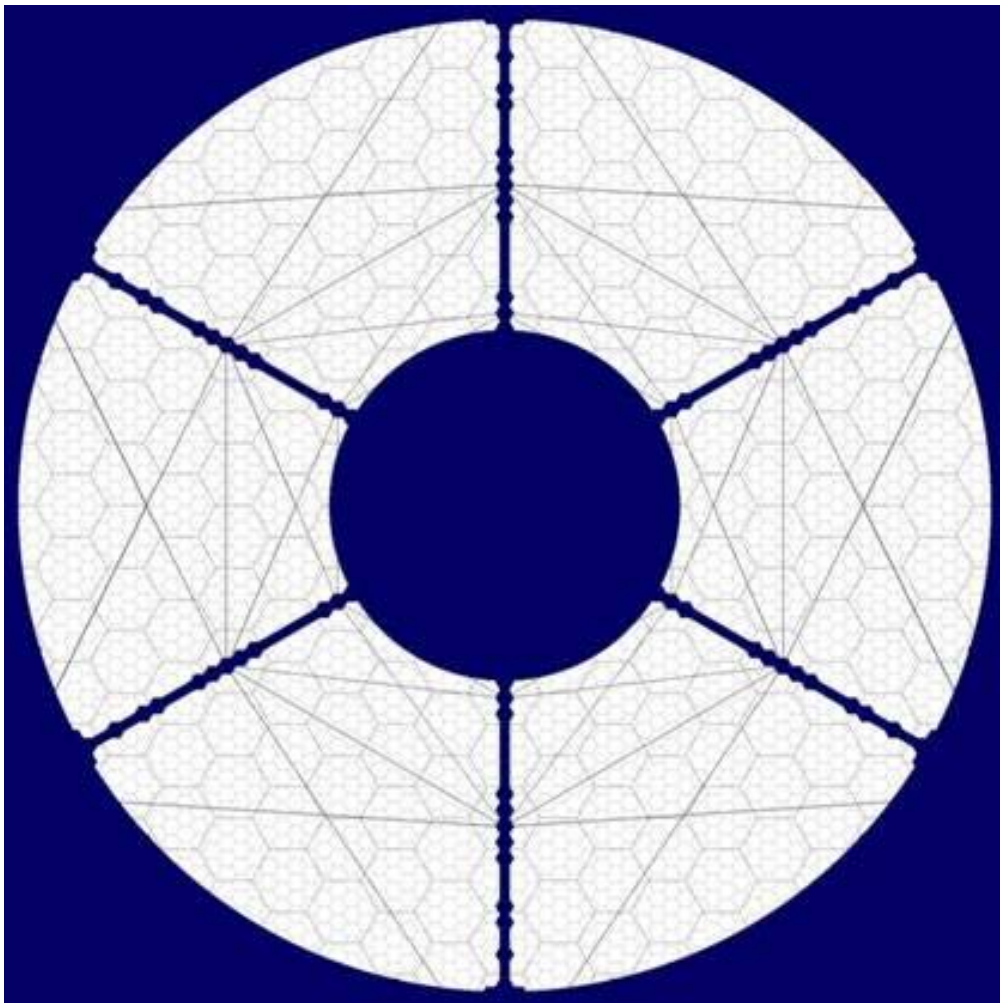

Figure 6-25. Pupil mask (emissivity budget). The pupil mask covers all obstructed areas except the inter-segment gaps and tensioning ropes.

The proposed segments maintenance infrastructure (see RD5) would allow the secondary mirror to be gold-coated within 43 days. In a science operation scenario whereby the telescope would have to be IR optimized over a significant span of time, one could reasonably assume that the mirrors M2 to M4 would receive temporary gold coatings. In the 43 days transition phases a variable reflectivity of the pupil would have to be tolerated. The telescope downtime would be limited to that required for the gold-coatings of M3 and M4 i.e. 5 to 7 calendar days.

Long-term durability data about the Gemini enhanced Ag coatings are not available at the time of writing of this report. Early performance results are however very promising, with a reported emissivity of less than 1.5% per reflective surface. Would such coatings be eventually selected, OWL emissivity would be as given in Table 6-8.

6.3.5 Sensitivity analysis

The sensitivity matrix (depointing and aberration coefficients for unit decenters) is given in Table 6-9. Field-dependent and field-independent terms are listed separately. Field-dependent terms are given at 1.5 arc minutes off-axis i.e. at the edge of the science field. Lateral decenters and tip-tilt introduce 3rd and 5th order coma (constant), and 3rd and 5th order astigmatism (linear in the filed of view). In addition, lateral decenters and tip-tilt may introduce a tilt of the image surface, i.e. a linear defocus.

The effect of corrector decenters (rigid body motion) about M4 vertex is given in Table 6-10. As expected, the effect of lateral decenters is identical to that of primary mirror decenters. The effect of tilt is much smaller.

Because of the short focal ratio of the primary mirror, M1, M2 and corrector piston are critical. Defocus will be best corrected by M2 for relatively large amplitudes and low time frequencies, fine correction being done with M5. M2 segments supports being identical to those of the primary mirror, they have the necessary range to compensate for up to 15 mm of despace. Excessive M5 refocus would require active deformation of M3 and M4 to compensate for the change in the prescription of field aberrations. Although theoretically possible, this is considered as a backup only, in case the required amplitude of M5 motion would exceed acceptable limits.

It should be noted that unit lateral decenters of M3 and M4 tend to compensate each other (coma terms), which is favorable since both mirrors will inherently move in the same direction under wind and gravitational loads.

It is expected that the internal metrology system, with a resolution of ~10 ppm, will allow centering all surfaces to within ~1 mm and ~2-3 arc seconds. Residuals will have to be compensated by active centering, with on-sky metrology.

OWL SENSITITVITY ANALYSIS — **ALL DATA ARE DIFFERENTIAL VALUE(DECENTERED) - VALUE(NOMINAL)**

Analysis file **OWL-1250-92518-100m-11sens.ZMX** — **Coordinates systems**

Units	dx, dy, dz	mm	About surface vertex	dx, dy, dz, da, db in surface ref. system, xy plane tangent to vertex
	da, db	arc seconds	About surface vertex	da = rotation about x; db = rotation about y
	dx_sky, dy_sky	arc secs		dz positive in the direction of ray propagation after surface
	Zernike	Coeff., microns (circular Zernikes)		Zernikes: x, y in-pupil coordinates
	WFE RMS	microns		*FIELD TERMS ARE GIVEN AT 1.5 ARC MINUTE OFF-AXIS ALONG +Y (*)*

Mirror	Decenter		Depointing		WFE RMS		Zernike coefficients												
							Field-independent							Field-dependent					
										Coma 3		Coma 5			Ast 3		Ast 5		
	Type	Ampl.	dx_sky	dy_sky	On-axis	Off-axis	Focus	Spher 3	Spher 5	x	y	x	y	Focus	x	y	x	y	
1	dx	1.000	1.652	0.000	2.831	2.830	0.000	0.000	0.000	2.699	0.000	0.009	0.000	0.000	0.000	-0.018	0.000	-0.001	
1	dy	1.000	0.000	1.652	2.831	2.827	0.000	0.000	0.000	0.000	2.699	0.000	0.009	0.005	0.018	0.000	0.001	0.000	
1	dz	1.000	0.000	0.000	23.095	23.095	40.002	0.001	0.000	0.000	0.000	0.000	0.000	0.000	0.000	0.000	0.000	0.000	
1	da	1.000	0.000	2.002	3.433	3.428	0.000	0.000	0.000	0.000	3.271	0.000	0.011	0.026	0.023	0.000	0.001	0.000	
1	db	1.000	-2.002	0.000	3.433	3.431	0.000	0.000	0.000	-3.271	0.000	-0.011	0.000	0.001	-0.001	0.021	0.000	0.001	
2	dx	1.000	0.000	0.000	0.000	0.000	0.000	0.000	0.000	0.000	0.000	0.000	0.000	0.000	0.000	0.000	0.000	0.000	
2	dy	1.000	0.000	0.000	0.000	0.000	0.000	0.000	0.000	0.000	0.000	0.000	0.000	0.000	0.000	0.000	0.000	0.000	
2	dz	1.000	0.000	0.000	46.192	46.192	80.007	0.003	0.000	0.000	0.000	0.000	0.000	0.000	0.000	0.000	0.000	0.000	
2	da	1.000	0.000	-0.520	4.349	4.348	0.000	0.000	0.000	0.000	-4.122	0.000	-0.013	-0.006	-0.026	0.000	0.000	0.000	
2	db	1.000	0.520	0.000	4.349	4.349	0.000	0.000	0.000	4.122	0.000	0.013	0.000	0.000	-0.001	-0.027	0.000	0.000	
3	dx	1.000	-1.243	0.000	33.029	33.032	-0.013	0.002	0.000	32.088	0.000	0.803	0.000	0.000	-0.012	-0.002	0.002	-0.046	
3	dy	1.000	0.000	-1.243	33.029	33.038	-0.013	0.002	0.000	0.000	32.088	0.000	0.803	0.014	0.014	0.000	0.044	0.000	
3	dz	1.000	0.000	0.000	22.945	22.946	39.740	-0.408	0.265	0.000	0.000	0.000	0.000	0.000	0.000	0.000	0.000	0.000	
3	da	1.000	0.000	-0.113	3.516	3.516	0.000	0.000	0.000	0.000	3.358	0.000	0.033	-0.044	0.012	0.000	-0.001	0.000	
3	db	1.000	0.113	0.000	3.516	3.516	0.000	0.000	0.000	-3.358	0.000	-0.033	0.000	-0.001	0.000	0.011	0.000	-0.001	
4	dx	1.000	-1.625	0.000	38.625	38.628	-0.007	0.002	0.001	-37.455	0.000	-0.866	0.000	0.000	-0.011	0.093	0.002	0.075	
4	dy	1.000	0.000	-1.625	38.625	38.633	-0.007	0.002	0.001	0.000	-37.455	0.000	-0.866	-0.301	-0.083	0.000	-0.077	0.000	
4	dz	1.000	0.000	0.000	11.966	11.970	20.719	-0.660	0.255	0.000	0.000	0.000	0.000	0.001	-0.001	0.000	0.000	0.000	
4	da	1.000	0.000	0.157	0.276	0.277	0.000	0.000	0.000	0.000	0.282	0.000	0.021	0.098	0.017	0.000	0.006	0.000	
4	db	1.000	-0.157	0.000	0.276	0.276	0.000	0.000	0.000	-0.282	0.000	-0.021	0.000	0.000	0.000	0.016	0.000	0.006	
5	dx	1.000	1.559	0.000	2.765	2.766	0.006	0.000	0.000	2.668	0.000	0.054	0.000	0.000	0.001	-0.073	0.000	-0.028	
5	dy	1.000	0.000	1.559	2.765	2.780	0.006	0.000	0.000	0.000	2.668	0.000	0.054	0.489	0.072	0.000	0.028	0.000	
5	dz	1.000	0.000	0.000	13.108	13.109	22.702	-0.249	-0.009	0.000	0.000	0.000	0.000	0.002	-0.002	0.000	0.000	0.000	
5	da	1.000	0.000	0.064	0.053	0.056	0.000	0.000	0.000	0.000	0.049	0.000	-0.001	0.119	-0.010	0.000	0.000	0.000	
5	db	1.000	-0.064	0.000	0.053	0.053	0.000	0.000	0.000	-0.049	0.000	0.001	0.000	0.000	0.000	-0.010	0.000	0.000	
6	dx	1.000	0.000	0.000	0.000	0.000	0.000	0.000	0.000	0.000	0.000	0.000	0.000	0.000	0.000	0.000	0.000	0.000	
6	dy	1.000	0.000	0.000	0.000	0.000	0.000	0.000	0.000	0.000	0.000	0.000	0.000	0.000	0.000	0.000	0.000	0.000	
6	dz	1.000	0.000	0.000	1.988	1.988	3.443	0.002	0.000	0.000	0.000	0.000	0.000	0.001	-0.001	0.000	0.000	0.000	
6	da	1.000	0.000	-0.046	0.000	0.019	0.000	0.000	0.000	0.000	0.000	0.000	0.000	-0.117	0.000	0.000	0.000	0.000	
6	db	1.000	0.046	0.000	0.000	0.000	0.000	0.000	0.000	0.000	0.000	0.000	0.000	0.000	0.000	0.000	0.000	0.000	
TOTAL			***-1.202***	***1.887***	***119.282***	***119.282***	***206.586***	***-1.303***	***0.513***	***-2.839***	***2.839***	***-0.052***	***0.052***	***0.288***	***0.009***	***0.012***	***0.006***	***0.006***	

Table 6-9. Baseline design, sensitivity matrix.

OWL SENSITITVITY ANALYSIS

ALL DATA ARE DIFFERENTIAL VALUE(DECENTERED) - VALUE(NOMINAL)

Analysis file **OWL-1250-92518-100m-11sens.ZMX**

Coordinates systems

Units

dx, dy, dz	mm	About M4 vertex
da, db	arc seconds	About M4 vertex
dx_sky, dy_sky	arc secs	
Zernike	Coeff., microns (circular Zernikes)	
WFE RMS	microns	

dx, dy, dz, da, db in surface ref. system, xy plane tangent to vertex
da = rotation about x; db = rotation about y
dz positive in the direction of ray propagation after surface
Zernikes: x, y in-pupil coordinates
FIELD TERMS ARE GIVEN AT 1.5 ARC MINUTE OFF-AXIS ALONG +Y (*)

Mirror	Decenter		Depointing		WFE RMS		Zernike coefficients											
							Field-independent							Field-dependent				
	Type	Ampl.	dx_sky	dy_sky	On-axis	Off-axis	Focus	Spher 3	Spher 5	Coma 3		Coma 5		Focus	Ast 3		Ast 5	
										x	y	x	y		x	y	x	y
Corrector	dx	1.000	-1.652	0.000	2.832	2.830	0.000	0.000	0.000	-2.699	0.000	-0.009	0.000	0.000	0.000	0.018	0.000	0.001
Corrector	dy	1.000	0.000	-1.652	2.832	2.828	0.000	0.000	0.000	0.000	-2.699	0.000	-0.009	-0.005	-0.018	0.000	-0.001	0.000
Corrector	dz	1.000	0.000	0.000	23.095	23.095	40.002	0.001	0.000	0.000	0.000	0.000	0.000	0.000	0.000	0.000	0.000	0.000
Corrector	da	1.000	0.000	0.034	1.787	1.787	0.000	0.000	0.000	0.000	1.691	0.000	0.005	0.000	0.011	0.000	0.000	0.000
Corrector	db	1.000	-0.034	0.000	1.787	1.787	0.000	0.000	0.000	-1.691	0.000	-0.005	0.000	0.000	0.000	0.011	0.000	0.000
TOTAL			***-1.686***	***-1.618***	***23.150***	***23.150***	***40.002***	***0.001***	***0.000***	***-4.390***	***-1.007***	***-0.014***	***-0.004***	***-0.004***	***-0.007***	***0.029***	***-0.001***	***0.001***

Table 6-10. Baseline design, sensitivity matrix, corrector decenters (rigid body).

6.3.6 Imaging of turbulent layers

Aberrations (including defocus) in the conjugation between layers and their presumably conjugated mirrors introduce errors in the adaptive correction. An aberrated image of a given layer implies that rays emanating from different sky sources and intersecting in the physical turbulent layer will impact the conjugate (adaptive mirror) at different locations. For the sake of simplicity, let us consider a single, infinitely thin layer and its aberrated conjugate (Figure 6-26). Assuming that light ray number 1 emanates from the reference source, and assuming a perfect adaptive correction for this ray (e.g. adaptive mirror supported by an infinite number of supports), we can easily calculate the adaptive correction error on rays emanating from the science sources (rays 2 or 3 in Figure 6-26. Let r_0 be the atmospheric coherence length in the turbulent layer, and r'_0 the equivalent dimension as projected onto the adaptive mirror. Lert dh' be the transverse geometrical aberration of the layer image, the reference ray (dh'=0) being that emanating from the reference source, which will see a perfect correction. Assuming constant magnification, r'_0 and dh' are proportional to equivalent quantities r_0 and dh transposed back to the object space. A Kolmogorov model being perfectly adequate over such dimensions, the wavefront mean square phase distortion σ^2 between the reference and the science target will be given by the structure function:

$$\sigma^2 = 6.88\ (dh / r0)^{5/3} \qquad \textit{Eq. 6-1.}$$

In general dh will be field-dependent; if the field of view θ is negligible (Single-Conjugate Adaptive Optics or SCAO), dh=0 and the adaptive correction will not be impaired by aberrations in the layer conjugation. This is no longer the case with Multi-Conjugate Adaptive Optics (MCAO) or Ground-Layer Adaptive Optics (GLAO). Statistically, however, the mean square correction error should decrease with the number of references and converge towards σ^2/N, where N is the number of reference sources, assumed to be uniformly distributed.

It should be noted that Eq. 6-1 gives the mean square aberration of the rays intersecting in A' only; the overall error of the correction at a given field position results from the integral of Eq. 6-1 over the conjugate area.

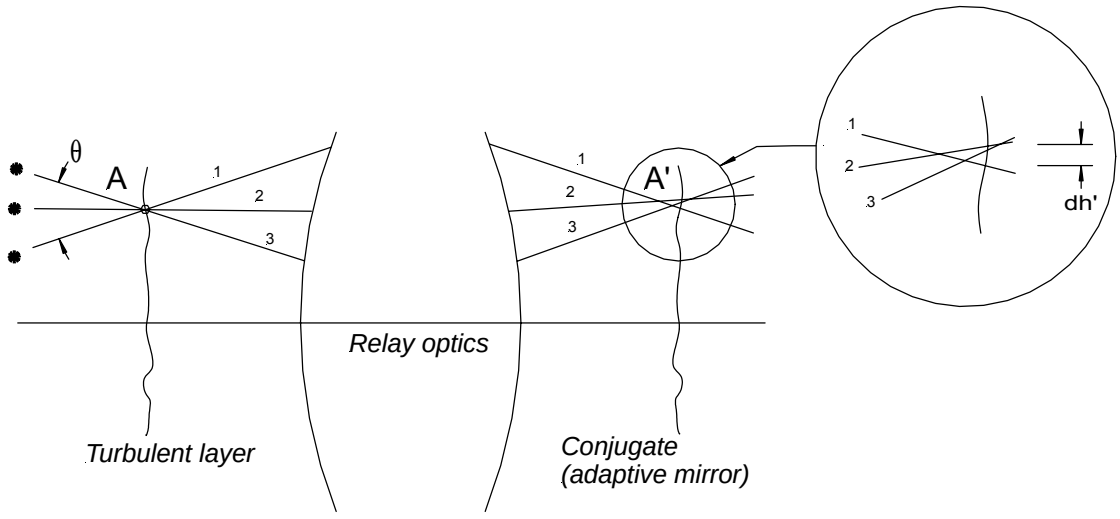

Figure 6-26. Aberrated layer image.

The case of a defocused image of a layer is the simplest to evaluate. Let ε be the despace of the conjugate with respect to the actual layer, in the object space, and θ be the field separation between the science target and the reference. With $dh = \varepsilon\,\theta$, we find that a 1 km despace, a 1 arc minute separation between the reference and science target and an atmospheric coherence length of 1 meter (good seeing, K band) leads to a ~$\lambda/7$ RMS correction error. Figure 6-27

shows the RMS correction error (wavefront, λ units) for a 1 km despace, as a function of r_0 and for three different angular separations between the reference and the science target.

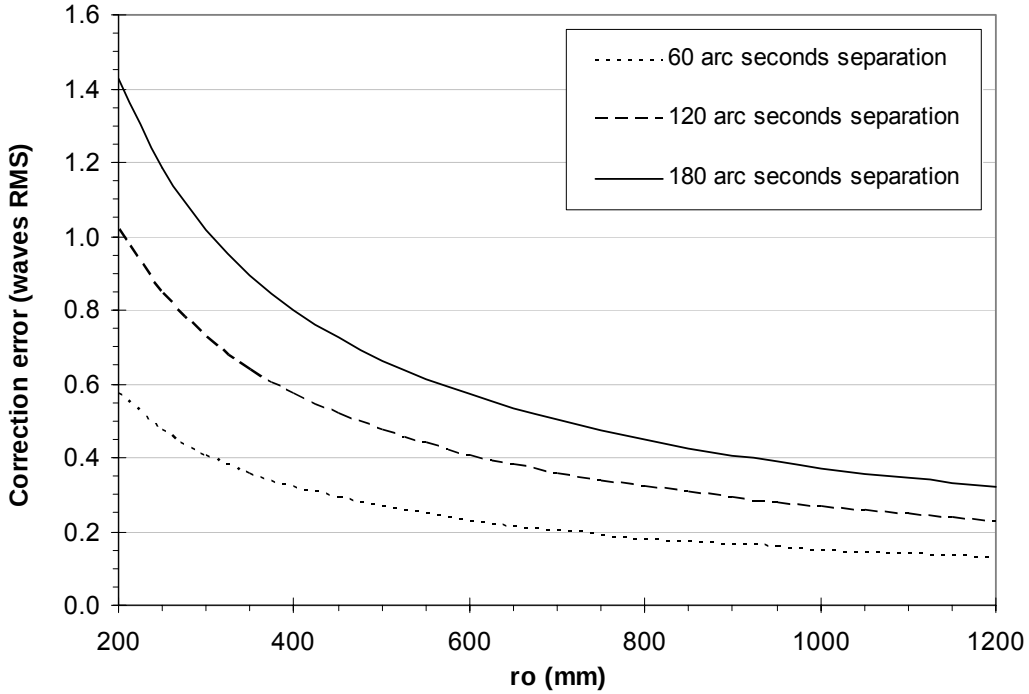

Figure 6-27. Adaptive correction error (wavefront RMS) for 1 km conjugate defocus

We shall now evaluate the impact of OWL aberrations of the pupil re-imaging on M6, including the effect of M6 tilt. Figure 6-28, Figure 6-29, and Figure 6-30 show the spot diagrams of the imaging of the entrance pupil onto M6, along the tilted axis of M6, with 1, 3 and 6 arc minutes field diameter. The effect of the mirror tilt is evident; the assymmety between "lower" and "upper" edges is due to an overall defocus, M6 vertex not being exactly coincident with the vertex of the exit pupil. Spot coordinates refer to the chief ray of the conjugation entrance-exit pupils i.e. the reference ray corresponds to an on-axis science target. The maximum geometrical spot radius is 5.8mm, 18mm, and 38mm, with 30, 90 and 180 arc seconds off-axis reference sources, respectively. Assuming an atmospheric coherence length corresponding to ~25 mm on M6[48], the corresponding dh/r_0 at the upper edge of the mirror of 0.23, 0.72 and 1.50, respectively. The adaptive correction errors are ~λ/8, λ/3 and λ/1.7 wavefront RMS for the corresponding rays. These errors are the maxima over the pupil area; the overall accuracy of the adaptive correction will result from the integrated effect over the entire mirror area –most of which is providing a substantially better conjugation. In addition, large corrected fields require several guide stars and as previously mentioned, the error should statistically decrease as $1/\sqrt{N}$, where N is the number of reference sources.

The current baseline design has not been constrained to having M6 vertex optimally located for ground layer and multi-conjugative adaptive optics. Preliminary checks indicate that a re-optimization ought to be possible without significant changes in the design.

[48] i.e. corresponding to the expected inter-actuator separation.

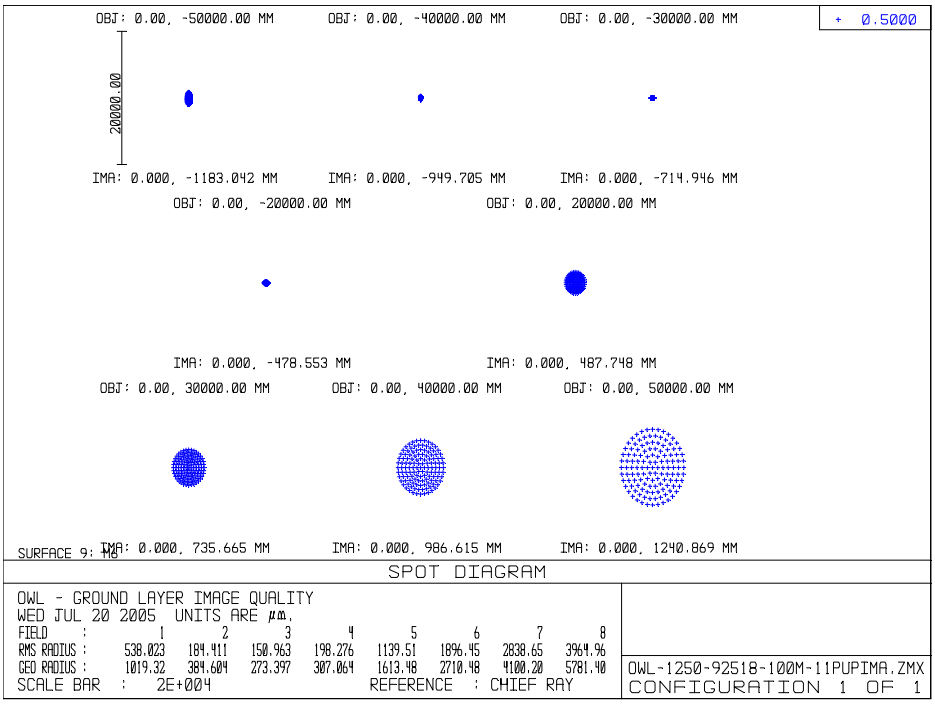

Figure 6-28. Image quality of the pupil conjugation; field of view 1 arc minute diameter.

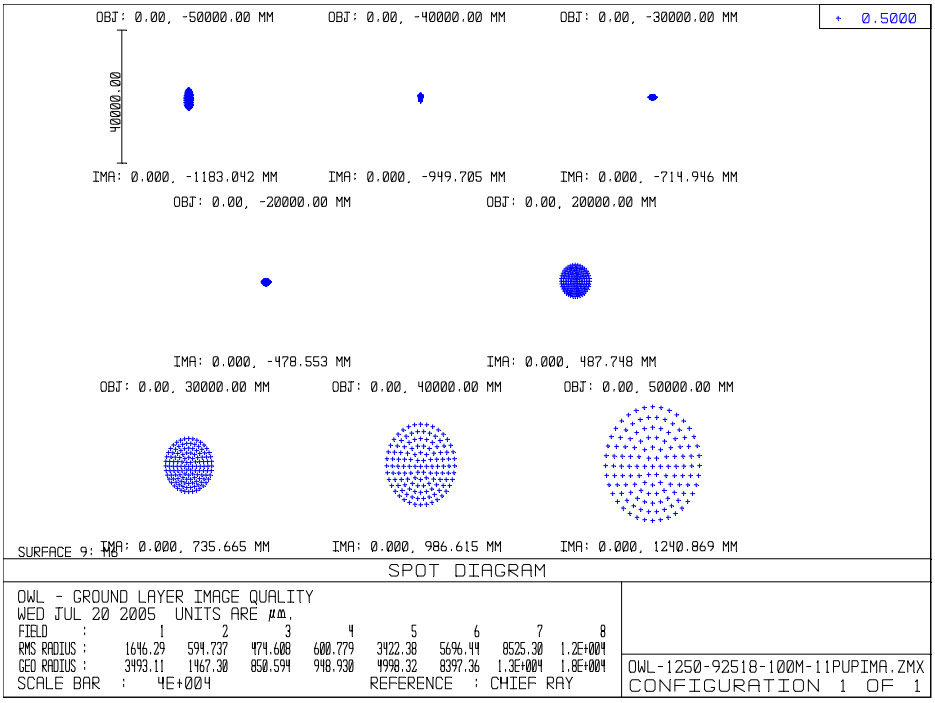

Figure 6-29. Image quality of the pupil conjugation; field of view 3 arc minutes diameter.

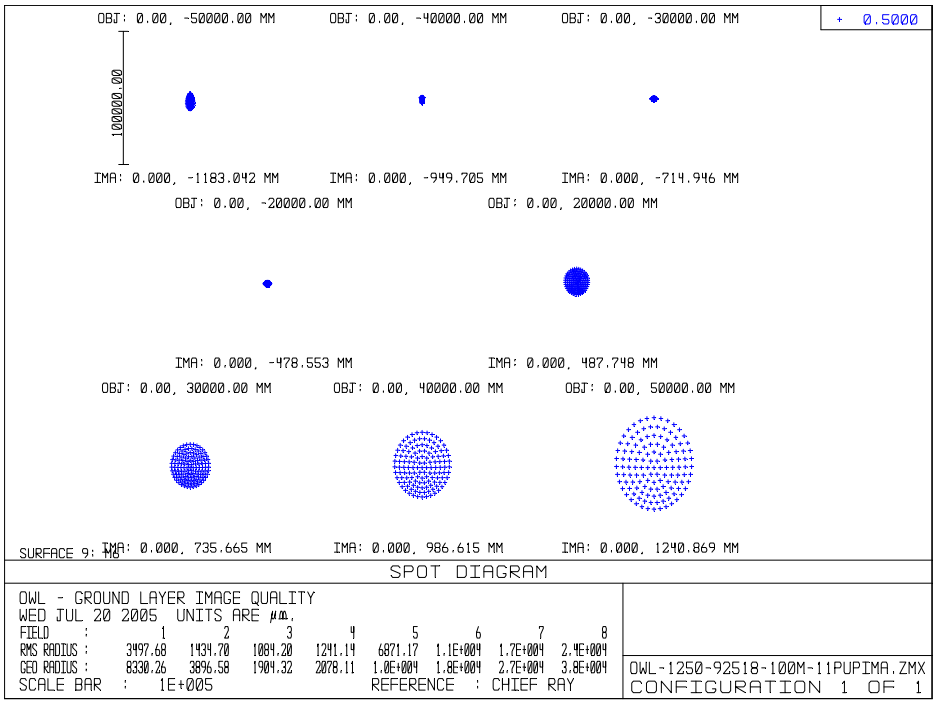

Figure 6-30. Image quality of the pupil conjugation; field of view 6 arc minutes diameter.

6.3.7 Imaging of Laser Guide Stars

Geometrical imaging properties for Laser Guide Stars (LGS) have been checked in full details with a previous iteration of the optical design (see RD1). At the time of writing of this document, only a brief analysis has been done with the baseline design. The main aberration is evidently defocus and, and as shown in RD1 it is proportional to D^2 but does not depend on the optical prescription. Higher order terms do not seem to be strongly design-dependent, and even after refocus, image quality is very poor. Figure 6-31 shows the spot diagram for a point-like LGS at 90 km distance, on-axis and 3 arc minutes off-axis, after refocus (the LGS image is 5879.7 mm behind the nominal focus). Figure 6-32 shows the wavefront 3 arc minutes off-axis. The off-axis image quality is about 1.5 arc seconds RMS.

As shown in RD1, this implies that not only tip-tilt, but also defocus, third and fifth order terms would have to be tracked on Natural Guide Stars (NGS), and that the LGS AO wavefront sensors would have to incorporate active surfaces for the compensation of low order terms in order to reduce the noise of measurement of higher order terms. Sampling on the NGS reference would be comparable to sampling of the tip-tilt on an 8-10 m class telescope. It should be noted that the pupil diameter being much larger then the outer scale of turbulence, low order atmospheric terms should, in principle, remain conveniently small.

Practical implementation of the above concept would certainly imply complex relay optics. Novel approaches towards wavefront sensing on Laser Guide Stars might eventually provide simpler solutions. The matter is being addressed within the framework of the ELT Design Study (see also section 8.4 and following).

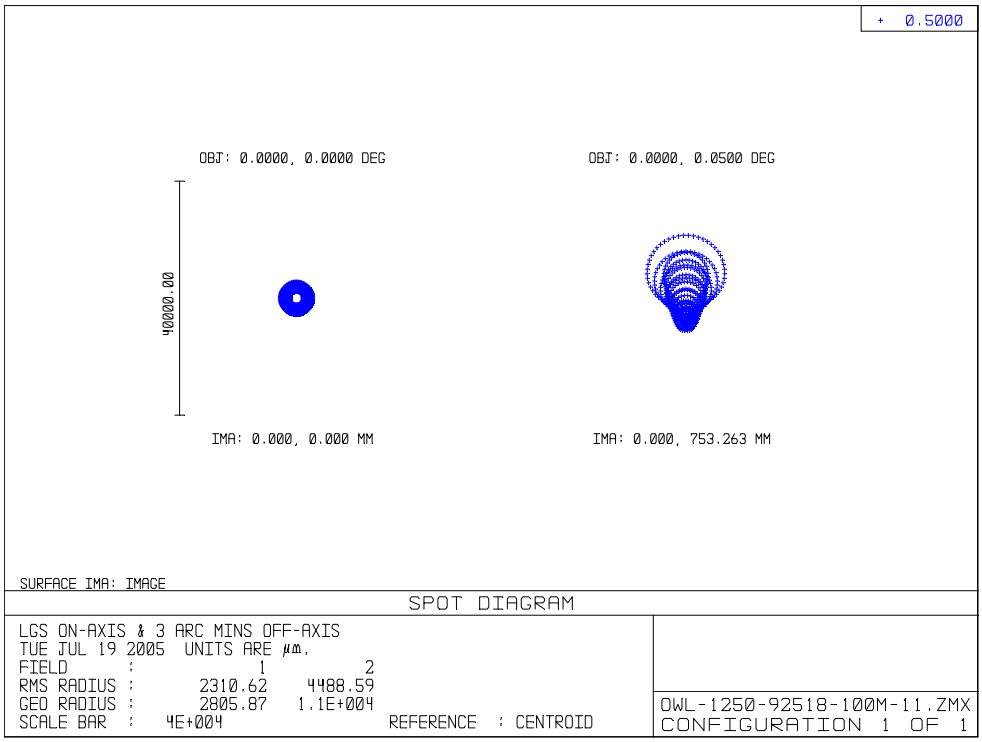

Figure 6-31. Spot diagrams, LGS at 90 km on-axis and 3 arc minutes off-axis.

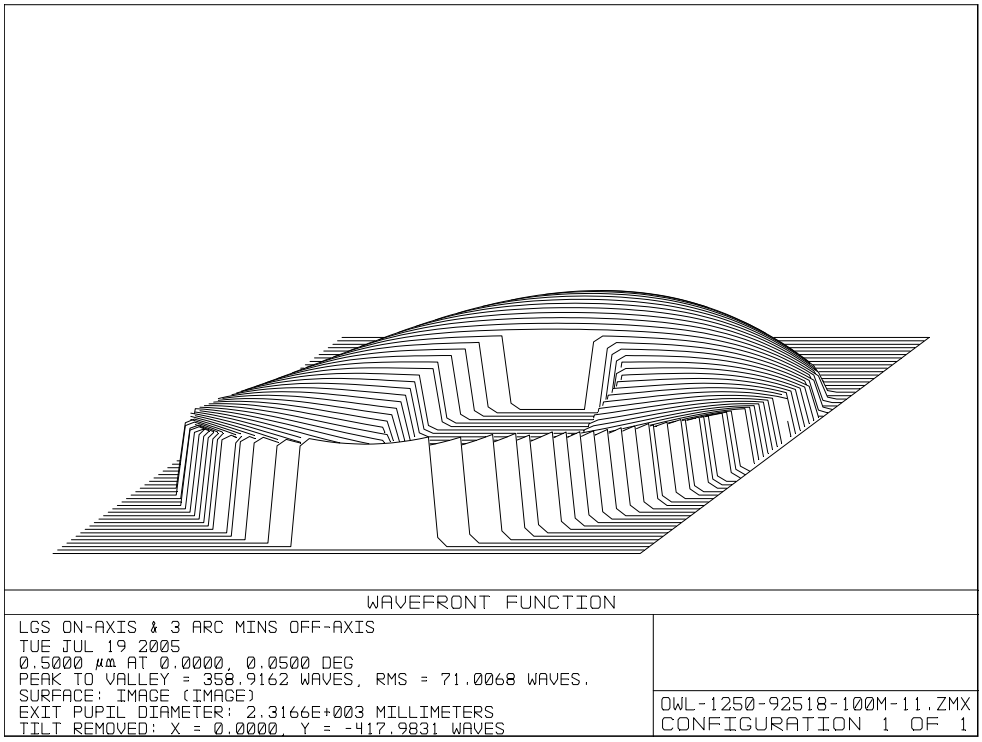

Figure 6-32. Wavefront map, LGS at 90 km, 3 arc minutes off-axis.

6.4 Diffraction and high contrast imaging

This section provides a brief description of diffraction effects associated to OWL segmentation and pupil shape. As a related topic, high contrast imaging and coronagraphy are addressed in RD22.

6.4.1 Diffraction

6.4.1.1 Structure of PSF in diffraction-limited regime

The properties of the PSF produced by the OWL pupil in diffraction limit regime is necessary for an adequate interpretation of astronomical data. The PSF possesses unique features particular to a segmented telescope with a large numbers of segments.

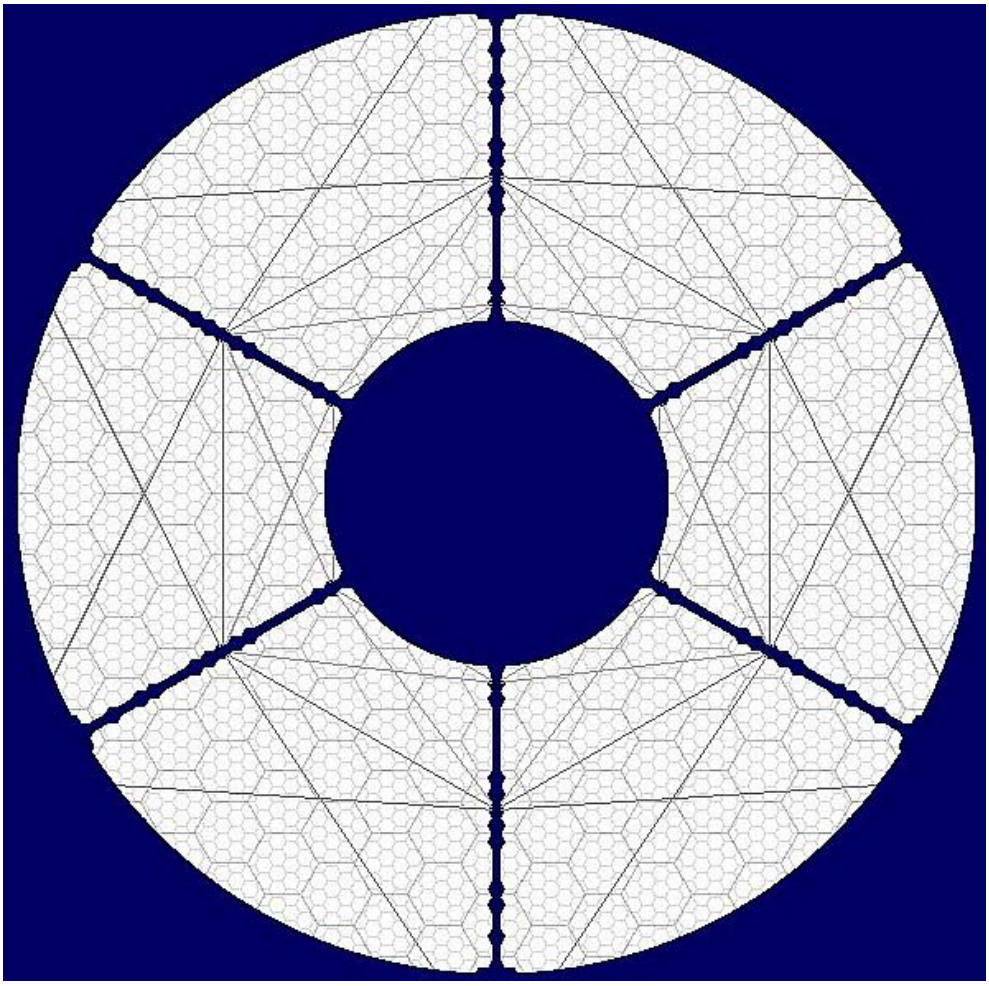

Figure 6-33. Model of the pupil for studying diffraction effects

6.4.1.1.1 Pupil modelling elements

The following pupil elements were included into the model:

1. A Circular mask with an inner diameter 35m and an outer diameter 97m. These dimensions are set to mask the irregular outer contour of the combined primary and secondary mirrors.

2. The obscuration by structural beams (spiders), which have a 1-m width, projected onto the entrance pupil
3. “Missing” segments under the structural beams. These correspond to the location of beams connecting the upper structures to those behind the primary mirror.
4. The ropes, with 50 to 70 mm width, projected onto the entrance pupil.
5. Primary mirror gaps: the segments are all identical, with a flat-to-flat dimension of 1.6m. Paving the primary mirror sphere with all identical segments implies irregular inter-segment gaps. The optimal segments distribution leads to gaps of 4mm to 16mm, with an average of 10mm. Taking into account 2 mm bevels at the segments edges, the averaged gap size used in simulations is 14 mm. To accommodate for gap size smaller than resolution of the numerical grid, the gray pixel method is used.
6. Secondary mirror gaps: the flat secondary mirror has constant gaps of 3.75mm. Taking 2mm bevels into account, the gaps of the secondary mirror are modelled with a width of 7.75mm. The two mirrors are superimposed using geometrical projection. The magnification factor for the secondary mirror is 3.8975.

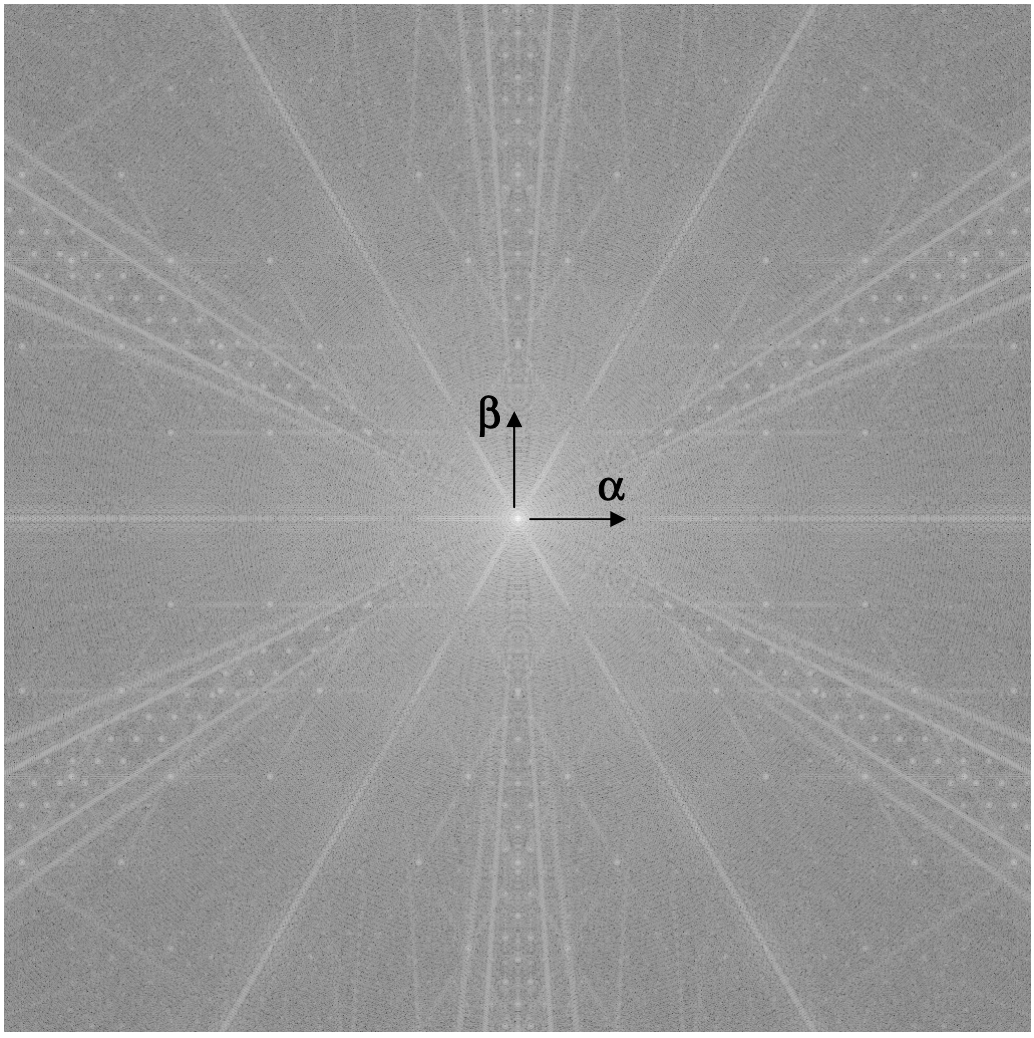

Figure 6-34 PSF from the pupil presented above. The field of view is 1 arc second diameter, wavelength is 650 nm. Here and further: logarithmic scale.

The PSF obtained by Fourier transform of the pupil is shown in Figure 6-34. Individual contributions by the pupil elements can be distinguished. Note that the diffraction pattern reveals the geometry of the aperture. Each of the features possesses a $\pi/3$ symmetry. This symmetry is preserved in the diffraction pattern, which makes the diffraction elements

separable from other effects (e.g. adaptive optics residuals). In order to describe this symmetry it is helpful to introduce the term *direction of diffraction*. There are two major directions of diffraction: α-direction is along the Ox plus 5 obtained by the rotation Ox by $\pi/3$; β – direction is the same for Oy.

In the following we shortly describe each of pupil effects separately.

6.4.1.1.2 Secondary mirror support

The spikes (diffraction lines) repeat the geometry of the spiders, rotated by 90º. The diffraction lines are periodic (Figure 6-35). Their thickness (a_1) and their period (a_2) are defined by the dimensions (b_1, b_2) of the spiders:

$$a_1 = \frac{\lambda}{b_1} = 0.206\frac{0.65\ \mu m}{66\ m} = 0.001 arc\sec$$
$$a_2 = \frac{\lambda}{b_2} = 0.206\frac{0.65\ \mu m}{1\ m} = 0.13 arc\sec$$

Eq. 6-2.

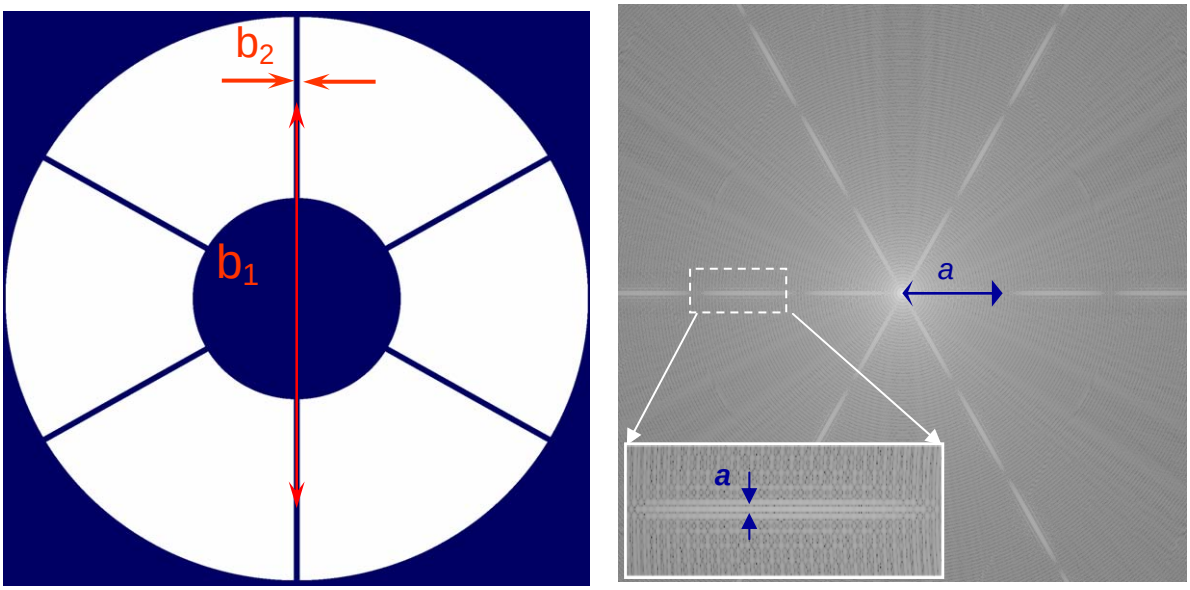

Figure 6-35 Diffraction by the "spider". PSF box size 0.72"

6.4.1.1.3 "Missing" segments

This element produces the diffraction pattern consisting of the short lines connecting the points of the high – order diffraction peaks. The diffraction is the strongest in β-direction (Figure 6-36).

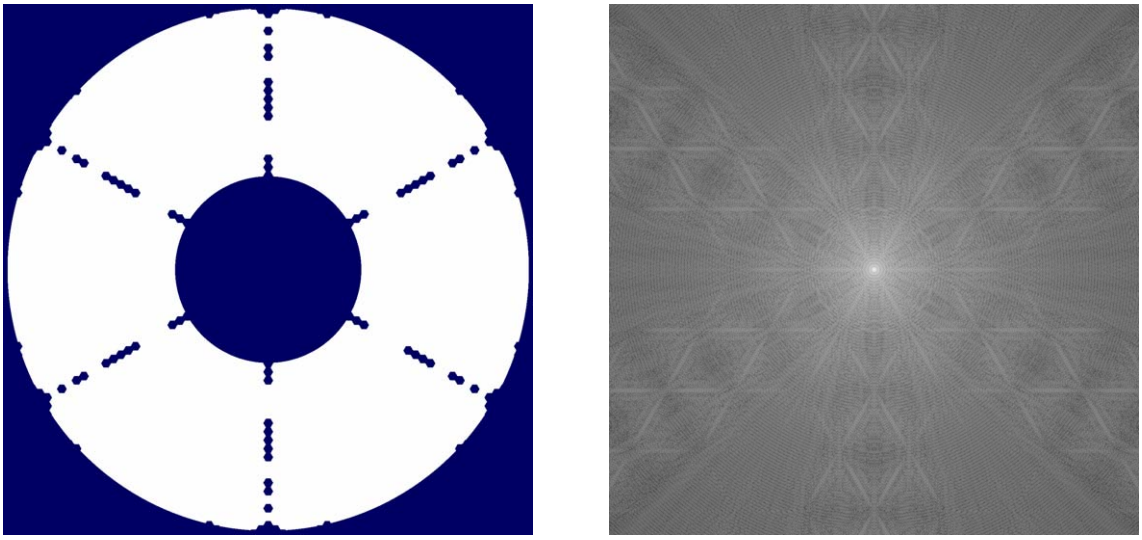

Figure 6-36 Diffraction by "missing" segments. PSF box size 0.72"

6.4.1.1.4 Ropes

The radial rays observed in the PSF are produced by the ropes. This pattern has also $\pi/3$ symmetry and most of the diffraction is within ±6° about β-direction (Figure 6-37).

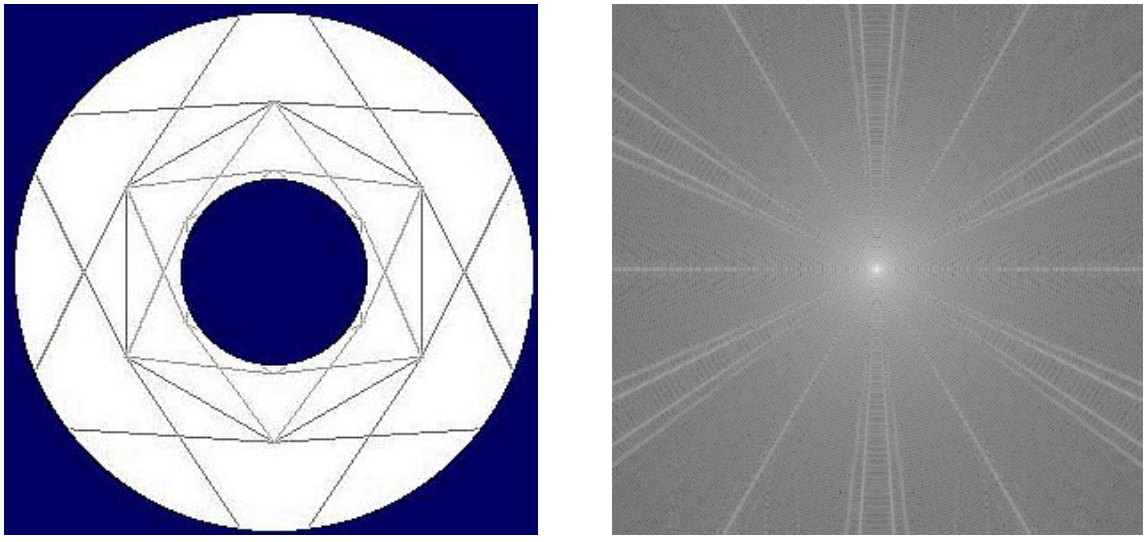

Figure 6-37 Diffraction by the ropes. PSF box size 0.72"

6.4.1.1.5 Diffraction by the gaps

Mechanism of diffraction pattern formation

Inter-segment gaps make the segmented mirror act as a diffraction grating. By analogy with diffraction gratings the residual PSF is the product of two factors: a "grid factor" (GF) which is the Fourier transform of the segmentation grid, usually a periodic function of sharp peaks, and the point spread function P_s of an individual segment [83], [84]. Without gaps the peaks of the

GF fall onto the zeros of the single segment PSF and in the product only central peak is observed (Figure 6-38).

The introduction of gaps enlarges P_s while it leaves the grid function GF unchanged. As a result higher order peaks appear. Relative peak intensity is the value of P_s at the locations of GF peaks.

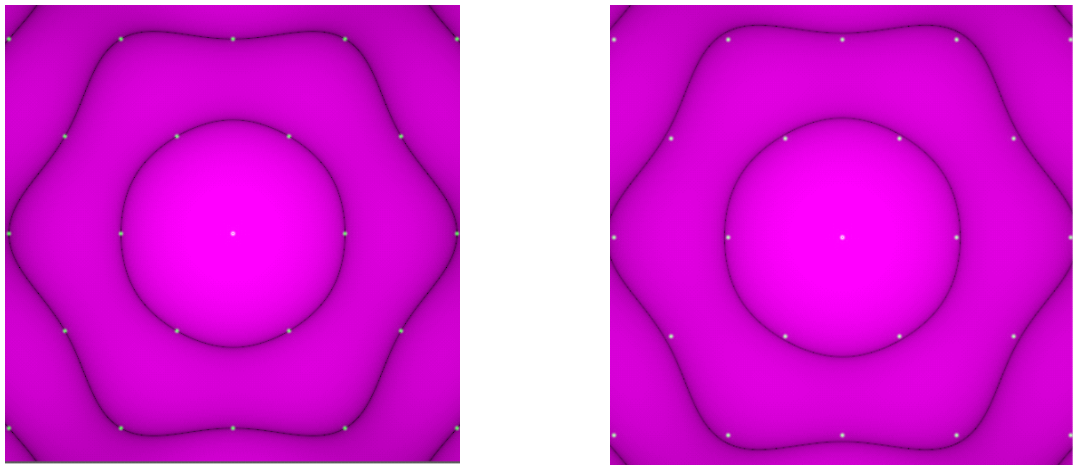

Figure 6-38. Mechanism of the formation of diffraction peaks (gaps): the grid factor (dots) is multiplied by the segment PSF. Left: without gaps; except for the central one all peaks of the grid factor fall into zeros of the segment PSF_s. Right: with gaps; peaks no longer coincide with PSF_S zeros.

The position of the peaks is defined by the segments center to center separation and the wavelength. The intensity of the peaks only by the gap size related to the segment size.

The well understood principle of diffraction peaks formation allows their formal classification. This classification allows to define the intensity of the peak knowing its angular distance from the central point. For example, the 6 brightest peaks closest to the center (in the classification they are referred to as A_1 peaks) are located at a distance equal to $2\lambda/(\sqrt{3}d)$ and have an intensity relative to the central point of $0.68g/d$ (g – gap size, d – segment size). This gives $5.2\cdot10^{-5}$ for the primary mirror of OWL (the result obtained in simulation is $4.5\cdot10^{-5}$).

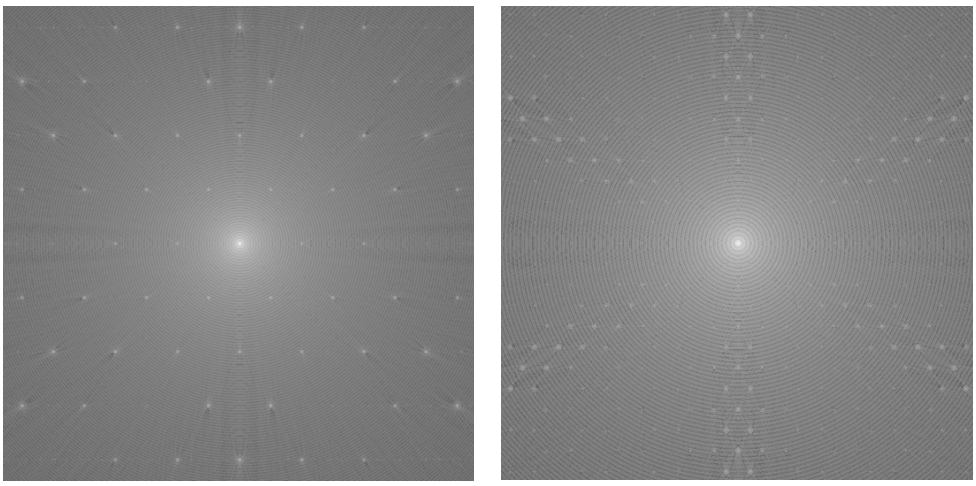

Figure 6-39 Diffraction by intersegments gaps of the primary (left) and of the secondary mirrors (right). Box size 0.72 arc secons.

Gaps on primary and secondary mirrors

Although gaps on the primary mirror vary from 4 to 16mm, all segments contribute equally to the diffraction pattern and diffraction peaks appear as with regular gaps (averaged size). The simulations performed with varying gap size have confirmed this and therefore the analysis was done with the averaged gap size. Gaps on the secondary mirror are all identical.

Because of the scaling factor, segments on the secondary mirror are ~4 times larger, and therefore the peaks are 4 times closer to the central peak, as shown in Figure 6-39.

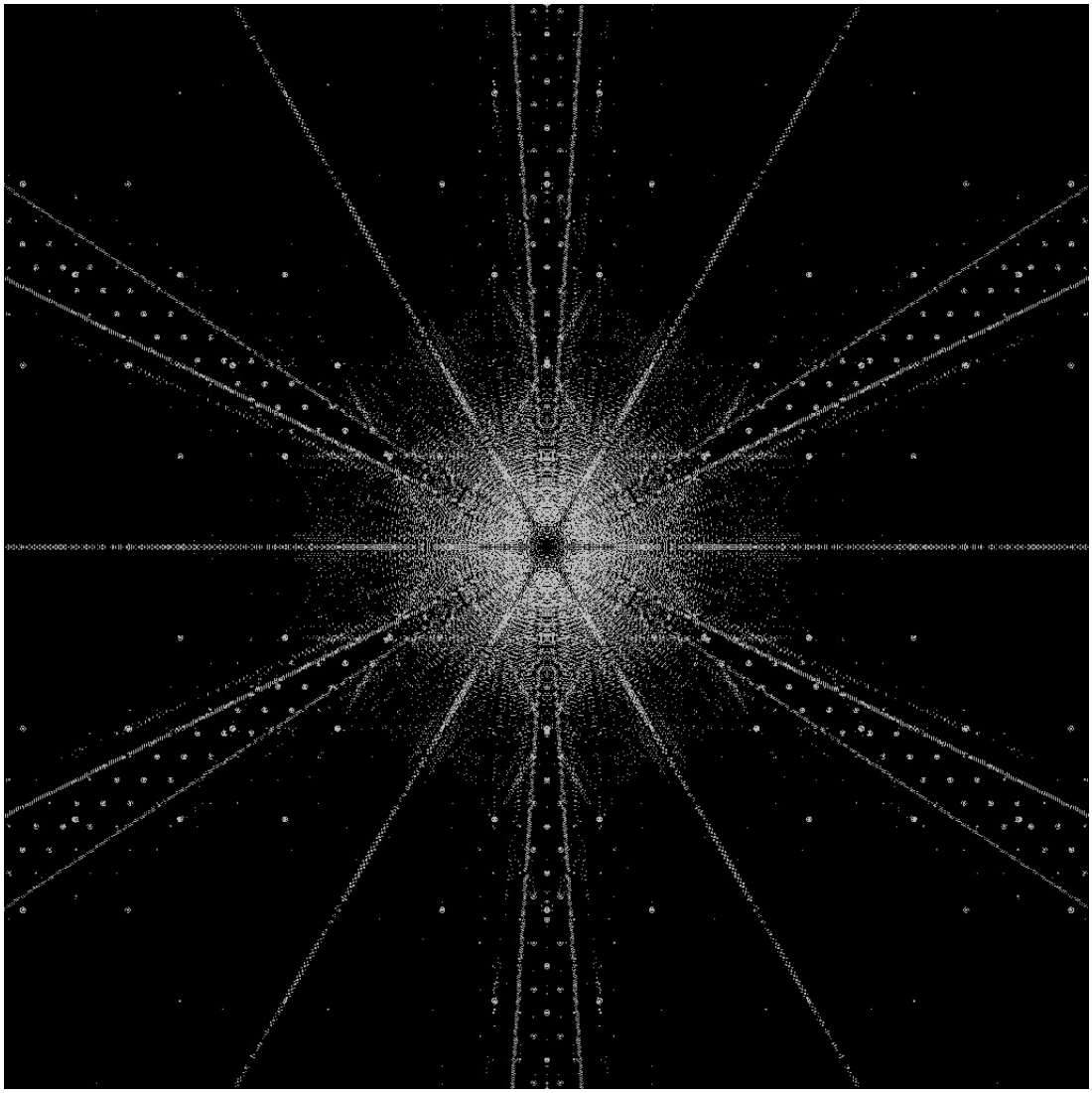

Figure 6-40 Intensity slice representation of OWL PSF between 10^{-5} and 10^{-7}. Most diffraction artefacts are apparent.

6.4.1.2 PSF representation: intensity slices

So far while describing the PSF we concentrated only on its geometrical properties, without regard to relative intensity. One can do the detailed analysis of each diffraction element with intensity measurement at each point, as it was done for instance for gaps [84]. Here, for a more representative description we show the PSF at different intensity intervals. Figure 6-40 shows that most of the effect is in the range 10^{-5} and 10^{-7}.

6.4.1.3 Effects of phasing errors on the PSF

6.4.1.3.1 Diffraction associated to piston and tip-tilt

The effect of the piston and tip-tilt on the PSF has been studied in detail according to the generalized formalism, i.e. through the representation using grid factor (GF) and PSF of the individual piston (P_s). Here we summarize the conclusion of this study.

Piston errors

The random piston errors cause a loss of intensity in the central peak and produce speckles. The speckle distribution corresponds to the distribution of the piston errors. The ensemble averaged speckled field for the given wavefront rms is $PSF_s \cdot [1-\exp(-rms^2)]/N$, where *rms* is the phase error (in radians) and *N* is the number of segments. Therefore, the outline of the speckled field repeats the shape of P_s but with reduced amplitude. The speckles are concentrated in the angular intervals $[0.25\lambda/d \div 1.2\lambda/d]$, $[1.2\lambda/d \div 2.2\lambda/d]$,… . The averaged width of each individual speckle has the size of the Airy disk from the whole mirror. The number of speckle in the first interval is of the order of the number of segments and their averaged intensity falls as N^{-1}.

Tip-tilt errors

A segmented aperture with random tip-tilt errors behaves as a randomly blazed 2D diffraction grating in that the loss of intensity in the central peak is accompanied by the appearance of a regular structure of diffraction peaks and a speckled halo. The position and relative intensity of the peaks is independent of the number of segments, while the averaged speckle intensity falls as N^{-1}. In weakly segmented mirrors (few tens of segments) the regular pattern is lost in speckles, but for highly segmented ones (few hundreds of segments) the regular pattern dominates. The outline of the speckled field is a modified PSF P_s, whose FWHM proportional to the tip-tilt error wavefront *rms*. The position of the diffraction peaks is given by the grid factor, i.e. is defined by segments center to center separation, wavelength and hexagonal geometry. For any value of the wave front *rms* the brightest peaks are the ones closest to the center six peaks (in the classification A_1 peaks) at $2\lambda/(\sqrt{3}d)$, that is 0.097" for d=1.6m and λ=0.65μm. For tip-tilt $rms=\lambda/8$ they have relative intensity $6 \cdot 10^{-3}$. For the small $rms < \lambda/15$ the intensity of A_1 peaks can be estimated as $0.01 \cdot rms^4$ (rms in radians). The position and intensity of all possible peaks can be also found using the classification mentioned above.

6.4.1.3.2 Intensity slice representation (FoV=1", λ=650nm)

Assuming random errors limited by the noise of the control system (actuators, sensors), the residual segmentation piston and tip-tilt would have a statistics close to a Gaussian distribution. The simulated PSF produced by random piston and tip-tilt errors are shown in Figure 6-41. Two representative cases, total rms (including the two segmented mirrors) of 30 nm and 56 nm, are presented. The wavelength is 650nm. The Strehl ratio follows the Marechal approximation:

$$St = \exp\left(-rms^2\right) \qquad \textit{Eq. 6-3.}$$

which gives St=0.92 for 30nm case and St=0.75 for 56nm case.

The residual PSF are shown in Figure 6-41 for the two values of RMS. Again we used the intensity slice representation. The overall speckles distribution follows the shape of the PSF of an individual segment of the primary mirror. A series of intensity slices is shown in Figure 6-41.

Full range *rms* = 30 nm *rms* = 56 nm

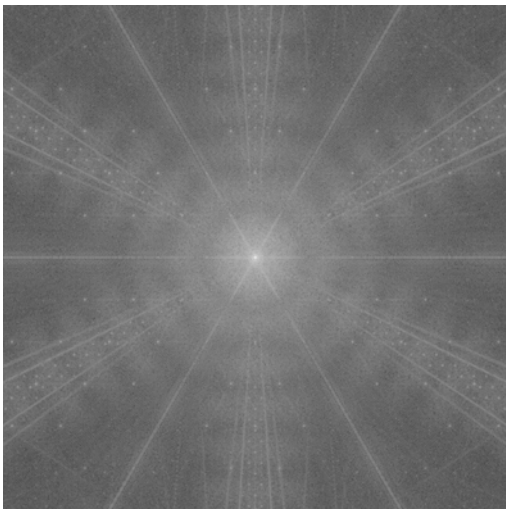

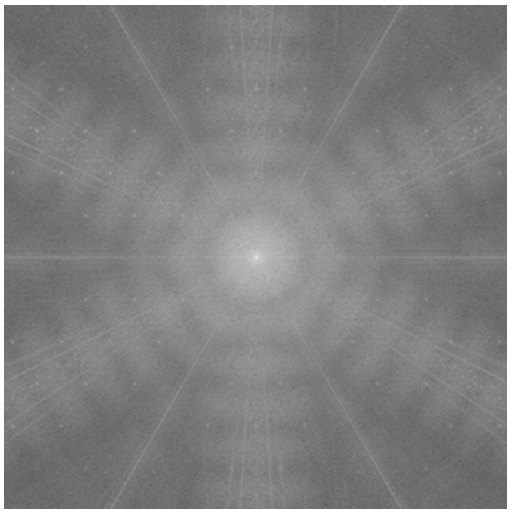

intensity slice 1 to 10^{-4} *rms* = 30 nm *rms* = 56 nm

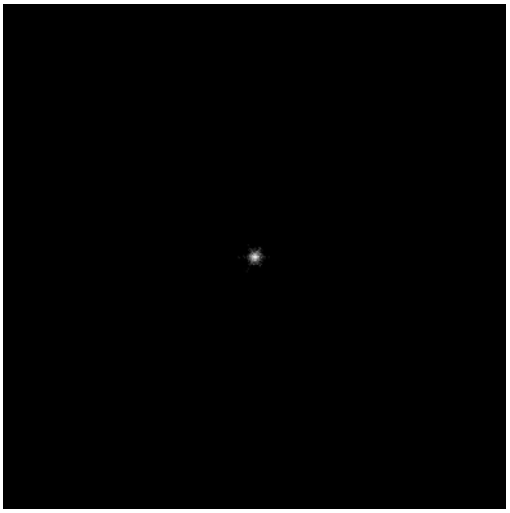

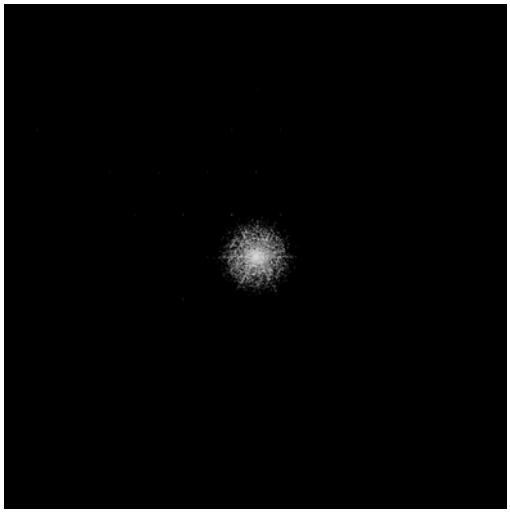

intensity slice 10^{-5} to 10^{-6} *rms* = 30 nm *rms* = 56 nm

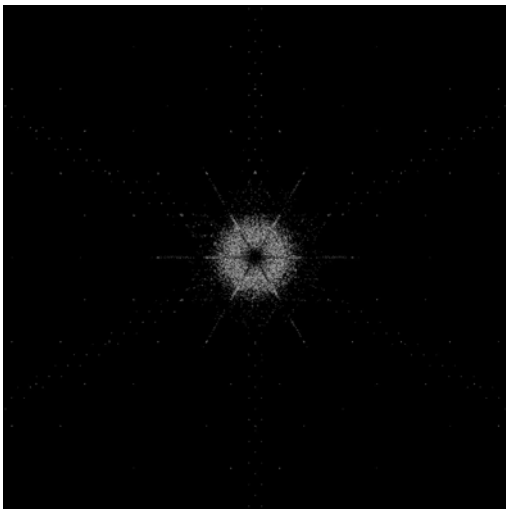

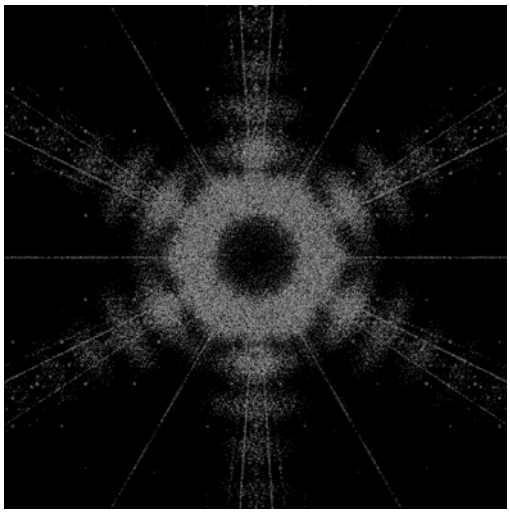

intensity slice 10^{-6} to 10^{-7} *rms* = 30 nm *rms* = 56 nm

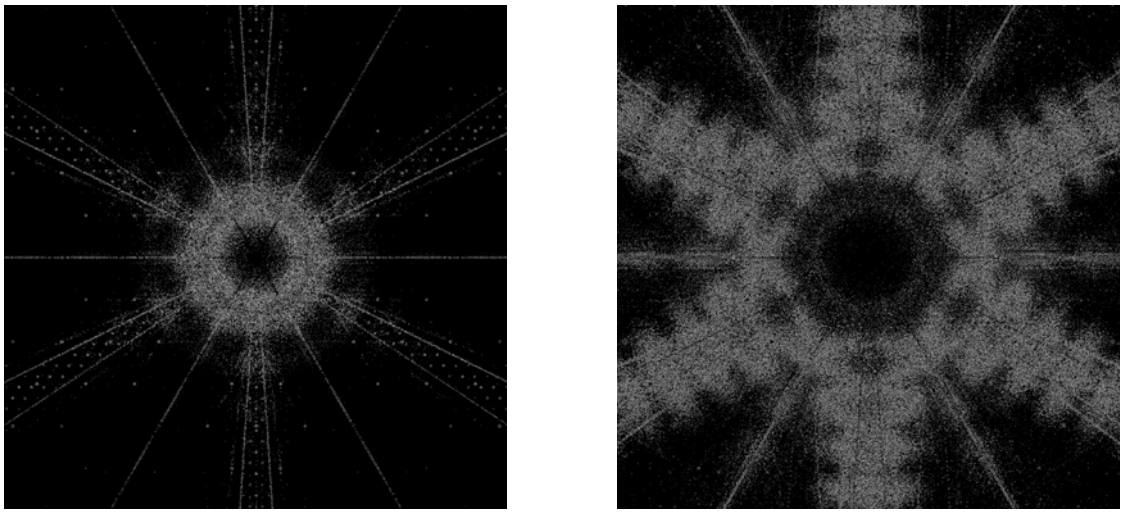

intensity slice 10^{-7} to 10^{-8}

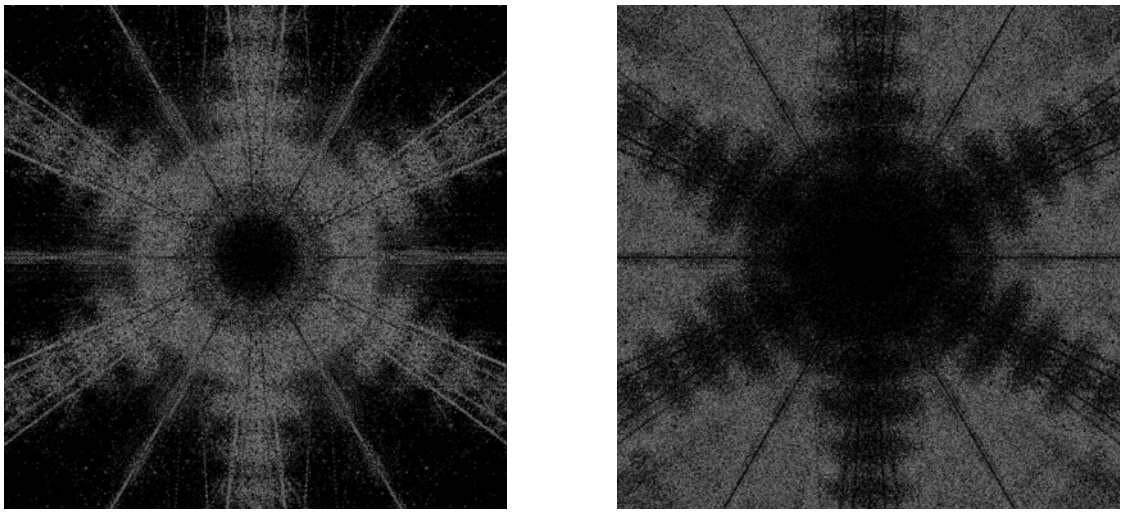

Figure 6-41 Intensity slice representation of OWL PSF with 30nm and 56nm wavefront RMS residual segmentation piston, tip-tilt errors on two segmented mirrors.

6.5 Optics design and fabrication

6.5.1 Segments

The segments product tree (excluding related documentation) is shown in Figure 6-42. The overall characteristics of the segments are given in Table 6-11. In the following sections we concentrate on segments distribution, support system, overall properties and fabrication issues.

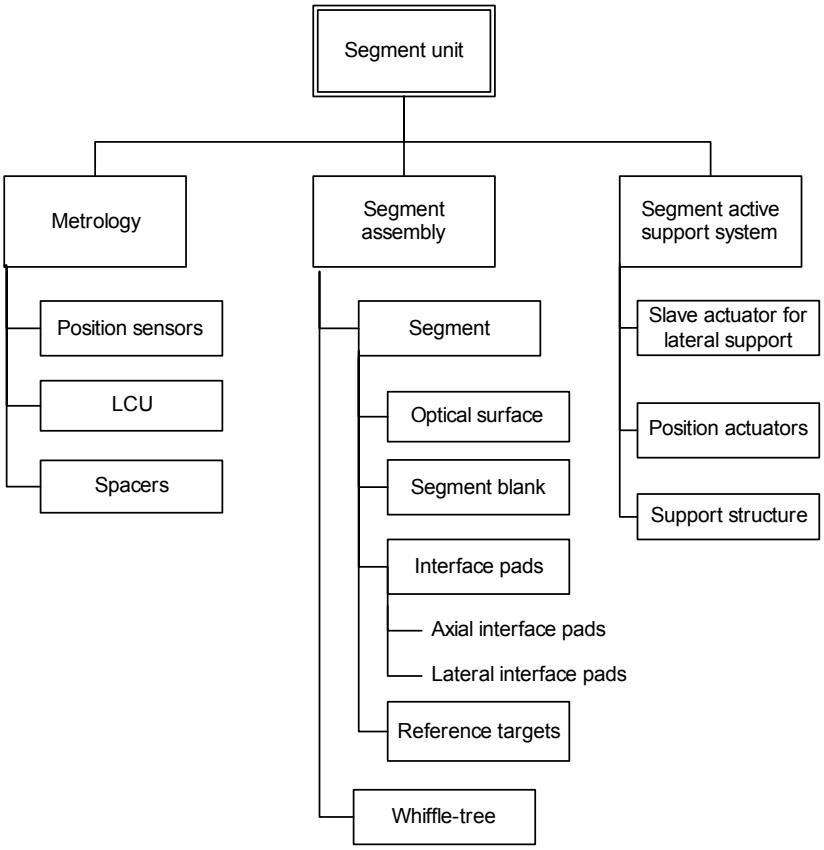

Figure 6-42. Segment unit product tree.

Characteristic		Value
Substrate		Zerodur, ULE or Astro-Sital
Shape / type		Hexagonal / solid
Dimensions	Flat-to-flat Thickness	1.6-m 70-mm
Radius of curvature	Primary mirror Secondary mirror	250-m Flat
Support	Axial Lateral	18 points whiffle-tree 1 central support
Quantity	Primary mirror Secondary mirror	3048 216

Table 6-11. Segments characteristics.

6.5.1.1 Segment size and distribution

The segments being spherical, optical figuring techniques do not imply the size limitations which may otherwise affect aspherical segments (e.g. maximum departure from a spherical surface, which could be generated by a warping harness). Handling and above all transport considerations point towards relatively small segments size, if possible compatible with standard transportation sizes i.e. 2.3-m flat-to-flat (the inner size of a standard 20 or 40 ft transport container). Larger segments would evidently simplify the position control (phasing) control system and reduce diffraction artefacts associated with intersegments gaps, but would imply excessive mirror masses and imply additional control complexity if their shape had to be

controlled actively. Industrial studies also concur[49] with a sharp cost increase beyond ~1.8-m. Small segments, a few tens centimetres, would have significant mass and handling advantages, and allow for higher bandwidth of their position control system. Beyond 4,000-5,000 units i.e. below ~1.2-m in size, however, it is generally felt that the complexity and cost of the position control system would negate the advantages brought by the smaller size.

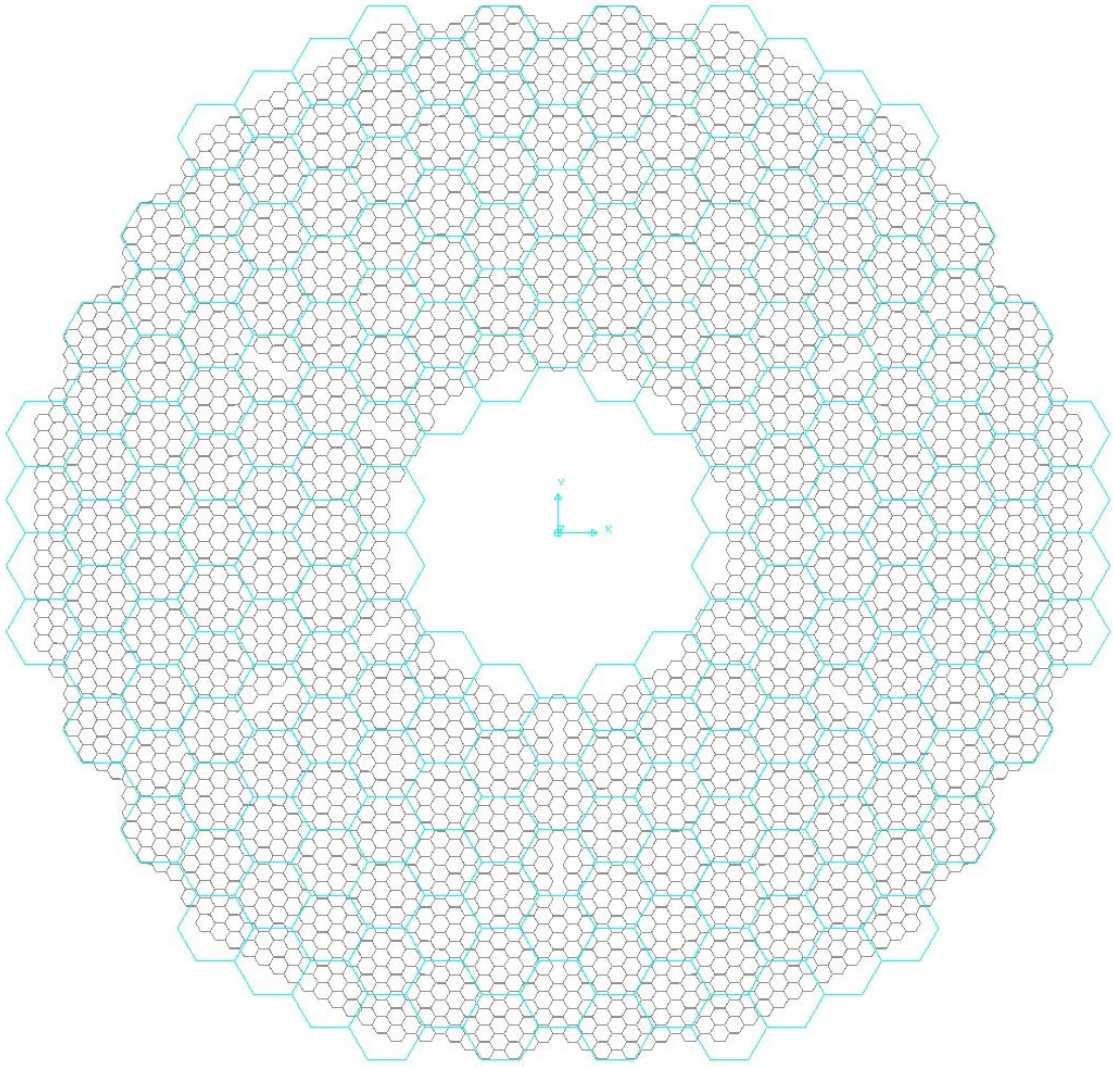

Figure 6-43. Primary and secondary mirror segments distributions.

The baseline segment size is 1.6-m flat-to-flat, with all segments identical. The dimension has been chosen as an integer divider (1:8) of the structural module size, thereby allowing for higher standardization of interfaces, and close to the presumed optimal in terms of production costs. The distribution of the primary and secondary mirror segments projection onto the pupil is shown in Figure 6-43. A refinement of the pupil geometry is likely as few (36) outer primary mirror segments appear to be strongly vignetted by the secondary mirror external contour.

In order to accommodate for the interfaces of the upper structures with the primary mirror cell and for supports of the mirror covers, the pupil is not uniformely paved but has obscurations with a six-fold symmetry (Figure 6-44).

All segments having the same dimensions, intersegments gaps are variable, from 4 to 14 mm (see RD46[50]). The radial intersegment gap is constant (14 mm) and the azimuthal variable (4 to

[49] See RD6, RD7, RD8, RD9, RD10, RD11, RD12.

[50] The values given in RD46 correspond to the former design iteration, with a longer focal ratio of the primary mirror.

13.5 mm). The azimuthal gap decreases with increasing radial coordinate of the segments (see Figure 6-44). A significant drawback of variable gaps is a potential loss of positioning accuracy with capacitive edge sensors[51]. An alternative technology (inductive sensors) is being assessed within the framework of the ELT Design Study (see RD504). The backup solution is to hold the position sensors on dismountable shims in order to guarantee that inter-sensors gaps remain constant. This would imply added sensors design complexity and segments maintenance complexity and, potentially, larger average intersegments gaps in order to accommodate for reasonable design space of the sensors interface with the segments.

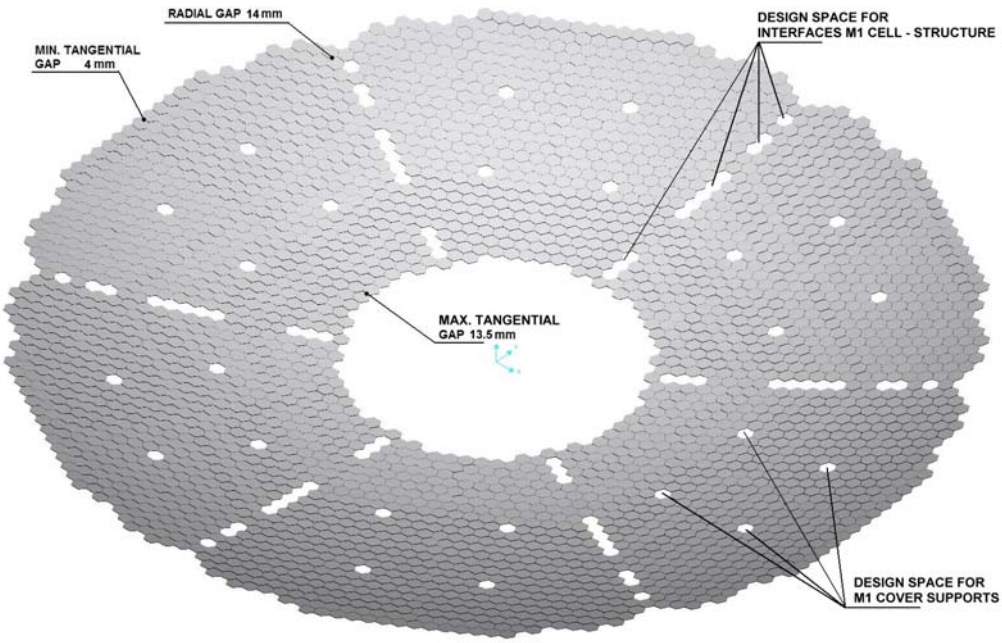

Figure 6-44. Primary mirror geometry, obscurations and intersegments gaps variation.

Primary and secondary mirror segments are identical but for their figure. A solution whereby the secondary mirror segments would have different size or outer cut, with its projected pattern onto the primary mirror coinciding with that of the primary mirror itself or with groups of segments in the prmary mirror, was briefly considered. This would be advantageous as one mirror phasing errors could be compensated by the other one. This is true, however, for a very small field of view only, as the patterns do no longer coincide off-axis. The tolerance would be comparable to the angular size of the secondary mirror gaps as seen from the primary mirror i.e. ~9 arc seconds for a 4 mm M2 intersegment gap. This approach was therefore abandoned.

6.5.1.2 Segments thermo-mechanical properties

A particular difficulty with segmented apertures is the tight tolerance on the repeatability of curvature between segments. While the overall curvature of a segmented mirror is still a matter of (a normally more generous) tolerance on the optical prescription, inter-segment curvature errors must be included in the segment misfigure or wavefront error budget.

Let us assume a tolerance of $\lambda/4$ peak-to-valley maximum allowable wavefront error (Maréchal criterion). A 1.6-m flat-to-flat dimension translates into a segment maximum radius of a=924 mm. The wavefront error W associated to a given error dR on the radius of curvature is given by

[51] According to FOGALE, SALT's supplier for its capacitive sensors, the accuracy specification is 50 nm Peak-to-Valley in piston (100 nm wavefront) and inter-segments gap variation (12 mm) is the single most important contributor to the allocated error budget.

$$W = \frac{dR}{4}\left(\frac{a}{R}\right)^2 \qquad \textit{Eq. 6-4.}$$

With the primary mirror (R = 250000 mm) and λ=0.5 μm, we find dR=9.6 mm i.e. dR/R=0.0038%. This is an extremely stringent tolerance, which not only implies tight optical figuring constraints but also stringent material specifications. The potential concerns, as detailed by Nelson et al for the Keck telescope [12] are:

1. differential change of curvature between segments (primary mirror only, the secondary being assumed flat).
2. differential segment thickness expansion, and thereby a differential displacement of the optical surfaces with respect to position sensors.
3. CTE or thermal gradients within individual segments.

All three effects have been investigated with Zerodur, fused silica and silicon carbide (see RD3[52]) and the first two found negligible. The third one, however, is critical (see Table 6-12). Silicon carbide has a slight advantage because of its excellent thermal conductivity but through-thickness CTE variations are still critical. The bulk of the optical surface deformation is defocus. It should be noted, however, that for lack of precise data, the calculation underlying Table 6-12 is extremely pessimistic since it assumes a linear through-thickness CTE gradient. There is circumstancial evidence that this is not the case; silicon carbide mirrors and structures, for example, have shown remarkable stability (a few micrometers) over wide thermal excursion down to cryogenic temperatures. Whether this is also true for silicon carbide mirrors overcoated with a polishable cladding remains to be proven. This issue is being addressed in the framework of the ELT Design Study, with the fabrication and testing of up to 8 silicon carbide segment prototypes, 1-m class (see RD510).

Error source: CTE and thermal gradient within segments; variation 5 K between operational and fabrication temperature.	Zerodur (class 2)			Fused Silica			Silicon Carbide		
	Wavefront RMS (nm)			Wavefront RMS (nm)			Wavefront RMS (nm)		
	M1	M2	**Total**	M1	M2	**Total**	M1	M2	**Total**
Front-back $\delta\alpha=10^{-8}$ K^{-1}	153	153	**216**	153	153	**216**	153	153	**216**
Heat flow dispersion 3 $W.m^{-2}$	50	50	**70**	17	17	**24**	9	9	**13**
TOTAL (RMS SUMMATION)			**227**			**218**			**217**

Table 6-12. Compared performance of Zerodur, fused silica and silicon carbide with respect to through-thickness CTE and thermal gradients (1.6-m flat-to-flat, 70 mm thick segments).

A possible solution to reduce the effect of CTE inhomogeneities and/or avoid CTE specifications which would exclude otherwise attractive materials is to specify the segments figure at median operation temperature so as to minimize the operational departure from factory conditions. This solution would only require that the segments be tested at operational temperature; figuring could still be executed at normal factory temperature and would only have to be tuned to produce the desired curvature at test temperature. Assuming a matrix test configuration, the technical difficulty and extra cost of cooling the test set-up (matrix and segment) down to ~5 ^{o}C, although not negligible, is still affordable (see RD11 and RD12).

6.5.1.3 Segments substrates

The baseline segment substrate is low-expansion glass or glass-ceramic (Astro-Sital, ULE or Zerodur), with Silicon carbide as an actively pursued alternative. Preliminary blanks specifications are given in RD42 and RD43. The segments dimensions have slightly evolved

[52] The results in RD3 are obtained with 80 mm thick, 1.8-m flat-to-flat segments. Results shown in Table 6-12 have been scaled to the baseline segment dimensions: 70 m thick, 1.6-m flat-to-flat.

since the time of writing of these reference documents, the dimensions provided in Figure 6-45 and Figure 6-46 are superseding.

Parametric studies for the blanks production in low-expansion glass or glass-ceramic have been undertaken by suppliers under ESO contract (see RD6, RD7, RD8). Equivalent studies have been undertaken with silicon carbide (see RD9 and RD10). The specified leadtime from signature of supply contract to the delivery of the last segment was 10 years, with 8 years as a goal. It came out of the studies that the faster schedule could be met, in some instances at an even lower (by ~5%) cost than the longer one. The specified leadtime included a 2 to 3 years provision for facilitization.

These studies covered three possible dimensions: 1.3, 1.8 and 2.3-m flat-to-flat. All studies concurred that the cost vs diameter curve was rather flat, with the lower and upper dimensions slightly (~5-10%) to significantly (~30-40%) more expensive. Yield was conservatively assumed to be constant over the production cycle i.e. no provisions were made for otherwise plausible improvements of yield with time and accumulated experience. Due to facility limitations, ULE is cost-effective with dimensions of up to 1.5-m.

With Zerodur, Astrosital and ULE, production of OWL segments blanks would require duplication of existing infrastructures but no particular process development. Schott and Corning recently reported a substantial increase in capacity, motivated by a surge in the market for large Zerodur and ULE components. In a follow-up of the initial study Schott reported that with a total capacity of 700 tons/year its current facilities are now close to meeting the requirements for the supply of OWL segments. According to Schott this capacity could be increased by up to 20% without requiring major investment. Schott also gained experience with hexagonal casts (Figure 6-47), allowing for 17% savings on raw material. A single cast could be cut into up to 3 segments. Availability of such facitlities at the time of purchase of OWL blanks is evidently not guaranteed, but further extension is possible. Facilitization would take less time than initially anticipated (~1 instead of 2-3 years) and production could ramp up within the second year after signature of the contract.

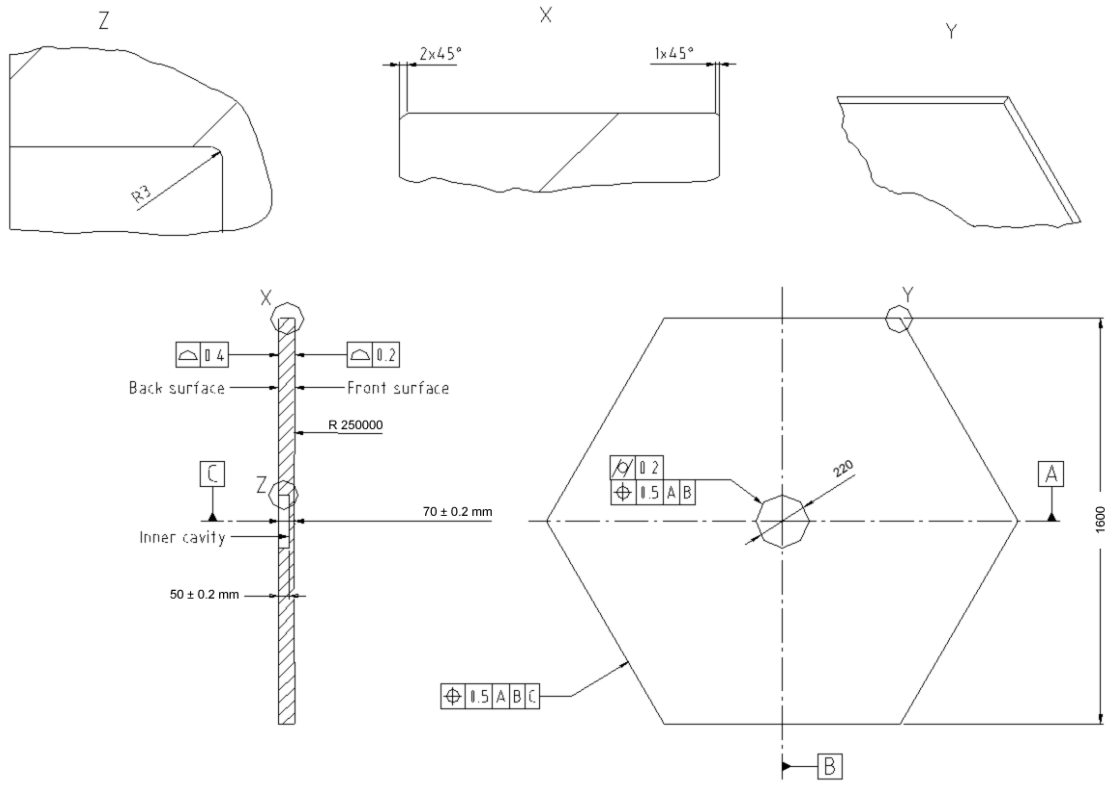

Figure 6-45. Primary mirror segment blank.

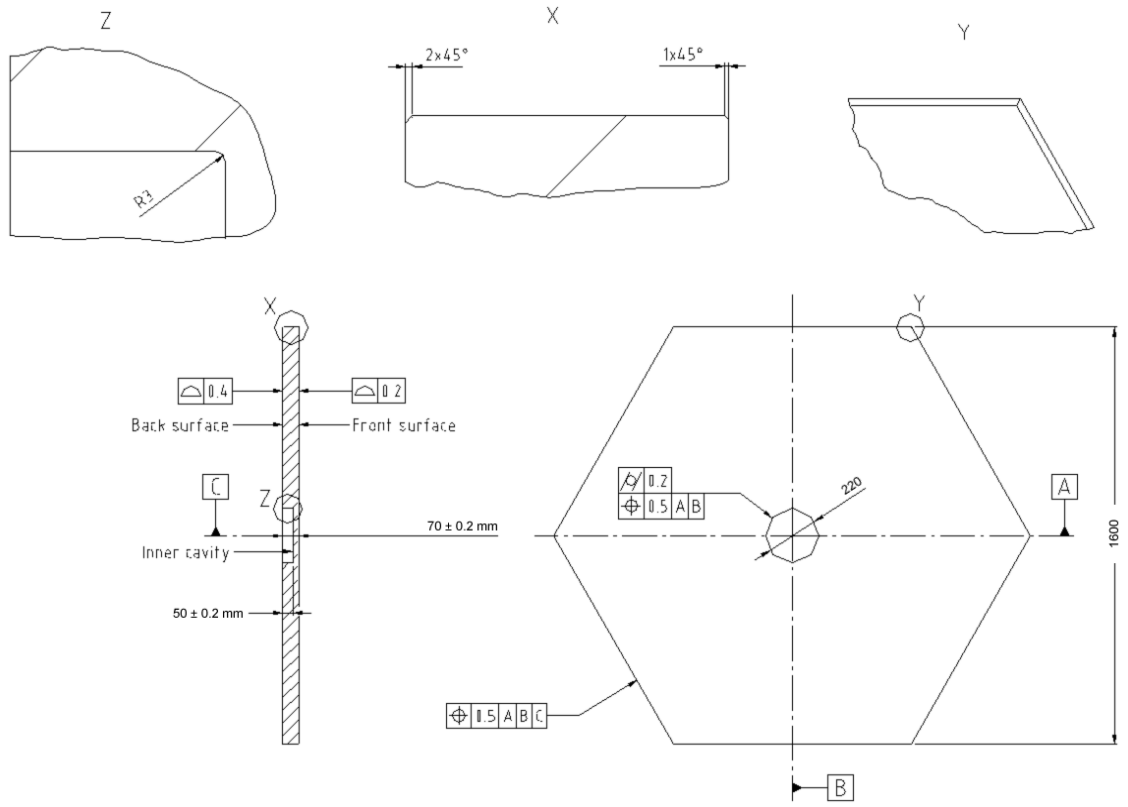

Figure 6-46. Secondary mirror segment blank.

With several hundreds of segments produced, robust statistics reveal the consistent and excellent homogeneity of Zerodur (Figure 6-48). Through-thickness CTE gradients, a possible concern for segmented apertures (see RD3), are below 0.010×10^{-6} K^{-1}, with measured values most frequently below 0.002×10^{-6} K^{-1}.

At the time of writing of this document, the option of segments moderate lightweighting is under investigation. Recent process developments would allow a substantial gain in machining time. The process has been verified on ~1-m Zerodur slabs. Provided the lightweighting geometry remains simple (circular pockets) and the lightweighting ratio does not exceed ~50%, thereby allowing safe rib and front plate thickness, lightweight, 70-mm thick, 1.6-m flat-to-flat segments blanks might be produced within a manageable cost increase.

Low-expansion glass or glass-ceramic is the current baseline for OWL segments, but the development of silicon carbide as an alternative is actively pursued. Figure 6-49 shows the thermo-mechanical figure of merit of several materials. The x-axis corresponds to the ratio of the CTE divided by thermal conductivity (representative of transient surface change under thermal load) and the y-axis corresponds to the inverse of the specific stiffness i.e. the ratio of density divided by Young's modulus (representative of e.g. total mass for a specified deflection under external load). The superior characteristics of silicon carbide are evident.

Figure 6-47. Zerodur hexagonal cast. Courtesy Schott.

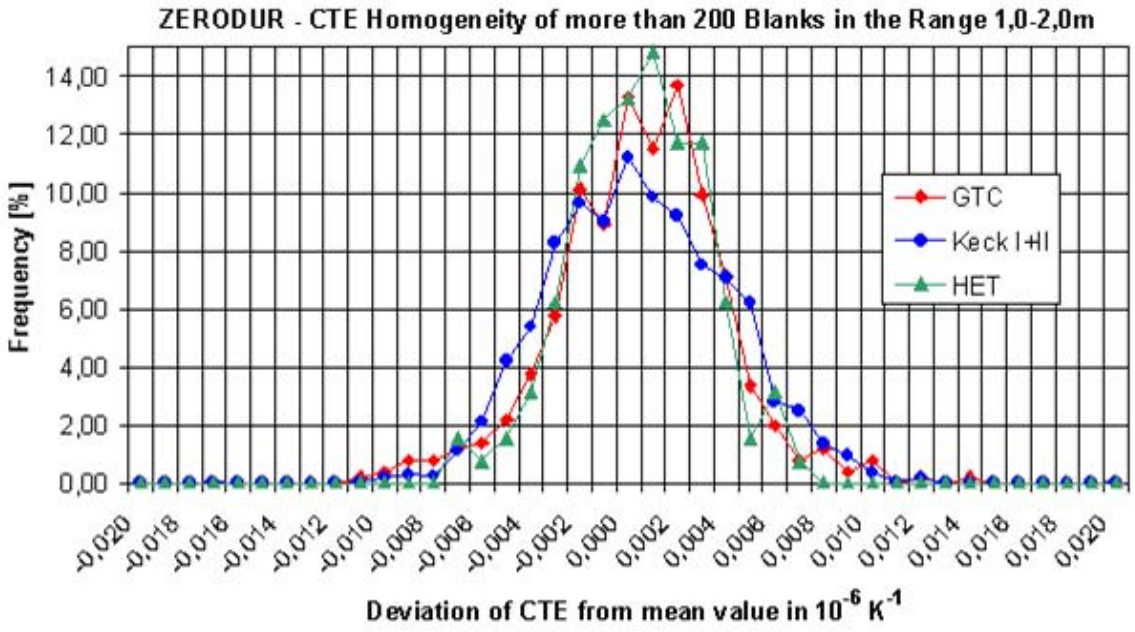

Figure 6-48. CTE homogeneity of Zerodur. Courtesy Schott.

Silicon carbide would allow for a substantially lower (by a factor ~6) segments mass, thereby implying an estimated 30% reduction of the telescope moving mass[53], relaxed segment actuator specifications and, potentially, higher control bandwidth. In view of its excellent thermal conductivity it would simplify thermal control, the primary and/or secondary mirrors being able to

[53] This figure includes a substantial reduction of the telescope structural mass.

passively reach thermal equilibrium with ambient conditions. Secondary mirror covers would no longer be required. Surface hardness is also an advantage in terms of durability.

Silicon carbide mirrors have been produced since the mid-80s, generally for ultra-lightweight, stable space structures and reflective optics. An industrial study commissioned in 1989 under ESO contract for the VLT 1.12-m secondary mirrors, concluded that such mirrors would be feasible and have an aerial mass of about 40 Kg/m². A contract was subsequently placed for the supply of the four electromechanical M2 units, with silicon carbide mirrors. After a machining accident at the silicon carbide supplier premises, however, the contract had to be cancelled as the supplier's mother company decided to close its activities in the area of optical substrates, which it regarded as a fringe market. The reason given for the accident was essentially related to inadequate, worn out machining tools –i.e. nothing that could not have been easily remedied. The VLT secondary mirrors were eventually made in Beryllium, at a significantly higher cost.

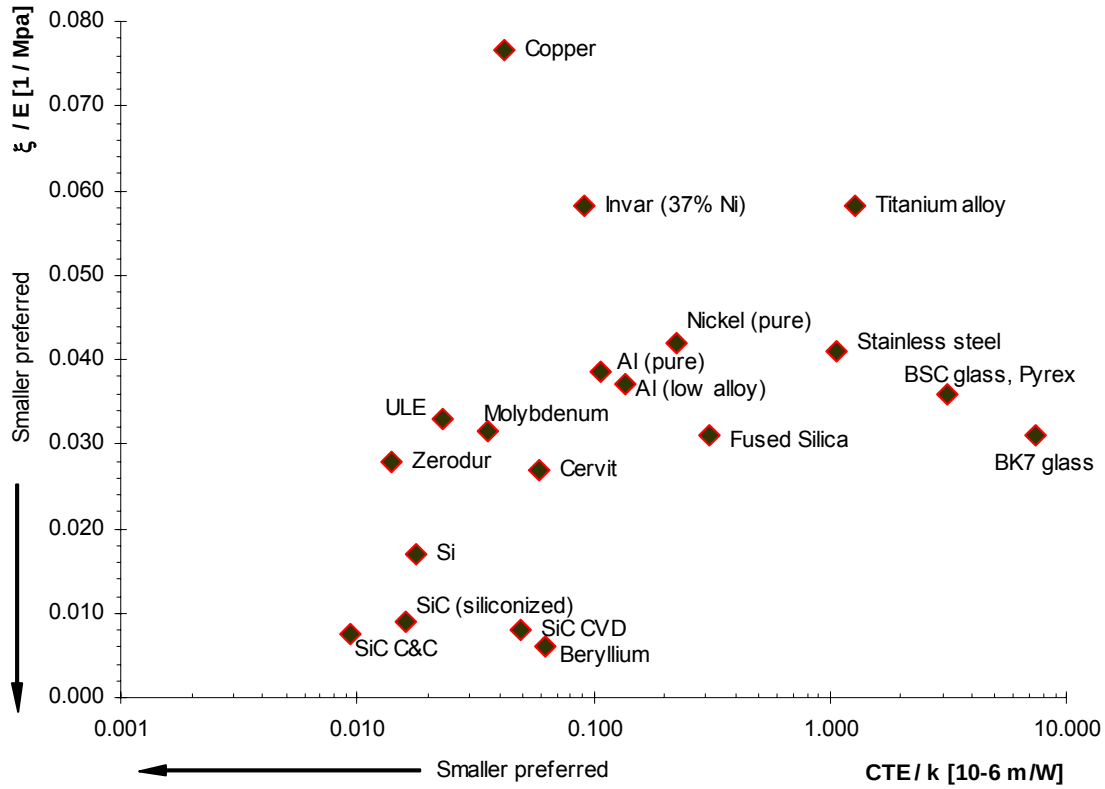

Figure 6-49. Thermo-mechanical figure of merit.

Silicon carbide has been traditionally regarded as a high-end, very expensive technology. The main reason is the extremely low mass target underlying space applications. In addition to requiring numerous and expensive qualification tests and models, this implies lengthy machine cycles as tool speed must be reduced to prevent breakage of exceedingly thin ribs. With low material cost and relatively fast (a dew days at most) cold-to-cold sintering or infiltration processes, there is no intrinsic reason for silicon carbide blanks to be more expensive than conventional materials (figuring and polishing, however, are considerably more costly, see 6.5.1.4). This has been, to some extent, confirmed by studies contracted to European suppliers (see RD9 and RD10) for the production of OWL segments, priority being given to minimal cost over aerial density (goal 70 kg/m² or less). Depending on supplier, process, and on whether blanks would be delivered with polishable overcoating or not, cost estimates range from about half the cost of solid glass-ceramic ones to comparable figures.

Boostec sintered blanks are made from SiC powder, cold-pressed with an organic binder at ~1000 Bar into a precursor ("green body", see Figure 6-50) which is subsequently machined to

near-net shape before de-binding and eventually sintering at ~2100 °C. Shrinking upon sintering is about 15% linear but reproducible[54]. The final blank is polishable but residual porosity (~1%-3%, depending on powder size) is generally incompatible with visible optical applications. Machining operations of the sintered blank must be minimized in view of its hardness[55]. Material ground out of the precursor could be recycled. Blanks up to 1.3-m could be made from a single pressed precursor, size being limited by the availability of suitable cold isostatic pressing facilities. Larger segments would be assembled from smaller precursor parts by brazing, bonding or bolting prior to infiltration –with brazing as the baseline solution. This technique has been successfully applied to the 3.5-m Herschel primary mirror [13]. There is no evidence of discontinuity or weakness at the brazed joints. Boostec reports a CTE homogeneity in the range of 0.005×10^{-9} K^{-1}, measured on different batches over several years.

Four segment blank prototypes (Figure 6-50), 1-m flat-to-flat, have been delivered by Boostec under ESO contract and will be polished and tested within the framework of the ELT Design Study (see A-1.3). Up to four more will be procured from a different supplier (see RD510).

Figure 6-50. Precursor (left) and 1-m sintered SiC segment (right). Courtesy Boostec.

ECM CESIC blanks are made by infiltrating a felt with silicon, at approximately 1800 °C, without significant dimensional change down to ~0.015% of linear dimensions. As with sintered silicon carbide, most machining can (and should) be done on the precursor. Beyond 1-m or 80-mm thickness, blanks must be assembled by bonding several parts before infiltration. There is no evidence of any discontinuity of weakness at the joints. Raw material being the major cost position, the option of assembling the entire back structure from smaller, serially produced plates and joints ("Lego" approach), could be an alternative to machining it out of a solid prescursor. A small (30cm) demonstrator blank has been produced.

Residual carbon content prevents clean optical finish and CESIC blanks also require a polishable overcoating, typically ~200-300 μm thick. One option is to depose a polishable slurry (ECM proprietary process) prior to a second firing run.

Both Boostec and ECM see no major issue in complying with a production cycle of 6 years after up to 2 years facilitization. In both cases a dedicated facility would have to be built, but the required equipment would be a mere duplication of existing ones. It is worth noting that both suppliers are operating furnaces already compatible with OWL segments characteristics. With sintered silicon carbide, the required yield for OWL would be about 50 tons/year, i.e. a significant but not major increase in relation to a 350 tons worldwide production in 2001. Based on the experience gathered with the 3.5-m blank for the Herschel IR telescope [13], it appears that an aerial mass specification lower than the specified maximum of 70 Kg/m² might be achievable without significant overcost.

[54] Typically ~0.4% of linear size.

[55] Hardness of the precursor material is low, thereby permitting fast machining. In this state the blank is however fragile, which is one of the reasons for the high cost of ultra-lightweight, thin ribs structures. Ribs, front plate thickness and lightweighting geometry of OWL segments could be kept within safe values.

A third European supplier (SNECMA) is currently in the process of validating an attractive technology (StarSic), whereby siliconization of the precursor and deposition of a polishable overcoating would be performed in one single furnace run. The process would therefore be potentially cost-effective. Preliminary results of thermal tests on a first 15-cm polishing sample are quite promising, with surface deflections in the range of $\lambda/8$ between room temperature and -10 °C. These deflections are probably related to a less-tan optimal machining of the precursor, which resulted in an irregular overcoating thickness after polishing. SNECMA already operates large facilities and has been a supplier of polishable overcoatings (ICVI) for silicon carbide mirrors.

6.5.1.4 Segments polishing

Preliminary specifications for the figuring and polishing of OWL primary and secondary mirror segments are given in RD44 and RD45 for glass-ceramic and silicon carbide segments, respectively. Optical quality requirements are summarized in Figure 6-51 (wavefront slope) and Figure 6-52 (wavefront amplitude). They include specifications applicable to any single segment and specifications applicable to the entire production. The overall wavefront error specification corresponds to seeing-limited operation; residuals after removal of low order terms take into account a minor correction of residual errors by the adaptive mirror M6, while residuals after removal of low- and mid-frequency terms take into account higher order adaptive optics correction. Preliminary definitions of low- and mid-order terms are given in terms of Zernike polynomials (see RD44 and RD45). Slopes are not directly measured but calculated from phase maps and therefore, strongly affected by the measurement noise on wavefront amplitude. Slopes specifications will eventually be replaced in favour of a finer descriptive of the allowable spectral content of the misfigure.

The definitions (polynomial orders) are different for the primary and secondary mirror segments, to take account of the different segments projected size onto the pupil. In the case of primary mirror segments, low order terms are third order aberrations, mid-frequency ones include seventgh order terms. The corresponding orders for the secondary mirror segments are 7^{th} (low order) and 11^{th} (mid-spatial frequency), respectively. The specifications given in Figure 6-51 and Figure 6-52 include curvature deviation from an average calculated on the basis of the 15 first produced segments.

In order to guarantee best performance in operational conditions and minimize the effect of through-thickness CTE gradients (see RD3), the specifications require that segments be tested at the presumed median operational temperature (5 °C). Figuring and polishing may of course be performed at room temperature.

Optical replication had been briefly considered at an earlier stage. This technology had been successfully developed by CERGA, now part of Observatoire de la Côte d'Azur, with ESO support in the late 1980s. The high forces applied during unmolding, however, imply high stresses in the parts and durability of the master is a potential issue. In addition, surface stresses generated during polimerization of the ~0.2 mm thick epoxy layer may lead to unpredictable warping. This path was, therefore, abandoned.

Two competitive studies have been performed under ESO contract, both for the polishing of either glass-ceramic or silicon carbide segments, and with segments dimensions of 1.3, 1.8 and 2.3-m flat-to-flat. Total price variation between the two lower sizes seems negligible. The larger size would lead to a price increase of ~20%. The specified schedule was 10 years from signature of the contract to the delivery of the last segment, with eight years as a goal. Both suppliers claim they could meet the goal. Facilitization would take 2 to 3 years and is included in the specifed shedule.

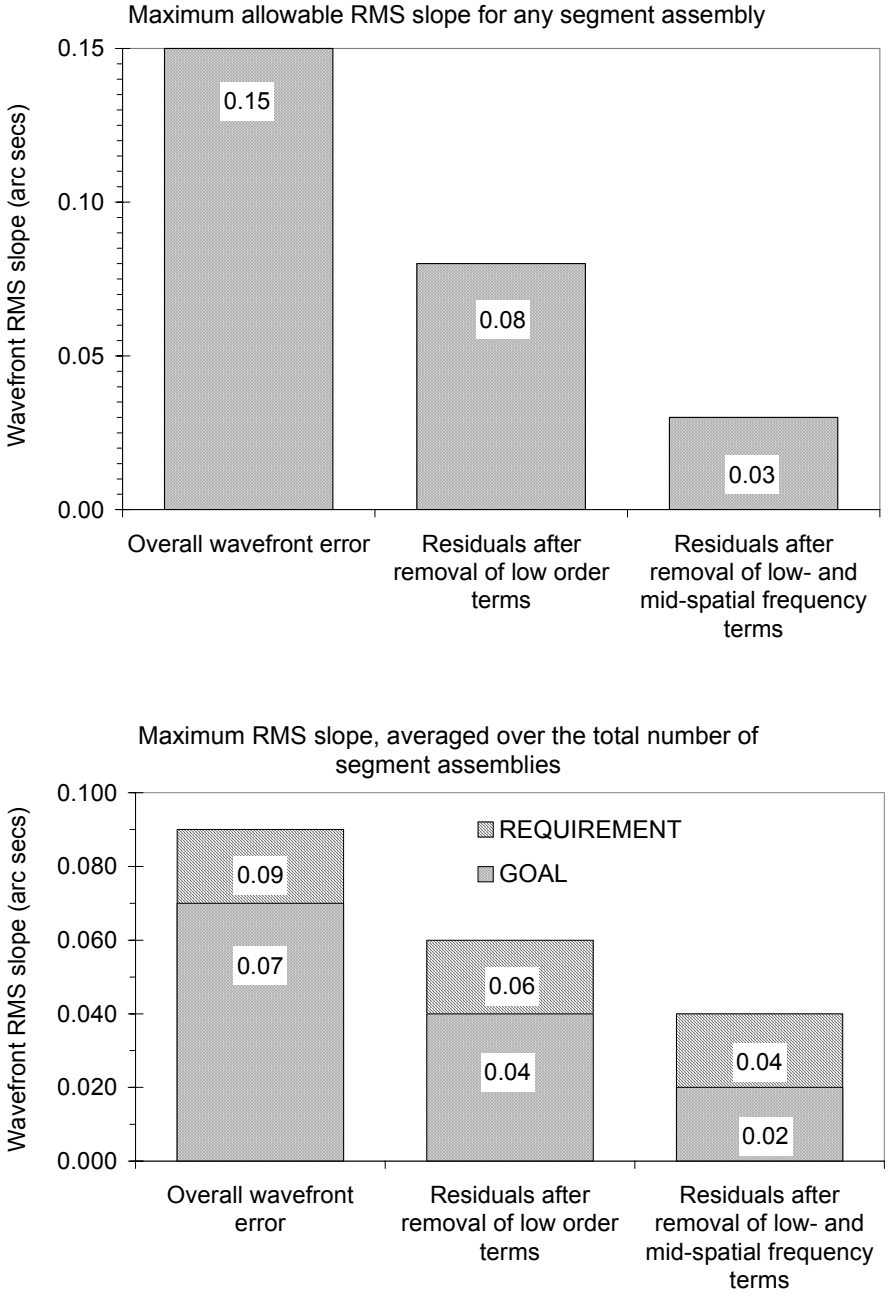

Figure 6-51. Segments optical quality (rms slope) specifications.

The suppliers considered planetary or double-side polishing as well as figuring and polishing on computer-controlled individual machines. Performance, reliability and cost of large planetary polisher is a potential issue with segments beyond ~1-m in size, and both optical manufacturers eventually selected parallel grinding and polishing of individual segments, to be complemented by either ion-beam or small tool computer-controlled polishing. The required production capacity is about 1.6 segments per day with 1.8-m segments, taking into account a 1% loss rate and assuming 6 working days per week, 46 working weeks per year. Processing several segments simultaneously on large machines is rather inconvenient as it would require complex handling and assembling operations, safety issues, and be less robust in terms of impact of failure on the production rate.

With polyurethane-coated large tools, the total number of machines is relatively modest anyway: 2 grinding computer-controlled machines, 5 polsihing ones (1.8-m segments). A dedicated production facility would have to be built. According to suppliers its size would be two to three

times the size of the factory built by REOSC for the prodcution of the VLT primary mirrors. No new, unproven or particularly challenging equipment would have to be developped.

According to specifications the segments would have to be acid-etched (back surface). The segments being passively supported during polishing and in operation, such acid-etching might be unnecessary. Removing this operation would lead to a small but significant reduction of total price.

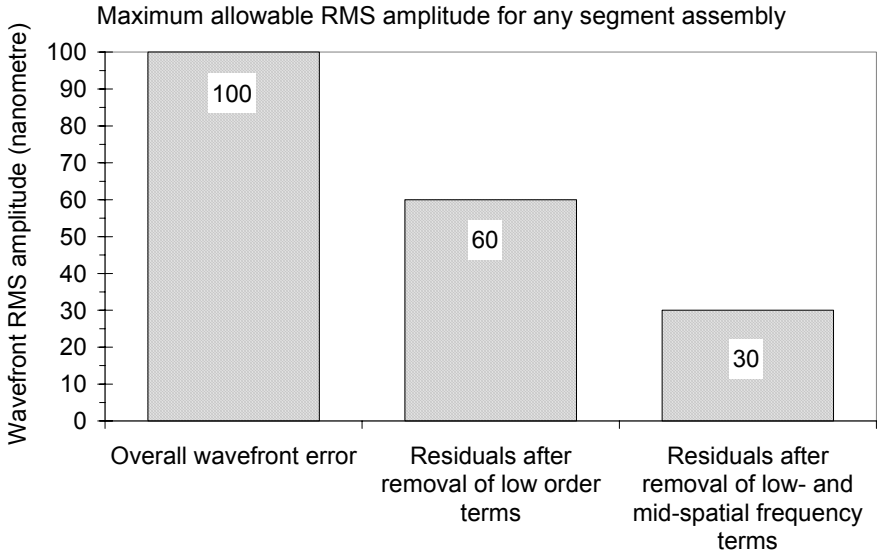

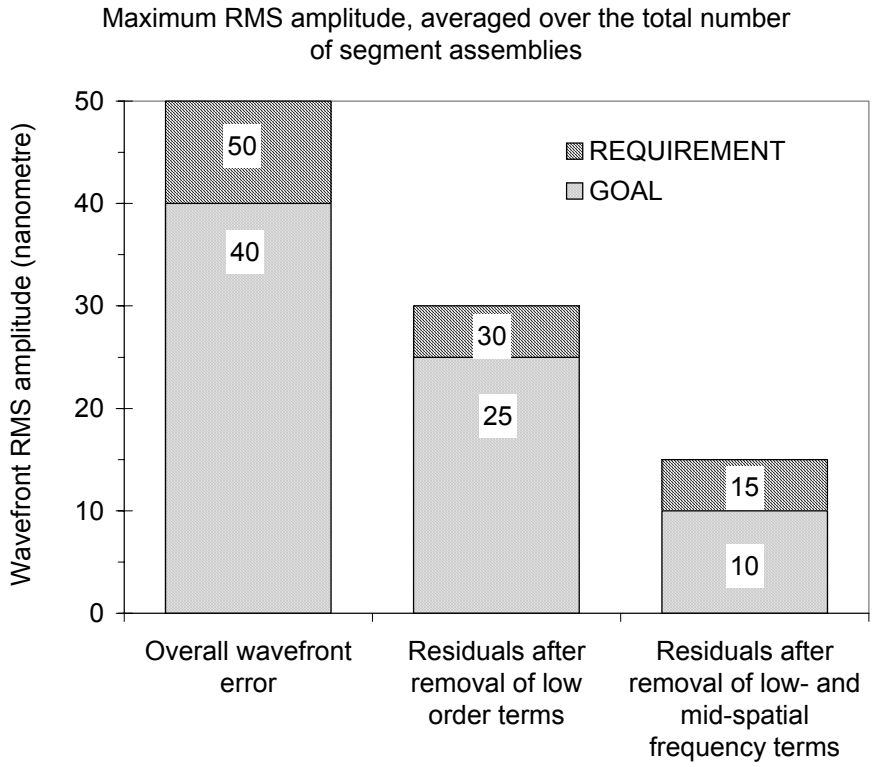

Figure 6-52. Segments optical quality (rms amplitude) specifications.

Wasters (polishing extensions) would be assembled onto the segments edges to reduce edge misfigure, as done with GTC segments. The spherical shape of OWL primary mirror is however favorable in that it allows the use of large, stiff tools, which are inherently better in relation to high spatial frequency errors, including edge misfigure. It is worth noting that a prototype LAMOST segment (spherical) has been polished without wasters, to adequate quality. Removing the need for wasters would lead to a significant reduction in total price. Further tests are necessary and will be performed on 1-m silicon carbide segments, within the framework of the ELT Design Study (see A-1.3).

Segments would be tested interferometrically through a common matrix, segments mounted onto their operational support systems, face up for the primary mirror, face down for the secondary mirror ones. Segments would be tested against a matrix (convex for the primary, flat for the secondary mirror). Two matrices are required, one for testing at room temeperature in the early phases of polishing, one for testing at 5 °C before finishing and for acceptance testing.

With 1.8-m glass-ceramic segments, industrial price estimates coincide within a few percents, and are broadly (within ~10%) in-line with ESO's internal estimate made at an earlier stage.

Polishing of silicon carbide segments is far more expensive. First, SiC segments are not directly polishable and an overcoating is required after fine grinding. Possible options include CVD, ICVI or depostion of a polishable slurry, the latter applicable with ECM infiltrated blanks only. Second, the grinding and polishing of silicon carbide requires very expensive abrasives –boron carbide and diamond- and no convenient solution has been found to recycle the slurries after use. Processing time is longer in view of the higher hardness of the material. Homogeneity of the thickness of the overcoating is also a potential issue for the optical manufacturer. Taking these factors into account, the polishing of silicon carbide segments is a factor 2.1 to 2.6 more expensive that the polishing of glass-ceramic ones. In addition, there is a potential issue of surface stresses and CTE mismatch between the bulk of the substrate and the polishable overcoating, as already mentioned.

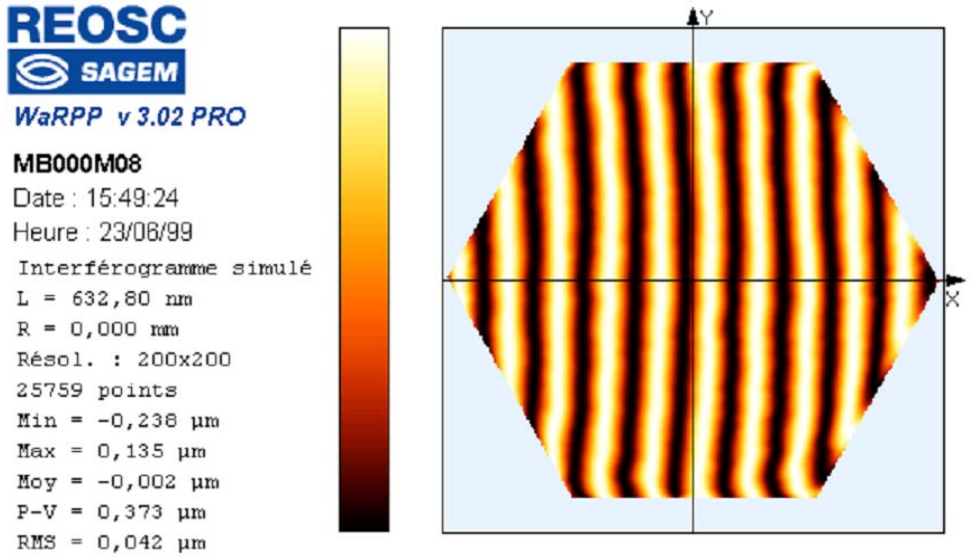

Figure 6-53. Interferogram of a LAMOST 1-m spherical segment prototype. Courtesy REOSC.

The additional cost of coating and polishing SiC segments, however, might be offset by the lower cost of raw blanks, the lower cost (mass) of the telescope structure and of the segments supports, and by the potentially higher bandwidth of the segments position control. Actuator cost and performance in relation to segment mass not having been evaluated at the time of writing of this document, a rigorous cost analysis is not possible yet. Actuator characteristics vs segment mass will be evaluated within the framework of the ELT Design Study (see A-1.2).

Furthermore, cost-effective alternatives to diamond slurries and to CVD or ICVI overcoatings might be available, and will be tested within the framewrok of the ELT Design Study (see A-1.3). Progress in the development by SNECMA of polishable blanks also ought to be closely

followed. According to plans, OWL primary mirror technology should be frozen by early 2008. By that time, and within the framewrok of the ELT Design Study, up to eight prototype segments will have been polished and tested, with different substrates and different possible overcoatings. These prototype segments are flat and will be measured interferometrically against a flat reference, at different temperatures, with a view to detecting CTE inhomogeneities and CTE mismatch between the polishable overcoating and the bulk of the substrate.

6.5.1.5 Segments supports

A preliminary parametric study of the segments axial support has been performed, with a view to deriving an optimal compromise between support geometry, segment thickness, and tolerances of support pads position. This study is documented in RD47. With similar segments dimensions, Keck and GTC opted for a 36-axial supports. Considering the number of OWL segments, it would be highly desirable to reduce the complexity of the support system. There are hopefully a number of factors that may allow doing so.

Figure 6-54 shows the deflection under gravity of a 70 mm thick Zerodur segment (one 60° sector shown), 1.6-m flat-to-flat, on an optimized distribution of 18 axial supports, and as predicted by Finite Element Modelling (FEM). The surface deflection is 31 nm RMS. A series of 50 runs with random axial position errors of up to ±1 mm leads to less than 1 nm i.e. negligible standard deviation.

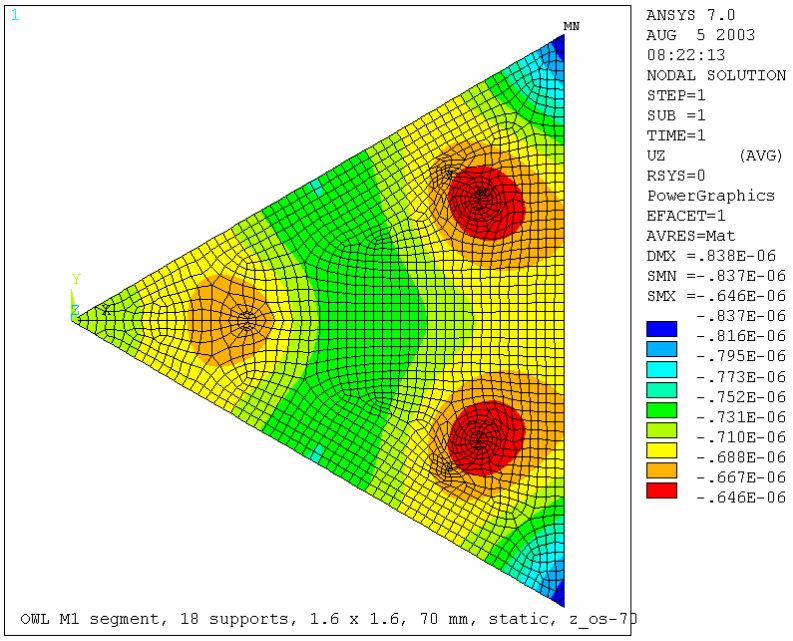

Figure 6-54. Segment deflection on axial support. Zerodur, thickness 70 mm.

A surface deflection of 31 nm RMS (62 nm RMS wavefront) would in principle not be acceptable. If, however, the error could be polished out with segment laying horizontal, it would follow a cosine of zenithal distance (z) law. In operation up to 60° form zenith, it would de facto be reduced by a factor two compared to the model shown herein –i.e. the axial support print-through would vary from 0 at zenith to 16 nm RMS at z=60°. Whether this is possible has actually been proven by REOSC (now SAGEM) in the lat 1980s. Within the framework of the VLT primary mirror polishing contract, REOSC supplied a 1.7-m Zerodur blank and polished it to serve as a reference (gauge) for the calibration of spherometric measurements on the 8-m mirrors. The spherical gauge mirror was polished with large stiff tools on supports mimicking those of the 8-m mirrors. No evidence of the print-through predicted by Finite Element Modelling (about 52 nm wavefront RMS) could be detected, even though the gauge was tested interferometrically. Even though the VLT primary mirrors were polished with flexible tools, no

evidence of any-print-through could be found either (the accuracy of the measurements was better than 10 nm wavefront RMS).

Actually, figuring and polishing of the segments on the same support distribution as in the telescope will *inevitably* converge towards the desired shape with the segment lying horizontal.

This, however, applies only to the primary mirror segments. In the case of the secondary mirror, the error would be doubled. A possible way around would be to test the (flat) secondary mirror segments against a reference, with the segments facing down. In the last runs of polishing (either small tool or ion-beam figuring), the residual misfigure on support could be corrected by the polishing process –provided that doing so does not require more than one or two polishing runs, which seems to be the case. Furthermore, spatial frequencies on the secondary mirror correspond to ~4 times lower frequencies in the pupil. With a separation of ~60 cm between M2 segments supports, residual flexures of the segments would be seen by the adaptive systems as DC errors with a spatial period of ~2.4-m in the pupil and a fairly small amplitude compared to atmospheric turbulence.

No analysis has been done with silicon carbide segments. The higher specific thickness of silicon carbide, together with the moderate requirements on lightweighting, should lead to more favorable results.

All the above remains fairly notional. Further design, analysis and tests will be required once the segments substrate and exact geometry will be finalized. According to plans, phase B includes design and testing of prototype segments and support systems. Analysis shall cover the performance of axial and lateral supports in relation to gravity, thermal change, allowable integration errors, and spurious bending moments. Should results not allow the segments to be supported on 18 axial supports, a 36 supports system is considered as a backup.

6.5.2 Corrector optics

In the following we concentrate on the fabrication of the 8-m class tertiary and quaternary mirrors. The adaptive M5 and M6 mirrors are described in sections 8.3 and 8.2.1.2.1, respectively.

For M3 and M4 the baseline approach is to follow as closely as possible the VLT 8-m mirror design, including fabrication, handling, transport, operation and maintenance concepts.

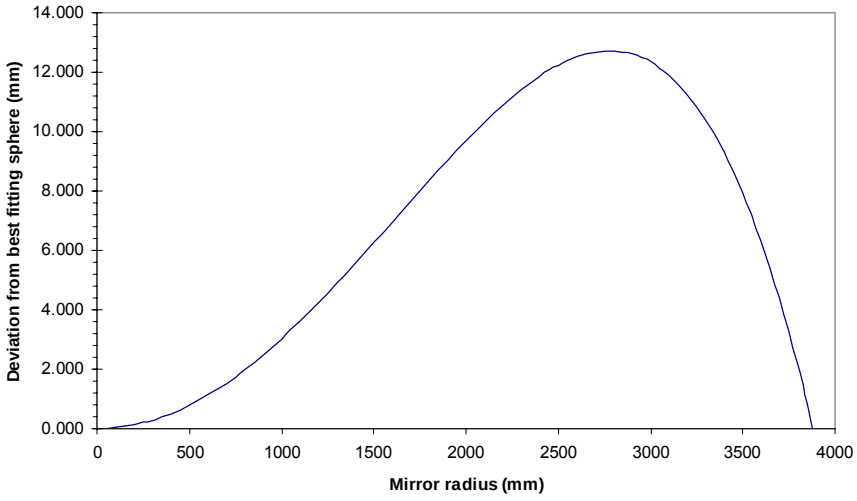

Figure 6-55. M4 aspherization profile.

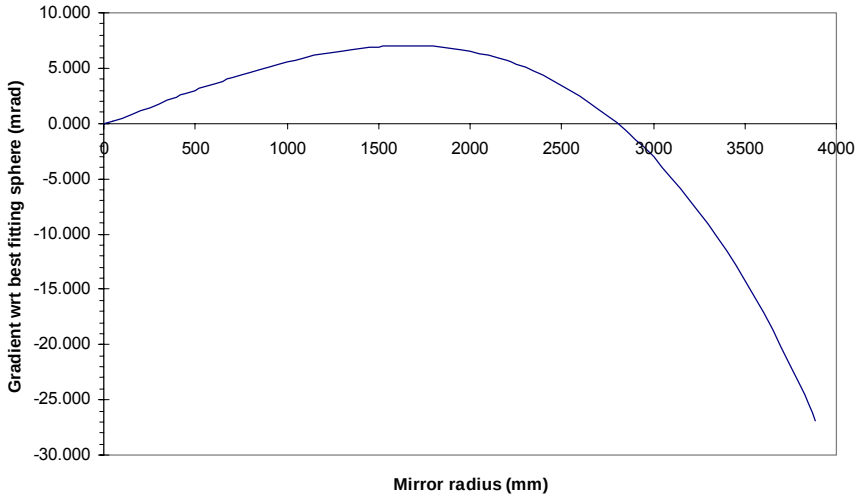

Figure 6-56. M4 slope difference with respect to best fitting sphere.

With radii of curvature 18.690-m and 19.970-m, respectively, M3 and M4 have a larger sag than the VLT primary mirrors. As a result, the last 8-m Zerodur blank still available at SCHOTT would be suitable for M4 with a final thickness of ~135 mm, to be compared to 175 mm for the VLT primary mirrors (the situation is much less favorable for M3). Although not impossible, such thinning would imply a significant densification of support systems for optical fabrication, transport, handling and operation. On the positive side, higher mirror flexibility and higher aerial density of the active support would allow for the correction of higher order modes than in the VLT. There is however no strong incentive to do so at this stage.

Attempts have been made to modify the optical design with a view to increasing at least one of the two 8-m class mirror radius of curvature to a VLT blank-compatible value, without success – unless the primary mirror focal ratio is relaxed[56]. According to SCHOTT, re-building the VLT 8-m production facility for 2 blanks would lead to fairly high costs. This situation would certainly change if the 8-m blanks were to be ordered together with the segment blanks as a global package.

For 8-m ULE blanks, CORNING provided more attractive if only indicative prices on the basis of Gemini specifications, with a radius of curvature changed to 19-m. Here again, there would be a substantial (20%) price reduction in the event of a joint order for the segments and 8-m blanks. According to CORNING, the first blank would be delivered ex works 24 months after placing the order, followed by the second one 16 months later. This schedule seems optimistic but could be secured by an advanced order of raw material.

M3 and M4 are storng aspheres, with 1.96-mm and 12.0 mm.departure from best fitting sphere, respectively. Figure 6-55and Figure 6-56 show the aspherization profile and slope variation with respect to best fitting sphere of M4. The latter is more representative of difficulty to produce a smooth surface, and about 40 times stronger than with a VLT primary mirror. In the following we concentrate on M4, which is by far the most difficult to polish and test.

Low spatial frequency terms are of no concern as the mirror will be actively supported. With the VLT, about 80 N active forces were required to correct for low spatial frequency misfigure. This is less than 10% of the full active range, about half of which is used for the conversion Nasmyth to Cassegrain. As no such conversion is required with OWL, the allowable low frequency terms or the actuator range could be relaxed in comparison to VLT. Figure 6-57 shows the high spatial frequency content of the VLT primary mirrors, in terms of wavefront RMS vs subpupil diameter. The smallest tool used in the very final stages of polishing of the fourth mirror was about 30 cm in diameter. With a slope deviation from best fitting sphere 40 times larger with OWL M4 than

[56] With a f/1.42 primary mirror, the sag of M4 is only 13 mm larger than that of a VLT primary mirror and the remaining SCHOTT blank would be usable, with a final mirror thickness of ~160 mm.

with VLT M1, one would expect a misfigure about 40 times worse, with the same tools and processes as for the VLT.

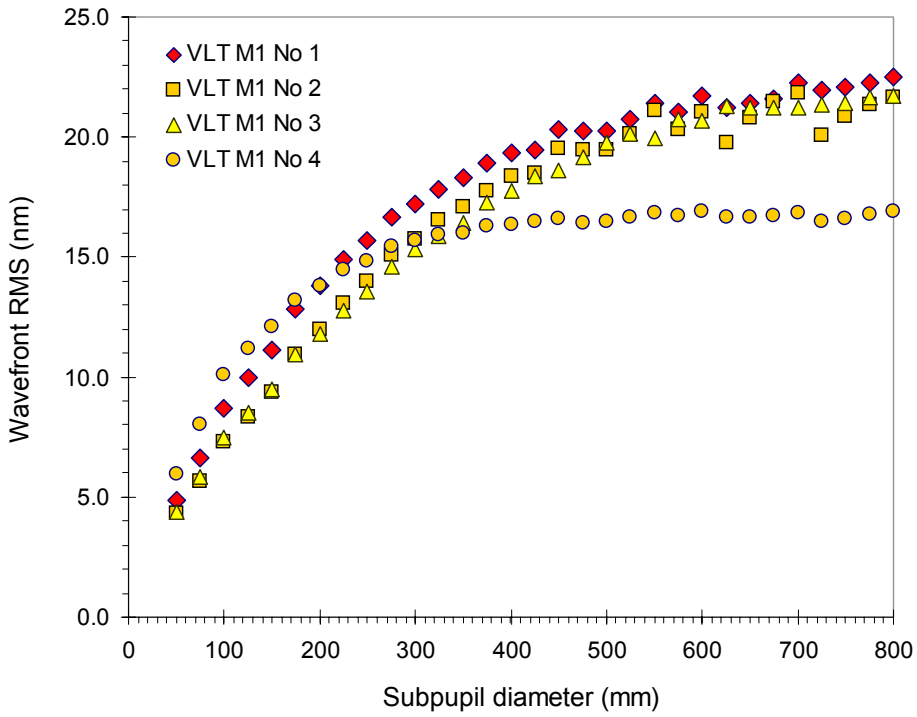

Figure 6-57. High spatial frequency wavefront error, VLT primary mirror.

With a magnification of 12.5 between M4 and the entrance pupil, the cut-off of the first generation adaptive optics would correspond to a period of ~80 mm on M4. From Figure 6-57 and applying the above scaling factor of 40 we infer that residual errors would be in the 200-300 nm wavefront RMS range. This is, hopefully, grossly pessimistic.

The optical quality specification for M4 is still to be finalized. The expected requirements are

- Wavefront RMS better than ~60 nm RMS after active and first generation adaptive correction (~80 mm spatial period on the mirror)
- Wavefront RMS better than ~10 nm RMS after active and high order (~10 mm spatial period) adaptive correction.

There has been very significant progress in optical fabrication since the polishing of the VLT primary mirrors. In addition, these mirrors were polished without making particular effort on minimizing spatial periods below ~0.5-m. Neverthelss, comprehensive studies by experienced optical manufacturers are still required. We expect OWL M4 to require very small tools (~1 cm) in the last stages of polishing, and a correspondingly long processing time.

While M3 could most probably be tested at centre of curvature through an Oeffner nulling system, M4 requires a considerably more complex test set-up. One option would be to test it against M3 and through a all-spherical 3-lenses compensator (Figure 6-58, simulated interferogram in Figure 6-59). This set-up has been conceived only to demonstrate that a theoretical solution not relying on aspheric optics or Computer-Generated Holograms exists – albeit a very inconvenient one in terms of practical implementation. The largest lens is 1.6-m in size and could be made of glassy Zerodur. M3 would have to be mounted upside down above M4. The set-up is extremely sensitive to decentres of the nulling system. This could, however, be alleviated by performing the optical tests at different azimuthal orientation of M4 (as was done with the VLT primary mirror) or by axially rotating the nulling system to disentangle non-axisymmetrical terms. Centring of the null-lens could be done to a few microns by inserting

symmetrical masks in the causticf of aberrations and re-centring the null-lens until obscurations are symmetrical[57].

One should also take into account the fact that M3 and M4 are active i.e. a considerable relaxation of low order terms is possible.

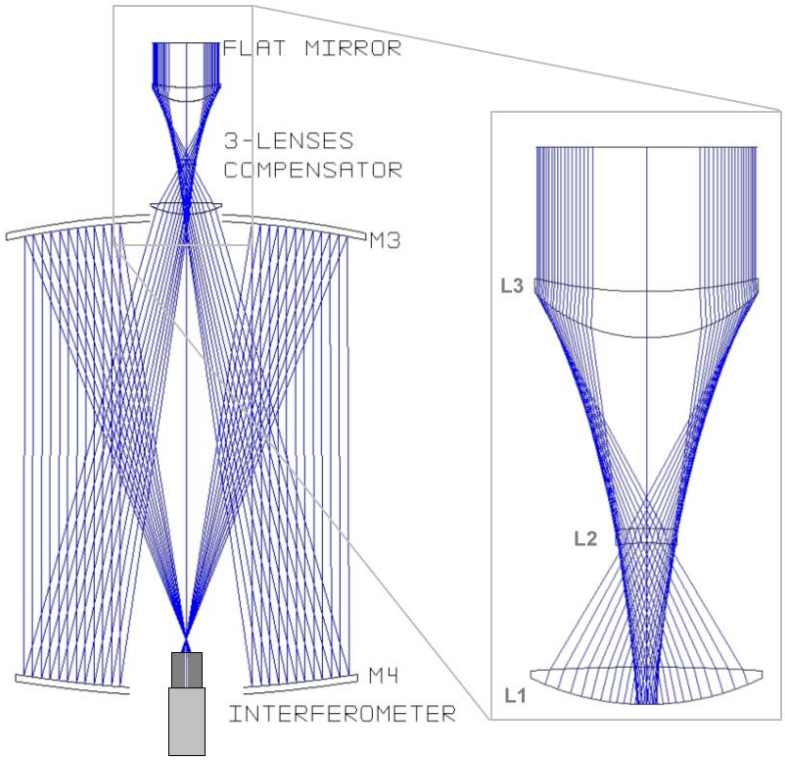

Figure 6-58. M4 optical test set-up.

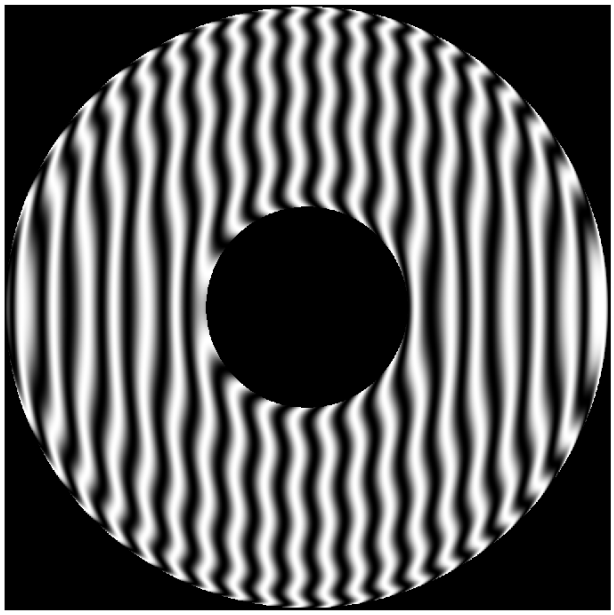

Figure 6-59. M4 nominal interferogram, double pass.

[57] This procedure was applied to the VLT primary mirror and proved not only accurate but also easy –the null-lens was centred to a few hundredth of a mm without particular effort.

6.6 Safety

The probability of failure P of a glass-ceramic part depends on the following parameters:

- Tensile stress σ
- Total area A of the part under stress
- Duration t of the load generating tensile stress
- Surface finish
- Material Weibull modulus □.

More specifically, the tensile stress σ_A over an area A and corresponding to a probability of breakage P is given by

$$\sigma_A = \sigma_0 \left(\frac{A_0}{A} \ln \frac{1}{1-P} \right)^{1/\lambda} \qquad \textit{Eq. 6-5,}$$

where σ_0 is the tensile stress over an area A_0 and corresponding to a $1\text{-}e^{-1}$ i.e. 63 % breakage probability. With Zerodur, D151 surface finish, σ_0=53.7 MPa and λ=14, while with acid-etched D64 it is σ_0=219.8 MPa and λ =6. In that case Eq. 6-5 assumes a 2 seconds load. If the duration t [in seconds] of the load is not 2 seconds, the tensile stress σ_{At} corresponding to the probability P is

$$\sigma_{At} = \sigma_A \left(\frac{t}{2} \right)^{-0.0417} \qquad \textit{Eq. 6-6.}$$

Conservatively assuming D151 on all surfaces, 11 MPa tensile stress over all surfaces of a segment would lead to a breakage probability of 10^{-5} over 2 seconds load time. The corresponding figures for 24 hours and 40 years loads are 6.9 and 4.6 MPa, respectively. These limits apply, however, to a single individual segment and are representative of desirable stress limits upon handling and transport only. Stress limits in operation shall assume that the complete mirror is under load. Assuming a total load area of 14,000 m², the allowable tensile stress limits for a 10^{-5} overall probability of failure are 6.2 MPa for a 2 seconds load, 4.0 MPa for a 24 hours load, and 2.7 Mpa for a 40 years (i.e. permanent) load.

For reference, interfaces and equipments for the VLT primary mirrors have been designed with a 3 MPa tensile stress limit for permanent load and 5 MPa for short-term (24 hours) loads. Only under extreme conditions (temperature ≤ -10 °C, leading to local stresses in bonded joints; earthquake; excessive vibrations and load transfers during transportation to site) could the limits be approached –but not exceeded Under normal operation, tensile stresses in the VLT 8-m mirrors are an order of magnitude below the specified limits.

With silicon carbide the situation is more favorable because of higher strength limits and lower masses. Stress concentration at the discontinuities of lightweight structures should hoever not be underestimated and a complete stress anaylis, taking into account actual segment geometry, will be required. The same comment applies with lightweight Zerodur.

With OWL and in normal operation, highest tensile stresses would in principle occur within the mirrors facing down i.e. the secondary, quaternary and M6 mirrors. Applying to above stress limits calculated for a complete 14,000 m² loaded area is, therefore, conservative. It is worth noting that the aerial density of OWL segments axial supports, with 18 supports and a segment size of 1.6-m, is comparable to that of the VLT primary mirrors, with 450 pads (3 pads per axial support tripod) and a mirror diameter of 8.2-m.

Whereby breakage of a single segment during transport or handling outside the telescope would not be catastrophic –assuming such breakage would not pose a threat to human safety-,

failure in the telescope could evidently lead to catastrophic damage –in particular with M2 segments-, not to mention inacceptable threat to human safety.

A suitable strategy for the preservation of human and system safety during transport, integration, operation and mainentnace still needs to be developed, taking the above into account. Possible measures to improve safety include:

- Acid etching of critical areas (interfaces);
- Safety support systems preventing large blocks to fall through in case of breakage;
- Protective canvas, reinforced mirror covers (M2) and corrector cage (M3 to M6);
- Suitable handling procedures, avoiding human presence under load; minimizing human intervention.

Transport, integration and maintenance aspects are also addressed in sections 13.1.1.2, 13.2.1.4, and 15.1.2.